Spring 2023

# Electrodeposition of Epitaxial Wide Bandgap P-Type Semiconductors and Copper Metal for Energy Conversion and Flexible Electronics

Bin Luo
*Missouri University of Science and Technology*



Department: Chemistry

# ELECTRODEPOSITION OF EPITAXIAL WIDE BANDGAP P-TYPE SEMICONDUCTORS AND COPPER METAL FOR ENERGY CONVERSION AND FLEXIBLE ELECTRONICS

by

BIN LUO

A DISSERTATION

Presented to the Graduate Faculty of the

MISSOURI UNIVERSITY OF SCIENCE AND TECHNOLOGY

In Partial Fulfillment of the Requirements for the Degree

DOCTOR OF PHILOSOPHY

in

CHEMISTRY

2023

Approved by:

Jay A. Switzer, Advisor
Manashi Nath
Amitava Choudhury
Jeffrey G. Winiarz
Michael S. Moats

## PUBLICATION DISSERTATION OPTION

This dissertation consists of the following three articles which are published in peer-reviewed journals:

Paper I: Epitaxial Electrodeposition of Hole Transport CuSCN Nanorods on Au (111) at the Wafer Scale and Lift-off to Produce Flexible and Transparent Foils, found on pages 31 - 65, is published in *Chemistry of Materials*, 2022, 34 (3), pp. 970-978.

Paper II: Epitaxial Electrodeposition of Wide Bandgap Cuprous Bromide on Silver via a Silver Bromide Buffer Layer, found on pages 66 - 89, is published in *Journal of The Electrochemical Society*, 2022, 169 (9), p. 092512.

Paper III: Epitaxial Electrodeposition of Cu (111) onto an L-Cysteine Self-Assembled Monolayer on Au (111) and Epitaxial Lift-Off of Single-Crystal-like Cu Foils for Flexible Electronics, found on pages 90 - 127, is published in *The Journal of Physical Chemistry C*, 2020, 124 (39), pp. 21426-21434.

## ABSTRACT

Epitaxial electrodeposition is a simple, low-cost technology to produce highly ordered materials on single-crystal surfaces. This research focuses on the epitaxial electrodeposition of wide bandgap p-type semiconductors and epitaxial Cu thin films via a self-assembled monolayer for energy conversion and flexible electronics. Paper I introduces the epitaxial electrodeposition of hole conducting CuSCN nanorods onto Au(111) surface, and lift-off to produce flexible and transparent foils. Highly ordered CuSCN could serve as an inorganic transport layer in various opto-electronic devices such as perovskite solar cells, LEDs, and transistors. An ordered and transparent CuSCN foil was also produced by epitaxial lift-off following a triiodide etch of the thin Au substrate. Paper II presents a scheme for epitaxial electrodeposition of wide bandgap CuBr on Ag via a AgBr buffer layer. CuBr shows potential for short-wavelength photo-detecting devices. Epitaxial CuBr(111) and Cu(100) are produced on Ag(111) and Ag(100) substrates, respectively. An oriented AgBr buffer layer, formed during the electrodeposition, is found crucial for directing the epitaxial growth of CuBr. Paper III describes a technique for epitaxial electrodeposition of a Cu(111) film on a self-assembled monolayer of the amino acid L-cysteine on Au(111). Direct epitaxial lift-off of the Cu film without etching gives a single-crystal-like Cu(111) foil with a low resistivity and good bending stability. It could be utilized as a low cost, flexible and ordered metal substrate for flexible electronics.

# ACKNOWLEDGMENTS

I would like to express my sincere thanks to my advisor, Dr. Jay A. Switzer, for offering me the opportunities to work on some interesting projects, and his continuous guidance and direction throughout my research. His knowledge and guidance inspired me to dig deeper into my research and generate new ideas. I could not have imagined having a better Ph.D. advisor. I would also like to thank my committee members, Dr. Manashi Nath, Dr. Amitava Choudhury, Dr. Michael S. Moats, and Dr. Jeffrey G. Winiarz, for their insightful suggestions and encouragement for my research. Their comments and feedback have helped me to improve my theoretical knowledge and experimental skills. In instrumentation, I would like to thank Dr. Eric Bohannan for his exceptional assistance on XRD, as well as the assistance in electron microscopy from Dr. Clarissa A. Wisner and Dr. Shatadru Chakravarty.

I express my appreciation to my friends and lab mates, including Xiaoting Zhang, John Z. Tubbesing, Dr. Avishek Banik, Taishi Higuchi-Roos, Dr. Qingzhi Chen, Christine Clauson, and Isaiah Robertson. They are supportive and helpful in my research. I would also like to thank my family for their constant love and support. I express my deepest appreciation to Jesus Christ, who is loving and leading me and my family. Finally, I would like to thank the funding support from the U.S. Department of Energy, Office of Basic Science under Grant No. DE-FG02-08ER46518.

# TABLE OF CONTENTS

Page

# LIST OF ILLUSTRATIONS

SECTION Page

PAPER II



PAPER III

# LIST OF TABLES

SECTION Page

# 1. INTRODUCTION

## 1.1. ELECTRODEPOSITION

Electrochemical deposition (electroplating) is a process of depositing materials onto a metal or semiconductor substrate by a redox reaction under an electric field. Electrodeposition was invented in 1805 by Italian inventor Luigi V. Brugnatelli by linking a wire between a battery and a gold solution.[1] Electrodeposition has been developed as a low-cost, convenient and fast method for thin film deposition and surface modification.[2-4] Other thin film technologies include molecular-beam epitaxy (MBE), chemical vapor deposition (CVD), chemical bath deposition (CBD), spin coating, physical vapor deposition (PVD) and atomic layer deposition (ALD).[5-10] Most of these methods require high temperature, high vacuum, expensive equipment, or complex experimental procedures. Electrodeposition has significant advantages including low cost, good controllability, and repeatability. It also offers the advantage of being able to control the departure from equilibrium through the applied potential. In addition, electrodeposition can achieve nano-sized thin layer deposits, which can make it a very cost-effective process. Electrodeposition has been further utilized in wider fields such as industrial metal electroplating, MEMS device fabrication, 3D printing technology, and semiconductor production.[11-14] The three-electrode system is the most commonly used electrochemical system due to its high stability and repeatability.

Thin film deposition is one of the most important applications of electrodeposition, which produces various functional layers such as metals, ceramics, magnets, MOFs, topological insulators, and thermoelectric films.[15-20] Among them, the electrochemical deposition of metals is a major application in industry such as semiconductor device fabrication, corrosion protection and FePt alloys for heat-assisted magnetic recording technology.[21-23] The principle of metal deposition is that high-valent metal cations are reduced to zero-valent metal elements and then deposited on the electrode surface, as shown in equation 1:

$$M^{n+} + ne^- \rightarrow M \quad (1)$$

For semiconductor deposition, the mechanism is more complicated. For elemental semiconductors such as Ge and Si, high-valent dissolved Ge(IV) species are reduced to Ge(0) and deposited, which is similar to equation 1.[24] However, the mechanism for semiconductors such as metal oxides and metal halides has two parts: firstly, an intermediate is generated by electrochemical redox reaction, and then a non-redox reaction occurs to generate the final product, which is deposited on the electrode surface. The electrochemical deposition process can effectively tune the properties of deposited film, such as thickness, morphology, crystal orientation and chirality by adjusting deposition conditions such as deposition time, solution composition, pH, temperature, and potential/current.[25-29]

## 1.2. EPITAXIAL ELECTRODEPOSITION OF THIN FILMS

A single crystal refers to a material in which the crystal lattice is continuous with long-range order and no grain boundaries. Single crystals have special optical, mechanical, magnetic and electrical properties in applications such as optical and electronic devices.[30-32] Epitaxial growth is a technology for controlled production of single-crystal-like materials.

**1.2.1 Epitaxy and Characterization.** We define epitaxy as an ordered material grown on a single crystal substrate that could directly control the in-plane and out-of-plane orientation of deposited material. Figure 1.1 shows the schematic diagram of a (A) polycrystalline film, (B) textured film, and (C) epitaxial film. A polycrystalline film has random out-of-plane and in-plane orientation. A textured film has a fixed out-of-plane orientation but has a random in-plane orientation. An epitaxial film has fixed both out-of-plane and in-plane orientations.

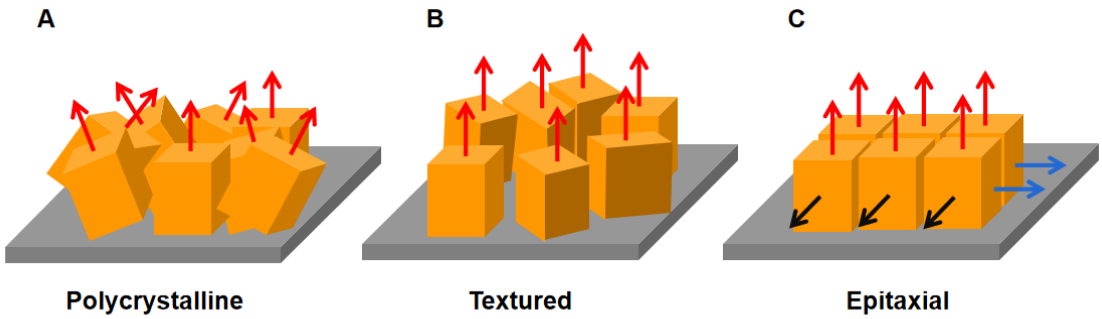


Figure 1.1. Schematic diagram of a (A) polycrystalline film, (B) textured film, and (C) epitaxial film.

According to the material composition difference between the grown film and the substrate, epitaxy techniques could be divided into homoepitaxy and heteroepitaxy. Homoepitaxy refers to the same material growing on the substrate that continues to grow the same crystal structure while heteroepitaxy refers to a different material growing on the substrate. In the case of heteroepitaxy, thermodynamic and kinetic mechanisms are involved in the growth of the epitaxial film. To achieve epitaxy, the mismatch between deposited material and substrate is crucial because less mismatch of the crystal lattice causes less defects and strains of the deposited layer. As shown in equation 2, lattice mismatch is defined as the difference between the lattice parameter of the film ($\alpha_F$) and the lattice parameter of the substrate ($\alpha_S$):

$$\text{mismatch} = (\alpha_F - \alpha_S) / \alpha_S \times 100\% \quad (2)$$

For simple epitaxial growth of the same material or material with a similar crystal structure, this equation could explain the epitaxial growth. For instance, cubic CuCl has $\alpha_F$ = 0.542 nm and cubic Si has $\alpha_S$ = 0.543 nm, so the CuCl(111)//Si(111) system has a mismatch of -0.18%. However, what we see experimentally tells us that even some large mismatched systems and some materials with different crystal structures can grow epitaxially. To explain that, an expanded lattice mismatch model known as coincidence site lattices (CSLs) is invoked. The interface model of CuSCN(003) on Au(111) (Figure 1.2) shows the formation of the CSL, in which 4 S atoms align with 5 Au atoms, and a mismatch of +0.22% is produced. The plausible CSL reduces in-plane stress on the

interface of CuSCN/Au. Epitaxial semiconductors have improved electronic properties because the structural order is increased due to the minimization of the density of defects and grain boundaries, which reduces electron-hole recombination probabilities.

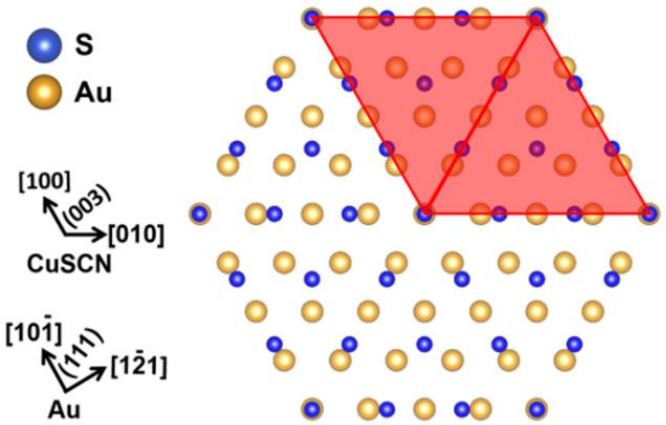


Figure 1.2. The atomic interfacial model of CuSCN(003) on Au(111).

Compared to polycrystalline and amorphous materials, epitaxial materials have significant advantages in various electronic devices. In silicon photovoltaic cells, single crystal silicon has the highest photoelectric conversion efficiency (26.1%), which is higher than polycrystalline silicon (22.3%) and amorphous silicon (14.0%).[33] In perovskite solar cells, single crystalline perovskite materials also have higher photoconversion efficiencies due to lower trap densities and a larger diffusion length.[34] In transparent p-n junctions, epitaxial heterojunctions show significantly higher rectification ratios.[35]

Epitaxial growth technologies include liquid-phase epitaxy (LPE), vapor-phase epitaxy (VPE) and soft-solution epitaxy. LPE is a high temperature liquid melt method

which is widely used in the semiconductor industry such as the $Al_xGa_{1-x}As$ material system.[36] VPE involves MBE, CVD, PVD and other techniques, which use vapor precursors to deposit various high-quality epitaxial materials such as the LED material GaN and topological insulator $Bi_2Te_3$.[37-39] However, these methods have high cost and high energy consumption because of the need for high temperature and high vacuum conditions as well as expensive instruments. Due to low cost and fast deposition, soft-solution epitaxy has been developed in recent years. Soft-solution epitaxy refers to epitaxial growth in an aqueous solution or organic solvent, such as electrodeposition, chemical bath deposition (CBD) and spin coating.[40-42] Among them, epitaxial electrodeposition offers a highly scalable deposition process which gives a high level of control over film thickness, orientation, and morphology. Epitaxial electrodeposition of various materials including metal oxides, metals, perovskites, and metal sulfides have been achieved on single crystal metals for decades.[43-47] In order to break through the limitation of expensive substrates and small size, epitaxial metals such as Au, Cu, Ag on a silicon substrate have been explored in the last 5 years, because single-crystal silicon is the bedrock of semiconductor devices.[48-50] Since the silicon surface is easy to oxidize to form an amorphous $SiO_x$ layer, pre-polarization of silicon at negative potentials is crucial for epitaxial growth. In the case of Au deposition on Si substrate, Si was firstly washed with 5% hydrofluoric acid (HF) to remove the native oxide layer to form a H-terminated Si surface and was then pre-polarized at -1.9 V vs. Ag/AgCl and dipped into the Au deposition bath. The ultra-thin Au film on

Si could serve as a low cost and large area substrate for further epitaxial growth of other functional materials and even lift-off for flexible electronics.[50] Based on wafer-sized Au/Si substrates, epitaxial $Cu_2O$, ZnO, and $BiI_3$ have been electrodeposited which have potential for mass production in the semiconductor industry. [50-52]

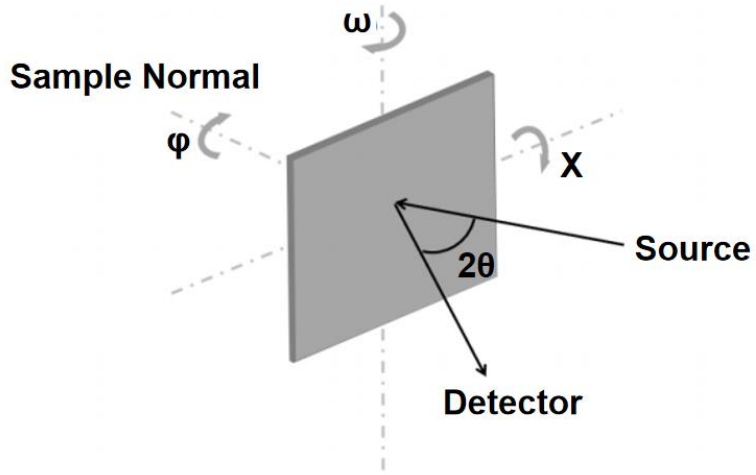


Figure 1.3. Thin film X-ray diffraction measurement with axes of rotation.

To determine the epitaxy of a material, several techniques are utilized for characterization. X-ray diffraction is one of the most commonly used methods to measure crystallographic order on a global scale.[53] Figure 1.3 shows thin film X-ray diffraction measurement with three axes of rotation. For thin film measurement, simple 2θ scans could give diffraction peaks and intensities showing the structure of materials according to Bragg's law. Meanwhile, the out-of-plane orientation could be determined by analysis of diffraction peak positions and intensities in 2θ scans. For instance, the XRD pattern of CuSCN/Au(111)/Si(111) only shows the {00l} reflections for the CuSCN, indicating [001]

out-of-plane order. However, the 2θ scan alone is not enough to determine whether the material has in-plane order. Epitaxial and textured materials both exhibit out-of-plane order in 2θ scans. X-ray pole figures are a powerful technique to analyze the in-plane order of a crystal. A pole figure is a stereographic projection where an angle χ is tilted from 0° to 90° and azimuthal angle φ is rotated from 0° to 360° while a specific Bragg angle 2θ is fixed. Diffraction signals collected from φ at each tilt angle χ (normally using a 3° step size), are used to build a 2D pole figure plot. In the case of epitaxial materials, the pole figure should manifest itself as separated spots at a specific tilt angle χ which is equal to the angle between the chosen plane and the oriented plane of the sample. The number of spots corresponds to the symmetry of the plane of the crystal. If the material is textured, there would be a ring rather than spots at the same tilt angle showing no in-plane order. For instance, as shown in Figure 1.4A, the (104) pole figure of epitaxial CuSCN(003) shows six intense spots (tilt angle: 50.93°) which are separated azimuthally by 60°. This tilt angle indicates that the angle between the (003) and (104) planes is 50.93°. Figure 1.4B shows that textured CuSCN(003) on a sputtered Au(111)/glass without in-plane order shows a ring pattern confirming the lack of in-plane order of CuSCN. The epitaxial perfection and relationship could be further measured by azimuthal scans at certain tilts and Bragg angles. The mosaic spread during epitaxial growth could be measured by rocking curves analysis.

Scanning electron microscopy (SEM) and transmission electron microscopy (TEM) are useful techniques to visualize the epitaxy of deposited materials. In SEM images, some

epitaxial morphological features could be directly observed, such as ordered crystals alignment in some directions. Although SEM images cannot determine the crystallographic orientation, they do show global in-plane orientation and indicate the nucleation and growth mechanism. High resolution transmission electron microscopy (HRTEM) can see atomic arrangement by lattice fringes and determine the orientation of deposited materials by d-spacing measurement. Electron diffraction (SAED) patterns could also be helpful to determine the epitaxial relationship. However, TEM analysis focuses on a small local region of a sample, which is not necessarily representative of the entire sample. The combination of X-ray techniques and electron microscopy is therefore an effective way to determine the epitaxy of thin films.

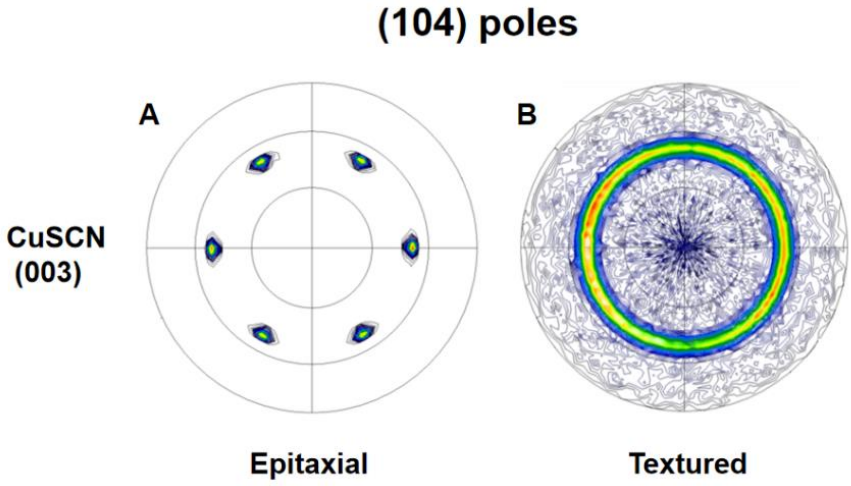


Figure 1.4. (104) poles of (A) epitaxial CuSCN(003) with in-plane order and (B) textured CuSCN(003) without in-plane order.

### 1.2.2. Epitaxial Electrodeposition of Wide Bandgap P-type Semiconductors.

Semiconductors are a class of materials with conductivity between metals and insulators which are essential to modern society. Without semiconductors, there would be no transistors, solar cells, LEDs, integrated circuits, and other devices which are the bedrock of information, lighting and energy technologies. Wide bandgap semiconductors normally refer to some semiconductors having bandgaps $\geqslant$ 3 eV, enabling transparency in the visible range.[54] Wide bandgap semiconductors are a large family including carbides (SiC), nitrides (GaN, AlN), oxides ($In_2O_3$, ZnO, $SnO_2$, $Ga_2O_3$, NiO) and halides (CuSCN, CuI, CuBr, CuCl). Due to their optical transparency, tunable carrier concentration and electrical conductivity, wide bandgap semiconductors are crucial for various advanced energy-conversion electronic devices such as displays,[55] thin film transistors,[56] solar cells,[57] LEDs,[58] high power electronics[59] and flexible electronics.[60] In the past decades, n-type wide bandgap semiconductors have been well studied, such as n-GaN,[61] n-ZnO,[62] Sn-doped $In_2O_3$ (ITO),[63] and indium gallium zinc oxide (IGZO).[64] They are extensively applied in transparent electrodes,[65] light-emitting devices[66] and UV detectors.[67] Just like every coin has two sides, wide bandgap p-type semiconductors are indispensable in various opto-electronic devices especially like transparent p-n junctions,[68] Si-based devices,[69] perovskite solar cells[70] and blue LEDs.[71] Low-cost and high quality wide bandgap p-type semiconductors are pressingly needed to enhance the entire performance of electronic devices.

**1.2.2.1. Hole transporting materials.** Wide bandgap p-type semiconductors have attracted significant attention in three main areas including hole transporting materials (HTMs), transparent conductive materials (TCMs) and short wavelength photo-devices. In recent years, there has been a significant trend in the development of light energy harvesting[72,73] and photoelectric conversion devices.[74,75] In the structure of various opto-electronics, HTMs play an essential role to significantly improve the efficiency of devices such as perovskite solar cells,[76,77] organic solar cells[78] and light emitting diodes.[79] HTM refers to p-type semiconductor layers using holes as majority charge carriers and blocking electron transport. HTMs could effectively extract photo-generated holes from photo-sensitive layers such as perovskite layers and form directional current through the device.

Perovskite solar cells (PSCs) are one of the most important devices which greatly depend on HTMs. PSCs are regarded as one of the most promising third-generation photovoltaic devices.[80,81] Perovskite, named after the mineralogist Lev Perovski, refers to the mineral calcium titanate ($CaTiO_3$).[82] Generally, the perovskite structure has an $ABX_3$ crystal structure. Perovskite-structured layers in solar cells are mainly organic-inorganic hybrid materials, such as $MaPbI_3$ and $FaPbI_3$[83,84] PSCs have high conversion efficiency (> 25%), which is at a comparable level with the single-crystal silicon solar cell.[85] Also, PSCs have low cost and convenient manufacturing by various methods such as spin coating, CVD and electrodeposition. For both n-i-p and p-i-n structures, general PSCs include an electron transport material (ETM) layer and a HTM layer on both sides of the perovskite

layer.[86] As shown in Figure 1.5, when sunlight hits the perovskite layer, it excites electrons from valence band (VB) to conduction band (CB). HTM extracts generated holes from VB of perovskite and leads to the metal layer while ETM extracts electrons from CB of perovskite and leads to the FTO.[87] In this way, the generation of directional current can be achieved.

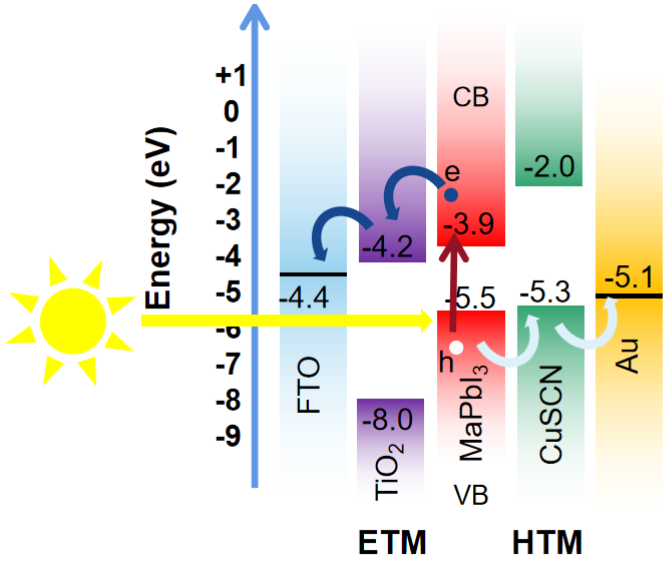


Figure 1.5. Energy diagram of a typical n-i-p perovskite solar cell.

The use of HTMs is crucial to getting highly efficient and long-term stable PSCs.[88,89] An ideal HTM should satisfy the following requirements: (1) high chemical stability to humidity and high thermal stability to high temperature; (2) low cost and easy fabrication which is suitable for mass production; (3) non-toxic nature; (4) suitable energy band positions to extract holes from VB of perovskite; (5) good hole transporting ability

including high hole mobility which could improve the efficiency of total device and avoid the charge recombination on the interface; (6) wide bandgap and high transparency in the visible range which is particularly important for the p-i-n structure. The conventional HTMs utilize organic structures including small organic molecules like Spiro-OMeTAD and polymers like polytriarylamine (PTAA) and PEDOT:PSS.[90,91] However, these organic HTMs show some limitations: (1) relatively high cost for scaling-up production; (2) poor stability which may cause degradation in high temperature; (3) limited hole transporting property with low hole mobility.

Therefore, there is increasing interest in using low cost and highly stable inorganic HTMs for PSCs.[92] A variety of wide bandgap semiconductors are developed for HTMs, including Cu(I) based semiconductors, molybdenum oxide ($MoO_x$), cobalt oxide ($CoO_x$), nickel oxide ($NiO_x$).[93-96] Cu(I) based semiconductors including cuprous thiocyanate (CuSCN), cuprous halides, $CuAlO_2$ are regarded as ideal HTMs for long-term efficient PSCs because they are low-cost wide bandgap p-type semiconductors with good hole-transporting properties.[97-100] CuSCN is one of the most promising inorganic HTMs.[101,102] CuSCN is a p-type metal pseudohalide semiconductor with an exceptionally large bandgap (3.7 ~ 3.9 eV), so the material is highly transparent (> 90% transmittance) in the visible range. CuSCN is earth abundant and inexpensive, which is available for mass production. CuSCN is highly stable in high temperature and humidity which ensure longtime good performance of PSCs.

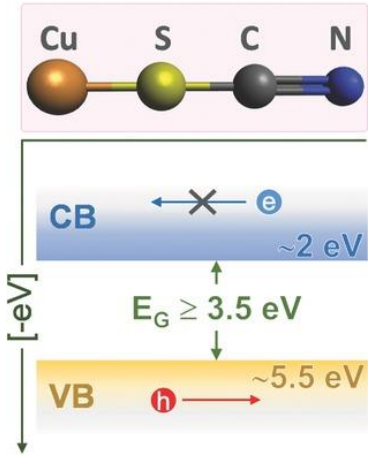


Figure 1.6. The band structure of CuSCN (image source [103]).

Figure 1.6 shows the band structure of CuSCN (image source [103]).[103] CuSCN's conduction band minimum (CBM) is around -2 eV which is not compatible with normal perovskite layers' CBM positions such as $MaPbI_3$. Therefore, electrons are highly forbidden from perovskite layers to CuSCN. The valence band maximum (VBM) is -5.2 eV ~ -5.5 eV which is suitable with perovskite's VBM and the work function of Au or carbon to efficiently transport holes. Therefore, CuSCN has good hole transporting and electron blocking properties. Due to excellent comprehensive performance, Neha Arora et al. applied CuSCN in stabilized perovskite solar cells with high-efficiency over 20%.[102] As a versatile inorganic HTM, CuSCN also gets attention in other electronic devices such as solar water splitting devices, field effect transistors and light-emitting diodes.[104-106] Owing to applying CuSCN as the hole transport layer, a standalone solar water splitting tandem cell achieved a solar-to-hydrogen efficiency of 4.55%.[104] Cuprous halides (CuX, X= Cl, Br, I) are another efficient inorganic HTM.[107,108] Cuprous halides are a class of nontoxic, earth

abundant and wide bandgap (2.9 ~ 3.4 eV) I-VII p-type semiconductors. CuCl, CuBr, CuI have bandgaps $E_{g(CuCl)}$ = 3.4 eV, $E_{g(CuBr)}$ = 3.0 eV, $E_g$(CuI) = 3.1 eV, respectively. Among them, CuI has been a promising candidate as HTM in PSCs and LED devices due to high transparency and high hole mobility.[109-112] For instance, spin-coated CuI thin films are favorable as an efficient inorganic hole transport layer for inverted planar perovskite solar cells because of long-term stability and anti-leaking performance.[113] CuBr has been also applied as an inorganic HTM in organic photovoltaics and transistors.[114,115]

Some P-type wide bandgap oxide semiconductor could be applied as hole transport layers.[116-122] $NiO_x$ is considered as a potential oxide hole transport layer in perovskite solar cells,[116,117] polymer solar cells[118] and quantum-dot light-emitting devices.[119] An ITO/Ag:$NiO_x$/$CH_3NH_3PbI_3$/PCBM/BCP/Ag structure achieved a stabilized solar-cell efficiency of 17.1%.[120] Solution-processed $WO_3$ exhibits hole selective behaviors in organic photovoltaics.[121] $WO_3$/spiro-OMeTAD double-layered hole transport layer helps to achieve high efficient (21.44%) planar perovskite solar cells.[122]

**1.2.2.2. Transparent conductive materials.** Transparent conductive materials are essential to serve as transparent electrodes or contacts for various devices, such as liquid crystal displays,[123] touch screens,[124] solar cells,[125] light emitting diodes[126] and water splitting photoelectrochemical devices,[127] which need light transmission to work. Some of the commonly used transparent conductive materials include wide bandgap semiconductors,[128,129] conductive polymers,[130,131] nanowire mesh substrates,[132,133]

graphene,[134] carbon nanotube[135] and ultrathin metal foils.[136] Among them, wide bandgap semiconductors especially metal oxides are one of the most extensively investigated areas due to their high transparency and conductivity. One of the most well-known transparent conducting oxides is Sn-doped $In_2O_3$ (ITO), which has been applied in a variety of commercial devices.[137] ITO exhibits an electrical conductivity of $10^4$ S.cm and over 80% transparency in the visible range.[137] Other alternatives include F-doped $SnO_2$,[138] Al-doped ZnO,[139] and indium gallium zinc oxide.[140] Amorphous indium gallium zinc oxide has been heavily investigated in oxide thin film transistor (TFT) for commercial displays.[141]

In the past decades, most of transparent conductive oxides are n-type semiconductors because of the nature of electronic structure. High performance p-type transparent conductive materials remain a challenge.[142] They suffer from poor optical transparency and low electrical conductivity, which are not yet sufficient for the development of new devices such as transparent transistors. Recently, there is a trend to develop novel p-type wide bandgap semiconductors as transparent conductive materials such as NiO,[143] $Cu_2O$,[144] $CuAlO_2$,[145] CuI,[146] CuBr.[147] In metal oxides, NiO is a candidate for p-type transparent conducting oxide material because of its bandgap in the range of 3.6 ~ 4.0 eV.[148] By doping with other atoms, the conductivity of NiO could be increased. V-doped NiO,[149] Li-doped NiO[150] and Cu-doped NiO[151] have been developed as p-type transparent conductive films. In non-oxide semiconductors, Cu based wide bandgap semiconductors are regarded as promising materials for transparent conductive films.[152]

Copper halides, especially CuI attract great interest because of their wide bandgap (3.1 eV) and over 80% transparency in the visible range.[153] More importantly, CuI has high hole mobility of 43.9 $cm^2V^{-1}S^{-1}$ in single crystalline γ-CuI and high carrier density ($10^{20}$ $cm^{-3}$) which is suitable for high performance transparent conductive materials.[153] By doping with iodide, a degenerate p-type CuI thin film was prepared with a conductivity of 283 $S.cm^{-1}$.[154] A sulfur-doped CuI with further treatment with $H_2O_2$ also achieved a high electrical conductivity of 596 $S.cm^{-1}$.[155] Also, CuI is easy to be prepared by various soft-solution processes which are suitable for scaling-up production.[156-158] Our group developed an epitaxial electrodeposition and lift-off method to prepare CuI foils as a flexible transparent conductive substrate for flexible electronic devices.[159]

**1.2.2.3. Short wavelength photo-devices.** Wide bandgap semiconductors have been extensively applied in photo-related devices.[160,161] According to the directions of energy conversion between electrical energy and light, there are two main applications: blue LEDs and UV photodetectors. Blue LEDs refers to a class of opto-electronic devices that could directly convert electrical energy to blue light. Wide bandgap semiconductors with large exciton binding energies enable high-energy photons to be released at forward applied bias when the recombination of electrons and holes occurs. The wide bandgap semiconductors for blue LEDs include III-V materials such as GaN,[162] AlGaN,[163] II-VI materials such as ZnO,[164] group IV materials such as SiC,[165] and group I-VII materials such as CuCl,[166] CuBr.[167] The leading materials group is III-nitrides GaN ($E_g$ = 3.4 eV, exciton

binding energy 23 meV) and its alloys which have been commercialized in a variety of lighting devices.[168,169] In 2014, because of the development of efficient blue GaN LEDs, three Japanese scientists, Isamu Akasaki, Hiroshi Amano and Shuji Nakamura were awarded the Nobel Prize in Physics.[170] However, the high cost of materials and expensive instruments for the fabrication of GaN devices are still issues.[166] ZnO could be a low cost alternative blue LED material due to its wide bandgap (3.44 eV) and large exciton binding energy (63 meV). n-ZnO/p-CuI,[171] n-ZnO/p-GaN,[172] n-ZnO/p-CuSCN[173] heterojunctions have been reported as short wavelength light emitting devices. There is a developing interest in silicon-based blue LED devices because silicon is the most dominant material in the semiconductor industry with a low price and mature processes.[174] Copper halides could be potential intrinsic p-type materials for UV/Blue light emission,[175,176] due to their large bandgaps and exceptional large exciton binding energies (CuCl 190 meV, CuBr 108 meV and CuI 62 meV). In particular, CuCl has close lattice match with Si (mismatch -0.18%), so CuCl/Si could minimize dislocation and in-plane tension for producing low-mismatch Si-based blue LED devices.[218,219]

UV photodetectors are a class of opto-electronic devices that detect UV light via electrical signals. UV photodetectors show wide potential applications such as solar UV detection,[177] flame detection[178] and environmental monitoring.[179] Earth abundant wide bandgap semiconductors including ZnO,[180] $TiO_2$,[181] NiO,[182] CuSCN[183] and copper halides[184] have gained extensive attention for low cost and high-performance UV

photodetectors. Self-powered ZnO/SrCoOx,[180] ZnO/CuSCN[185] and ZnO/CuI[186] p-n junctions exhibit rapid response and high on/off ratios. A self-powered Fe-doped $TiO_2$/n-Si heterojunction UV-visible photodetector was fabricated via a general solution process.[181] NiO nanoflakes with $TiO_2$ nanorods arrays contributed to enhanced UV photoresponse.[182] P-CuSCN/n-$Ga_2O_3$ thin film heterojunctions achieved highly sensitive deep UV photodetection.[183] A Ag/CuSCN/Ag metal-semiconductor-metal (MSM) structure produced high performance deep UV photodetector.[187] Ultrathin 2D nonlayered CuBr flakes have been used to build UV photodetectors with high photoresponsivity of 3.17 A $W^{-1}$ and fast response (a fast rise time of 32 ms and a decay time of 48 ms).[188] Transparent CuI/a-IGZO heterojunctions also serve as UV photodetectors with excellent linearity.[189]

**1.2.2.4. Benefits of epitaxial wide bandgap p-type semiconductors**. Epitaxial wide bandgap p-type semiconductors have some significant advantages. Firstly, due to the good control of in-plane and out-of-plane orientation, epitaxial wide bandgap semiconductors with reduced electron-hole recombination probabilities could improve charge transport when compared with polycrystalline counterparts.[190] This is especially important for HTM materials. An ordered HTM with fewer defects could have facilitated hole transport to help improve the overall performance of solar cell devices.[191-194,220] For example, mesoscale ordering of a single crystal spiro-OMeTAD exhibits increased mobility by three orders of magnitude.[220] In paper I, epitaxial CuSCN produces an inorganic Schottky diode Au/CuSCN/Ag with more ideal rectifying behavior. Epitaxial

CuSCN has a diode quality factor of 1.4, whereas polycrystalline CuSCN has a diode quality factor of 2.1. Secondly, epitaxial wide bandgap semiconductors provide a pathway to serve as single-crystal-like substrates for all-epitaxial optoelectronic devices.[195] Epitaxial HTMs allow the further growth of perovskite layers for all-epitaxial perovskite solar cells. Epitaxial transparent conductive materials allow the fabrication of high-performance transparent wide bandgap p-n junctions.[196,197,35] For example, the epitaxial CuI/ZnO heterojunction exhibits high rectification ratios larger than $10^9$.[35] In addition, epitaxy can be utilized to adjust the composition of semiconductors such as the doping concentration and the production of alloys.[198] Also, epitaxy could be used for producing superlattices and metastable phases with novel properties.[199,200]

**1.2.2.5. Epitaxial electrodeposition of Cu(I) based wide bandgap p-type semiconductors.** As mentioned above, some Cu(I) based semiconductors such as CuSCN, CuI, CuBr, CuCl are important wide bandgap p-type semiconductors. They show p-type conductivity due to Cu vacancies.[201] Table 1.1. shows some characteristics of various Cu(I) based wide bandgap p-type semiconductors. CuSCN has α phase and β phase at room temperature, but β-CuSCN is normally observed as HTMs. β-CuSCN has a rhombohedral structure with lattice parameters a = b = 0.3857 nm, c = 1.6449 nm and R3m (160) space group. SCN groups connect with the planes of Cu atoms by Cu-N bonds and Cu-S bonds to build the entire β-CuSCN structure. There are rarely reports of vapor-phase deposition of CuSCN films.[202] The reason could be attributed to the instability of the SCN group under

high temperature (> 200℃) and high vacuum, which causes spontaneous decomposition. There are numerous reports about CuSCN films produced by soft-solution processes such as spin coating,[203] chemical bath deposition,[204] electrodeposition[205] and SILAR methods.[206] Electrodeposition is particularly interesting because CuSCN nanorod arrays with large surface area could be deposited by mass-transfer limitation control during the deposition process.[207] However, the deposited CuSCN yields an amorphous film, polycrystalline film or a fiber texture with no in-plane order, limiting its hole transport property.[208] Therefore, the hole mobility (0.01 ~ 0.1 $cm^2V^{-1}S^{-1}$) of solution-processed CuSCN is still quite limited compared with other inorganic HTMs.[209]

Cuprous halides normally exhibit a γ-polymorph with a zinc blende structure (space group, $F\bar{4}3m$) at room temperature. Cu atoms tetrahedrally coordinate with halogen atoms to form the cuprous halide structure. CuCl, CuBr, CuI have lattice parameters $a_{(CuCl)} = 0.542$ nm, $a_{(CuBr)} = 0.568$ nm, $a_{(CuI)} = 0.605$ nm, respectively. The heteroepitaxial growth of cuprous halides has been well studied by vapor-phase techniques such as DC sputtering,[35] molecular beam epitaxy[210,211] and pulsed laser deposition.[212] Other common methods such as spin-coating,[156] chemical bath deposition[213] and chemical vapor deposition[214] mostly produce amorphous or polycrystalline films. Cuprous halides thin films also have been electrodeposited, but only with polycrystalline structures or fiber textures with no in-plane orientation.[215,216] Epitaxial cuprous halides produced by electrodeposition still face some challenges such as substrates, bath compositions and deposition conditions.

Table 1.1. Some characteristics for various Cu(I) based wide bandgap p-type semiconductors.

| Cu(I) based semiconductors | Crystal structure | Lattice parameters (nm) | Bandgap (eV) | Type | Main applications |
|---|---|---|---|---|---|
| CuSCN | Rhombohedral | a=0.3856, c=3.2905 | > 3.5 eV (3.7-3.9 eV) | P | HTMs, LEDs, UV sensors |
| CuI | Cubic | 0.60521 | 3.1 eV | P | HTMs, TCMs, LEDs |
| CuBr | Cubic | 0.56897 | 3.0 eV | P | HTMs, UV sensors |
| CuCl | Cubic | 0.54202 | 3.4 eV | P | Si-based blue LEDs |

Our strategies for electrochemical deposition of epitaxial Cu(I) based wide bandgap p-type semiconductors are shown in Figure 1.7. The mechanism has two parts: firstly, Cu(II) is reduced to $Cu^+$ on the electrode surface by an electrochemical redox reaction, and then $Cu^+$ combines with surrounding anions to generate insoluble Cu(I) based semiconductors which could nucleate and epitaxially grow on the ordered substrate. The substrate could directly control the in-plane and out-of-plane orientations of the deposited semiconductors.

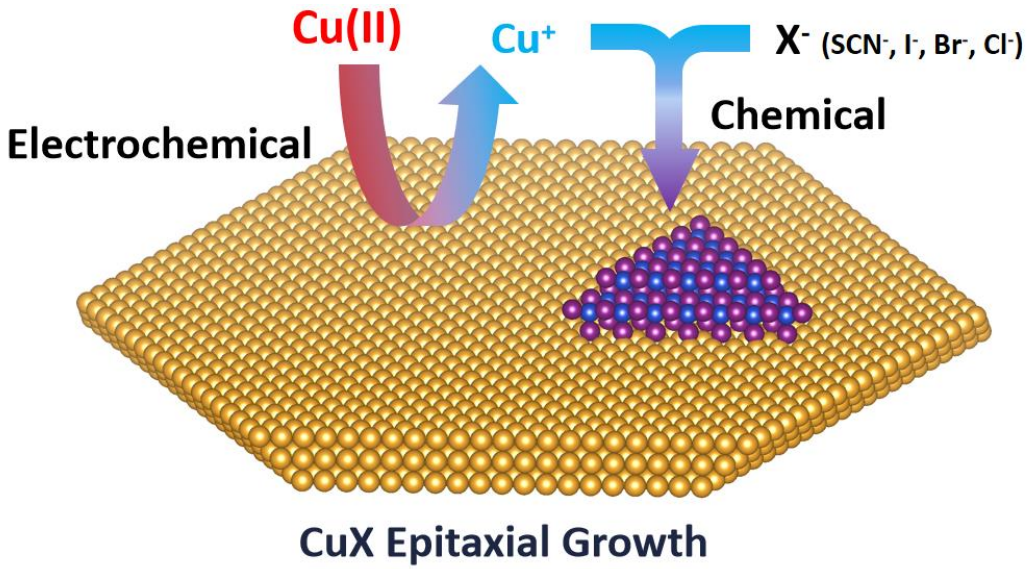


Figure 1.7. The mechanism of electrochemical deposition of epitaxial Cu(I) based wide bandgap p-type semiconductors.

General electrochemical reactions can be written in equations 3 and 4, where $X^-$ represents different anions, including $SCN^-$, $I^-$, $Br^-$, $Cl^-$.

$$Cu(II) + e^- = Cu^+, E^0 = +0.159 \text{ V vs. NHE} \quad (3)$$

$$Cu^+ + X^- = CuX \quad (4)$$

Our electrochemical deposition of Cu(I) based wide bandgap p-type semiconductors was performed on some ordered substrates from a solution containing 20 mM $CuSO_4$ as a Cu source and 40 mM KX as the source of anions and the supporting electrolytes, with the pH of 3~5. The electrodeposition could be performed at room temperature and 1 atm pressure. It should be noted that in the electrochemical bath, some $Cu(II)X_2$ such as $Cu(II)I_2$ and $Cu(SCN)_2$ have low solubility in aqueous solution which could lead to precipitation and decomposition during the deposition process. To prevent

that, in the CuSCN and CuI cases, we use EDTA to complex and protect Cu(II) to form a clear solution.[217] Normally, an applied potential between -0.1 V ~ -0.4 V vs. Ag/AgCl is suitable to produce pure Cu(I)X phases, while more negative applied potentials could produce Cu metal from the reduction of Cu(I)X or from direct deposition from solution.

In paper I, we introduced a simple electrochemical route for the epitaxial growth of CuSCN(003) nanorods on Au(111)/Si(111) wafer. In paper II, we presented the epitaxial electrodeposition of CuBr(111)/Ag(111) and CuBr(100)/Ag(100) via an epitaxial AgBr buffer layer. In my co-author paper "Banik, A.; Tubbesing, J. Z.; Luo, B.; Zhang, X.; Switzer, J. A. Epitaxial Electrodeposition of Optically Transparent Hole-Conducting CuI on n-Si (111). *Chem. Mater.* 2021, 33, 3220-3227.", we developed an electrochemical approach for the epitaxial growth of CuI(111) thin films on Si(111). In APPENDIX A, we briefly show some results of epitaxial electrodeposition of the low-mismatch CuCl(111) on Si(111) as a potential silicon-based blue LED structure.

**1.2.3. Epitaxial Electrodeposition on Self-Assembled Monolayers.** Functional self-assembled monolayers (SAMs) of thiols on single-crystal metals form two-dimensional soft templates with well-controlled functional surfaces. SAMs have been used for a variety of areas such as controlled crystallization, corrosion protection, biosensors, and pattern fabrication technologies.[221-224] SAMs attract significant attention in nanoscale pattern formation, such as E-beam lithography, micro-contact printing and dip-pen nanolithography.[225-227]

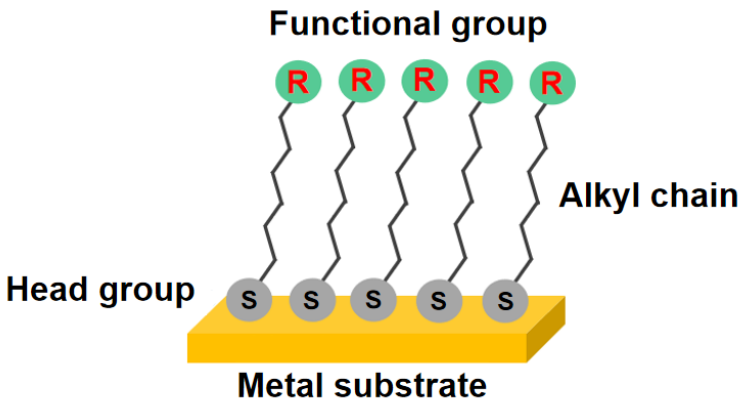


Figure 1.8. Structure diagram of functional alkanethiols on a metal substrate.

Functional alkanethiols on metal surface are the most used SAMs because they can be prepared by immersion in a precursor solution and achieve ordered atomic arrangement. The structure of functional alkanethiol SAM contains head group connecting with the metal substrate (normally via a strong Au-S bond), alkyl chain and functional group on top of SAM, as shown in Figure 1.8. Normally, alkanethiols SAMs are reported to be arranged in a ( $\sqrt{3}$ x $\sqrt{3}$) R30° or c(4 x 2) structure on the Au(111) surface.[228]

**1.2.3.1. Epitaxial growth on self-assembled monolayers.** A SAM surface with functionality enables growth of ordered crystalline materials including MOFs, calcite, and organic semiconductors.[229-231] The functional group of the SAM is crucial to controlling the epitaxial growth and orientation of crystals. H-terminated alkanethiol SAMs are usually hydrophobic and lack control of nucleation and growth, so deposited materials are often polycrystalline. Polar functional groups such as -COOH, $-NH_2$, -OH, $-SO_3^{2-}$, $PO_3^{2-}$ could lead to ordered growth of materials by coordination interaction.[230] For instance, -COOH

terminated alkanethiol SAM have been shown to direct the epitaxial growth of calcite crystals.[232] Furthermore, selection of different acid-terminated SAMs could effectively control the orientations of grown calcite crystals for micro-pattern by micro-contact printing.[230] Ordered crystallization on SAMs has been achieved by vacuum techniques such as CVD and soft-solution processes such as CBD.[233] However, electrochemical epitaxial growth on SAMs still remains a challenge. Potential stability and functionalization of SAM need to be optimized to ensure the epitaxial growth of materials on the SAM. As a soft and compliant organic surface, electrodeposition on SAMs may be easier to minimize the effect of lattice mismatch than on a hard and inorganic substrate. Meanwhile, epitaxial films on soft substrate provide the possibility for a direct lift-off process for flexible devices.[234]

**1.2.3.2. Electrodeposition of metals on self-assembled monolayers.** Metal electrodeposition on SAM has been an important method to achieve micro-patterned metal electrodes.[235,236] SAM covered surfaces also enable lift-off processes to prepare free-standing metal patterns for flexible devices or molds/replicas for micro-contact printing.[237] Metal electrodeposition is achieved by defect-mediated electrodeposition or coordination controlled electrodeposition.[238,239] In defect-mediated electrodeposition, the metal nucleates at defects of SAM or SAM-free areas, and then grow into a mushroom-like morphology due to lack of orientation control. In less reported coordination-controlled electrodeposition, the functional groups of the SAM could coordinate with metal ions and

lead to homogeneous growth of metal films such as Pd.[239] However, only polycrystalline, or amorphous metal films were produced by the SAM due to the lack of order of SAMs and unsuitable functional groups. In paper III, we provide a simple method to directly electrodeposit a smooth epitaxial Cu film on the polar L-cysteine SAM/Au(111) surface. XRD analysis, morphology and possible mechanisms are discussed in detail. The future development of that could be the combination of epitaxial growth and nano/micro-pattern techniques of SAM for high-quality MEMS devices.

### 1.3. EPITAXIAL LIFT-OFF FOR FLEXIBLE ELECTRONICS.

As new materials and fabrication technologies emerge, there is great interest in electronic devices that can be produced using flexible substrates, such as flexible displays, wearable solar cells, sensors, and flexible batteries.[240-244] Epitaxial lift-off (ELO) is a processing technique in which epitaxial layers are peeled off from the host substrate. In 1978, Konagai *et al.* first proposed the epitaxial lift-off method to separate a device layer from a GaAs substrate by using HF to selectively etch an AlGaAs sacrificial layer.[245] Epitaxial lift-off process provides a pathway to create highly ordered flexible thin films which can be applied in flexible electronics. A major advantage of epitaxial lift-off is that the obtained foil remains highly in-plane and out-of-plane ordered, which could serve as high quality device compositions. Another advantage is that the inexpensive deposited thin foil could be continuously produced from an expensive crystal substrate after reuse cycles.

This could greatly reduce the cost of producing highly ordered foils. In addition, epitaxial lift-off expands the optical and electrical applications of thin foils. For instance, a 7 nm Au foil from Si substrate was found 80% transparent in the visible range and conductive, which could serve as an excellent transparent flexible electrode in OLED devices.[50]

Conventional epitaxial lift-off process requires a specific etchant to etch the sacrificial layer between the device layer and the substrate.[246,247] In the case of Au foil from a Si substrate, HF etching solution was used to etch the $SiO_x$ layer between Au and Si layer which was formed by photo-oxidation.[50] In paper I, we select a $KI/I_2$ solution to etch the Au layer between CuSCN and Si, then peel off a wafer-sized transparent and flexible CuSCN foil. Since Au is an excellent common inert substrate for epitaxial growth of various materials such as ZnO, $CsPbBr_3$, $PbO_2$, this etching method could be a general approach to producing flexible ceramic foils from Au/Si substrate.

Due to the toxicity of the etchants, time-consuming process and incomplete etching, advanced epitaxial lift-off techniques without etching are developed.[248,249] One approach could be remote epitaxy and lift-off. Yunjo Kim *et al.* confirmed that GaAs(001) homoepitaxially grow on monolayer graphene covered GaAs(001) substrates by CVD deposition.[249] The deposited single-crystalline films could be easily released from the graphene covered substrate without etching and further perform in light-emitting devices. In paper III, we present a method of non-etching epitaxial lift-off of electrodeposited Cu film from L-cysteine SAM/Au which is a 2D soft layer. This Cu foil could further serve as

a substrate to grow other epitaxial semiconductors. We demonstrated that epitaxial $Cu_2O$ layers could be deposited on this foil as a potential solar cell structure.

## 1.4. RESEARCH OBJECTIVES

The following four research objectives were developed based on the goal of achieving epitaxial electrodeposition of wide bandgap p-type semiconductors and copper metal for energy conversion and flexible electronics.

**1.4.1. Epitaxial Electrodeposition of CuSCN Hole Conductor.** The wide bandgap p-type metal pseudohalide semiconductor CuSCN can serve as a transparent hole transport layer in various opto-electronic applications. The first objective of this research is to directly electrodeposit epitaxial CuSCN on Au(111)/Si(111). Paper I shows the detailed results of the deposition process, XRD, SEM, & TEM and epitaxy characterizations.

**1.4.2. Epitaxial Electrodeposition of Cuprous Halides CuBr and CuCl.** The wide bandgap p-type cuprous halide CuBr can serve as a fast responsive short wavelength light detecting material especially for UV sensors or transparent hole transport layer for various opto-electronics. The second objective of this research is to directly electrodeposit epitaxial CuBr film on a Ag substrate. The work on epitaxial electrodeposition of CuBr is shown in Paper II. Meanwhile, cuprous halide CuCl has a high exciton binding energy and close mismatch with Si and, therefore, has the potential to form a Si-based blue LED. In

APPENDIX A, we briefly show some results of epitaxial CuCl(111) on Si(111) including XRD and SEM analysis.

**1.4.3. Epitaxial Electrodeposition of Cu Films on L-cysteine SAM.** Functional SAMs of thiols on single crystal metals are 2D soft organic surfaces for the highly ordered growth of crystalline materials. The third objective of this research is to directly electrodeposit epitaxial Cu on L-cysteine SAM/Au(111). Paper III shows the results of the electrodeposition, XRD, and possible epitaxy mechanisms.

**1.4.4. Epitaxial Lift-Off of Single-Crystal-Like Foils.** Epitaxial lift-off process expands applications of epitaxial thin film as free-standing foils for flexible electronic devices. The fourth objective of this research is to develop metal and semiconductor foils via the epitaxial lift-off process. Paper I shows flexible CuSCN foil production from Si wafer by Au etching and Paper III shows flexible Cu foil production from L-cysteine SAM/Au.

# PAPER

## I. EPITAXIAL ELECTRODEPOSITION OF HOLE-TRANSPORT CuSCN NANORODS ON Au(111) AT THE WAFER SCALE AND LIFT-OFF TO PRODUCE FLEXIBLE AND TRANSPARENT FOILS

*Bin Luo, Avishek Banik, Eric W. Bohannan, Jay A. Switzer**

Department of Chemistry and Graduate Center for Materials Research, Missouri University of Science and Technology, Rolla, MO 65409-1170, USA.

## ABSTRACT

The wide bandgap p-type metal pseudohalide semiconductor copper(I) thiocyanate (CuSCN) can serve as a transparent hole transport layer in various opto-electronic applications such as perovsksite and organic solar cells and light-emitting diodes. The material deposits as one-dimensional CuSCN nanorod arrays, which are advantageous due to their high surface area and good charge transport properties. However, the growth of high-quality epitaxial CuSCN nanorods has remained a challenge. Here, we introduce a low cost and highly scalable room temperature procedure for producing epitaxial CuSCN nanorods on Au(111) by an electrochemical method. Epitaxial CuSCN grows on Au(111) with a high degree of in-plane as well as out-of-plane order with +0.22% coincidence site lattice (CSL) mismatch. The phase of CuSCN that deposits is a function of the $Cu^{2+}/SCN^-$ ratio in the deposition bath. Pure rhombohedral material deposits at higher $SCN^-$

concentrations, whereas a mixture of rhombohedral and hexagonal phases deposits at lower $SCN^-$ concentrations. A Au/epitaxial CuSCN/Ag diode has a diode quality factor of 1.4, whereas a diode produced with polycrystalline CuSCN has a diode quality factor of 2.1. A highly ordered foil of CuSCN was produced by epitaxial lift-off following a triiodide etch of the thin Au substrate. The 400 nm thick CuSCN foil had an average 94% transmittance in the visible range and a 3.85 eV direct bandgap.

Keywords: CuSCN, electrodeposition, epitaxy, perovskite, hole transporting layer.

## 1. INTRODUCTION

Hole transport materials (HTMs) are essential for opto-electronic devices, such as perovskite solar cells and light-emitting diodes.[1-3] CuSCN is a nontoxic, earth-abundant, wide bandgap (3.7 ~ 3.9 eV) p-type metal pseudohalide semiconductor. CuSCN has been steadily gaining attention as a versatile inorganic HTM in stabilized high-efficient perovskite solar cells,[4] standalone solar water splitting devices,[5] light-emitting diodes[6-8] and transistors.[9-11] The basis for the success of CuSCN as an excellent HTM could be attributed to exceptional optical transparency, chemical stability, processing versatility, and good hole-transporting properties.[12] One-dimensional CuSCN nanorods arrays have further attracted attention due to their high surface area and good charge transport properties.[13-15] However, epitaxial growth of CuSCN nanorods with high out-of-plane as well as in-plane order has remained a challenge. Although CuSCN films have been

prepared by various solution processes such as spin coating,[16] electrodeposition[17-19] and SILAR methods,[20] the deposited CuSCN is a polycrystalline film[21-24] or a film with a fiber texture with no in-plane order[25,26] limiting its hole transport property. Charge carrier transport across the CuSCN layer is affected by grain boundaries and the crystalline orientation, and would be especially impacted for in-plane transport. The hole mobility ($0.01 \sim 0.1$ $cm^2$ $V^{-1}s^{-1}$) of solution-processed CuSCN is still quite limited compared with other inorganic HTMs.[27-29] A highly-ordered hole transporting layer provides a low density of defect sites and grain boundaries suppressing charge recombination probabilities and facilitating efficient charge transport.[5] For example, single crystal spiro-OMeTAD exhibits remarkable mobility, exceeding their thin-film counterparts by three orders of magnitude via mesoscale ordering.[30] In addition, epitaxial hole conducting CuSCN films could serve as substrates for growth of single crystalline perovskite materials or n-type ZnO layers for high-quality opto-electronic devices.[31] Epitaxial CuSCN also allows for the measurement of electronic properties along specific crystallographic directions. This is especially important for non-cubic materials such as CuSCN. Therefore, there is a pressing need to find a method to produce epitaxial CuSCN.

Electrodeposition is a low cost and highly scalable deposition process producing epitaxial metal and semiconductor films.[32-34] Here, we detail an electrochemical method to produce epitaxial CuSCN nanorods on a Au(111)/Si(111) substrate at room temperature from an aqueous $CuSO_4$-EDTA-KSCN bath. The material is deposited on a 28 nm thick

layer of Au(111) on a Si(111) wafer that was electrodeposited by a method that we reported earlier.[33] The Cu(II) is simply reduced electrochemically in the presence of $SCN^-$ ions. Highly out-of-plane and in-plane ordered nanorods grow from the Au(111) surface with a low CSL mismatch of +0.22%. Two kinds of CuSCN nanorods with pure rhombohedral phase and mixed rhombohedral/hexagonal phases were produced by adjusting the $Cu^{2+}/SCN^-$ ratio in the deposition bath. Epitaxial CuSCN/Au is an ideal HTM/metal system due to well-aligned work function for ohmic contact and efficient charge transport. However, it faces challenges such as degradation of the CuSCN/Au interface[4] and the limitation of flexibility due to the rigid substrate. Therefore, epitaxial lift-off technology was applied to a flat epitaxial CuSCN film through a simple chemical Au etching with triiodide ion and lift-off procedure which extends the application of highly ordered CuSCN foils to various substrates via a dry-transfer method. This could form the basis of transparent hole-transporting layers for flexible opto-electronics.[35]

## 2. RESULTS AND DISCUSSION

The electrolyte used for the deposition of CuSCN was typically 20 mM $CuSO_4$, 20 mM EDTA, and 80 mM KSCN based on work by other workers who have shown that complexing agents such as EDTA are needed to prevent the precipitation of black $Cu(SCN)_2$, which further decomposes to white CuSCN and thiocyanogen.[18] According to the speciation study of this earlier study the primary species present in this solution is

Cu(II)EDTA with a lower concentration of $CuSCN^+$.[18] Hence, the EDTA serves as a reservoir of Cu(II) ions which keeps the concentration of $CuSCN^+$ low in order to prevent the precipitation/decomposition.

We explored the electrochemistry of the deposition using a rotating disk electrode (RDE), which provides well-controlled convection to the electrode surface. Using the RDE, a solution reduction reaction should manifest itself as a mass-tranport-limited plateau with a limiting current. Figure 1 shows linear sweep voltammetry (LSV) analysis of various electrolytes with Au RDE at 1000 rpm rotation rate. Figure 1A shows the LSV with a Au RDE in the $CuSO_4$-EDTA-KSCN bath. We observed three cathodic regimes, C1, C2, and C3. The reduction C1 begins at +0.35 V and reaches a plateau with a current density of 1.3 $mA/cm^2$, indicating a solution species reduction, whereas the reaction at C2 presents itself as a peak, which indicates a surface species reduction that is not mass-transport-limited. We attribute C1 to the reduction of solution $CuSCN^+$ to solid CuSCN as shown in Eq. 1.

As shown in Figure 1A, although the range of CuSCN deposition is quite wide, from +0.3 to -0.5 V, epitaxial CuSCN is only achieved using a prepolarized bias of -0.3 to -0.5 V. That is, epitaxial CuSCN is only deposited at potentials negative of the peak at C2. In order to further study the nature of reduction process C2, we pre-deposited CuSCN to a thickness of approximately 250 nm on the Au RDE at -0.4 V for 60 s and then performed LSV in the $CuSO_4$-EDTA-KSCN bath as shown in Figure 1B. In this case C2 is absent, suggesting that C2 is due to the reduction of a surface adsorbed species on the Au surface.

Because the current density at C2 in Figure 1A is higher than that of a self-assembled monolayer, combined with the fact that $SCN^-$ is known to be strongly adsorbed on the Au(111) surface,[37] we speculate that C2 is the reduction of an adsorbed $Cu(II)_xEDTA_y(SCN)_z$ cluster[18,36,38] on the Au surface that is attached by Au-SCN interaction, as given in Eq. 2. To understand the effect of EDTA on the electrochemistry, we performed LSV using the Au RDE in a $CuSO_4$-KSCN bath without EDTA and shown in Figure 1C, in which C1 appears as a cathodic plateau with 9 $mA/cm^2$ that is 7 times higher than the $CuSCN^+$ reduction plateau in the $CuSO_4$-EDTA-KSCN bath in Figure 1B. The higher current density for C1 in this bath indicates that the EDTA does serve to lower the concentration of $CuSCN^+$ in solution. The voltammogram in this solution lacks reduction process C3, suggesting that C3 in Figures. 1A and 1B is due to the reduction of Cu(II)EDTA to Cu (in Eq. 3). The deposition solution that does not contain EDTA is not stable for more than a few minutes because of the spontaneous precipitation of CuSCN and $Cu(SCN)_2$ powder as shown in the typical XRD pattern in Figure S1. Figure 1D shows the LSV of a Au RDE in a solution of 20 mM $CuSO_4$ and 20 mM EDTA (i.e., no $SCN^-$ present). In this case C1 and C2 are not observed. The only reduction process (C3) is the reduction of Cu(II)EDTA to metallic Cu, as shown in Eq. 3.

$$Cu(II)SCN^+ + e^- = Cu(I)SCN \quad (1)$$

$$Cu(II)_xEDTA_y(SCN)_z \text{ (adsorbed cluster)} + xe^- = xCuSCN + (z-x)SCN^- + yEDTA \quad (2)$$

$$Cu(II)EDTA + 2e^- = Cu(0) + EDTA \quad (3)$$

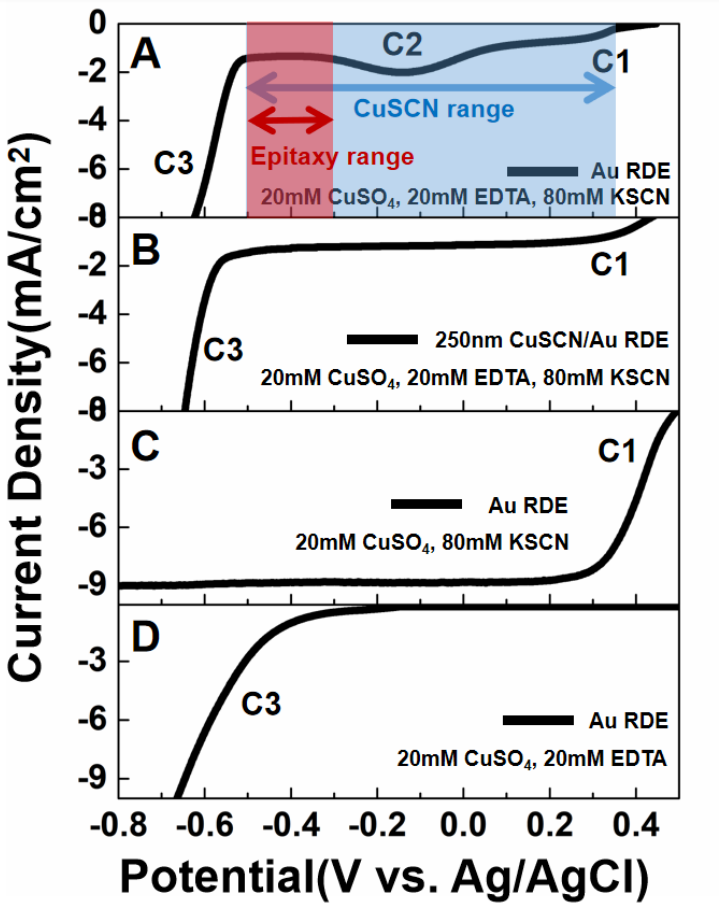


Figure 1. Linear sweep voltammograms (LSVs) of electrolytes with various compositions. (A) Au rotating disc electrode (RDE) in 20 mM $CuSO_4$, 20 mM EDTA, 80 mM KSCN solution; (B) CuSCN (250 nm )/Au RDE 20 mM $CuSO_4$, 20 mM EDTA, 80 mM KSCN solution. 250 nm CuSCN was pre-deposited at -0.4 V vs. Ag/AgCl for 60 s; (C) Au RDE in 20 mM $CuSO_4$, 80 mM KSCN solution; (D) Au RDE in 20 mM $CuSO_4$, 20 mM EDTA solution. RDEs were rotated at 1000 rpm. Scan rate of all LSVs were 10 $mV \cdot s^{-1}$.

Epitaxial CuSCN is only achieved using a prepolarized potential of -0.3 to -0.5 V as shown in Figure 1A. CuSCN deposited at +0.2 V was analyzed by XRD and SEM as shown in Figure S3. It is polycrystalline with a slight [001] preferred orientation in the XRD pattern (Figure S3A) and disordered microstructure (Figure S3B, S3C). The RDE studies in Figure 1 may provide some insight into why the epitaxial CuSCN can only be

produced at potentials negative of C2 in Figure 1A. Material deposited positive of C2 grows on top of the adsorbed $Cu(II)_xEDTA_y(SCN)_z$ clusters, which inhibit the epitaxial nucleation on the Au(111) surface. Consistent with this argument, a short nucleation pulse of a Au(111) electrode at -0.4 V for 10 s followed by growth at -0.1 V for 10 minutes results in epitaxial CuSCN (Figure S4A), whereas constant potential deposition at -0.1V for the same time leads to disordered CuSCN (Figure S4B) without clear spots in the (104) pole figure. Therefore, in this work, epitaxial deposition utilizes a constant potential at -0.4 V, and Figure S5 shows a typical current density-time plot.

An optical image of epitaxial CuSCN on a 2 inch diameter Au(111)/Si(111) wafer is shown in Figure 2A. The CuSCN is deposited on a Au(111)/Si(111) wafer with a 28 nm thick Au(111) layer that was electrodeposited as reported earlier.[33] Although CuSCN is highly optically transparent, the deposited epitaxial CuSCN film shows a colored appearance due to Au layer and light wave interference. The orientation of the deposited epitaxial CuSCN on Au(111)/Si(111) was determined by XRD and pole figure measurement. An XRD pattern of CuSCN/Au(111)/Si(111) is shown in Figure 2B. It exhibits [001] out-of-plane order and is indexed to β-CuSCN. Note that only the {00l} reflections are observed for the CuSCN. The peaks for CuSCN are sharp and intense which is consistent with high crystallinity.

It is well known that β-CuSCN exhibits polytypism resulting from different stacking sequences in the [001] direction. AB type layer stacking corresponds to the

hexagonal 2H structure[39] (JCPDS No. 75-2315) whereas the rhombohedral 3R structure[40] (JCPDS No. 29-0581) with the ABC stacking also exists. 3R CuSCN has lattice parameters a = b = 0.3857 nm, c = 1.6449 nm and R3m (160) space group, whereas 2H CuSCN has lattice parameters a = b = 0.3850 nm, c = 1.0937 nm and $P6_3mc$ (186) space group. In order to determine the polytype of CuSCN, powder XRD analysis was done as shown in Figure S6. Powders are scraped from the substrate and ground into micron-size particles. The powder XRD of the CuSCN shows that the material is the pure 3R phase.

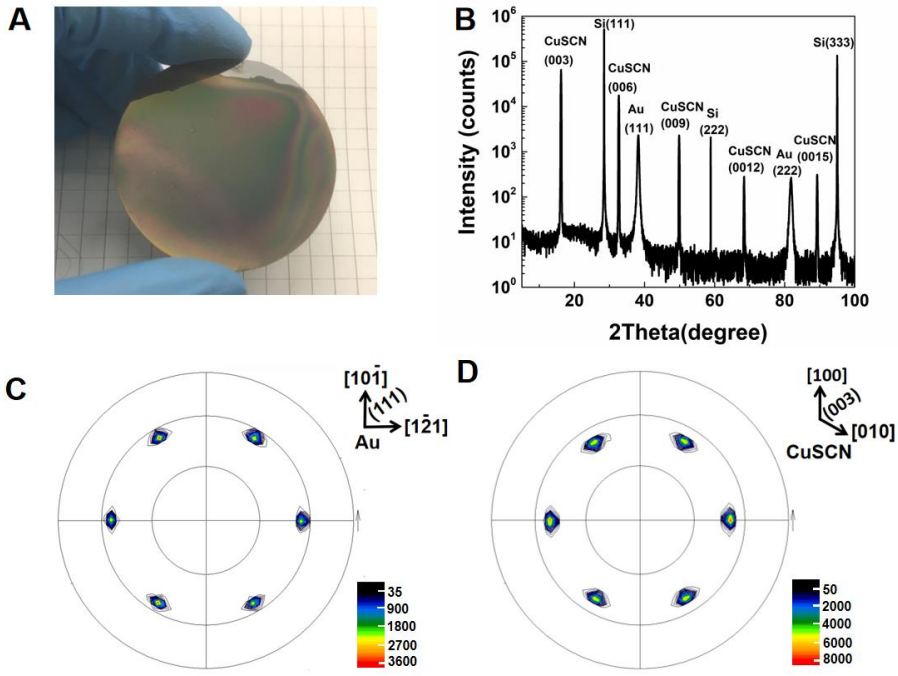


Figure 2. X-ray diffraction pattern and pole figures of epitaxial 3R CuSCN film. (A) Optical image of CuSCN film on 2 inch diameter Au(111)/Si(111) wafer; (B) XRD pattern of 3R CuSCN(003) on Au(111)/Si(111); (C) (200) pole figure of Au(111); (D) (104) pole figure of 3R CuSCN(003). 3R CuSCN was deposited at -0.4 V for 10 minutes in 20 mM $CuSO_4$, 20 mM EDTA, 80 mM KSCN at room temperature.

The in-plane order of 3R CuSCN(003)/Au(111)/Si(111) was determined using pole figures of crystal planes that are not parallel with the surface. The Au(200) pole (Figure 2C) and Si(220) pole (Figure S7) exhibit six spots (tilt angle: 54.74°) and three spots (tilt angle: 35.5°) respectively, as expected and reported earlier.[33] In the case of CuSCN, the (104) pole figure (Figure 2D) of 3R CuSCN(003) shows six intense spots (tilt angle: 50.93°) which are separated azimuthally by 60°. This tilt angle indicates that the angle between the (003) and (104) planes is 50.93°, consistent with the simulated stereographic projection for 3R CuSCN(003) (Figure S8A). Six spots of 3R CuSCN indicate the existence of parallel and antiparallel orientations. Unlike the simulated stereographic projection in Figure S8B, 3R CuSCN does not have spots at $\chi$ of 58.73° in the H(102) pole (Figure S9). This indicates that there is no epitaxial 2H phase, consistent with the powder XRD analysis.

To further confirm that the orientation of CuSCN is directly controlled by Au substrate, we electrodeposited CuSCN on a sputtered Au(111)/glass without in-plane order (Figure S10). The ring pattern in (104) pole of 3R CuSCN (Figure S10A) growing on Au(111) on glass (Figure S10B) confirms the lack of in-plane order of CuSCN. Hence, the Au(111)/Si(111) substrate directly controls the in-plane orientation of the deposited CuSCN. Therefore, 3R CuSCN(003) film grows epitaxially on Au(111)/Si(111), and the epitaxial relationship is 3R CuSCN(003)[100]//Au(111)[$10\bar{1}$]//Si(111)[$10\bar{1}$]. The epitaxial perfection of the 3R CuSCN(003) film was further measured. Azimuthal scans were performed for the (104) pole of 3R CuSCN(003) (tilt angle: 50.93°) and (200) pole of

Au(111) substrate (tilt angle: 54.74°) (Figure 3A). We observe six peaks for both CuSCN and Au, in agreement with pole figure results, corresponding to in-plane parallel and antiparallel domains. The obtained peak/background ratio is 250:1, which confirms a high degree of in-plane order. Rocking curves on 3R CuSCN(003) and Au(111) were done to measure the mosaic spread of CuSCN (Figure 3B). The FWHM (full width at half maximum) was 0.59° for 3R CuSCN(003) and 0.88° for Au(111). The FWHM of 3R CuSCN indicates that the mosaic spread in 3R CuSCN is less than that of Au(111) substrate.

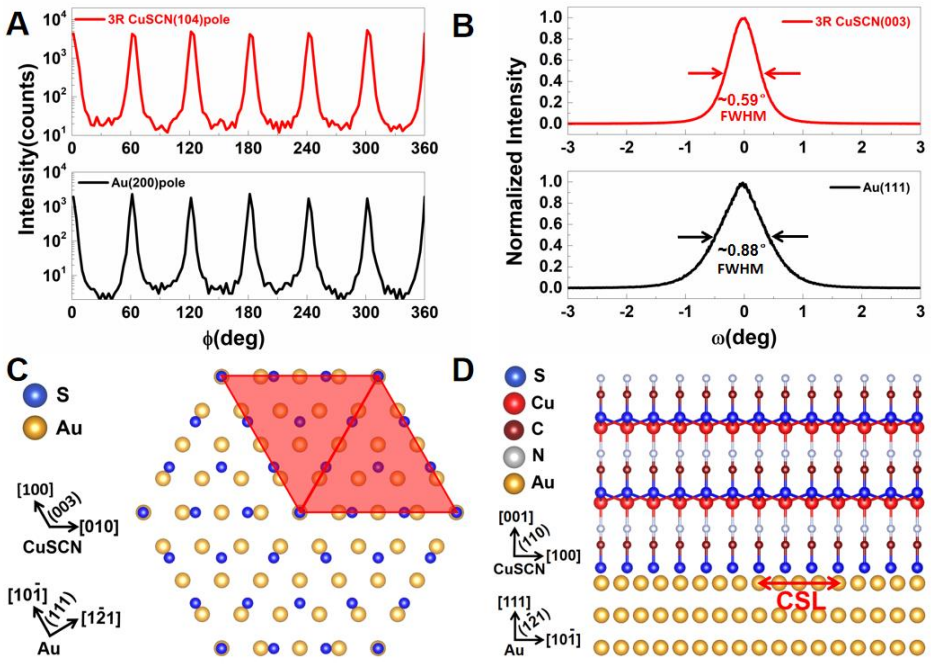


Figure 3. Epitaxial perfection and interface models of 3R CuSCN(003) on Au(111) substrate. (A) Azimuthal scans of 3R CuSCN(003) at $\chi = 50.93°$ and Au(111) at $\chi = 54.74°$ ; (B) X-ray rocking curves for 3R CuSCN(003) and Au(111); (C) In-plane interface model of S (blue) atoms of 3R CuSCN(003) with Au(111) (orange). 4 S atoms with 5 Au atoms form the coincidence site lattice, which results in a mismatch of +0.22%; (D) Out-of-plane interface model of [001] epitaxial growth of 3R CuSCN(003) on Au(111).

Interface models of 3R CuSCN(003) film on Au(111) substrate are exhibited in Figure 3C and Figure 3D. In the in-plane interface model (Figure 3C) of S atoms with Au(111), Au and S atoms are colored orange and blue, respectively. By the formation of the CSL, in which 4 S atoms align with 5 Au atoms, a mismatch of +0.22% is produced. Antiparallel and parallel domains could both be observed due to rotational twinning. In the out-of-plane interface model (Figure 3D) showing the cross-sectional structure of CuSCN on Au(111), we could observe that the head-tail direction of linear $SCN^-$ ions is parallel with the [001] growth direction.

The morphological features of the 3R CuSCN(003) were determined by SEM and TEM. Plan-view SEM images of electrodeposited 3R CuSCN(003) on Au(111)/Si(111) are shown in Figures. 4A and 4B. In Figure 4A, after deposition for 60 seconds, initial triangular crystals with an average size 300-500 nm formed as a homogeneous seed layer with a 250 nm thickness. The high in-plane order in the image is consistent with the epitaxy of 3R CuSCN(003) on the Au(111)/Si(111). Parallel and antiparallel crystals indicate parallel and antiparallel in-plane orientations, consistent with the pole figure results. CuSCN nanorods with 500-800 nm diameters further grow after deposition for 10 minutes as shown in Figure 4B. The SEM cross-section (Figure 4C) of 3R CuSCN(003) shows the nanorods are dense and vertical to the Au(111)/Si(111) substrate, indicating the preferred [001] orientation. The nanorods formation mechanism was studied. As shown in Figure S11, when the growth potential of CuSCN is changed from + 0.3V to +0.2 V, which

corresponds, respectively, to activation control and mass transport limited control in the LSV in Figure 1A, the morphology changes from the flat film with uniform triangular crystals (Figure S11A), to the initial nanorods (Figure S11B), then to disordered long nanorods (Figure S11C). This shows that nanorods morphology is because of limitation of mass transport, in agreement with a previous report.[22] The high-resolution TEM image indicated that the nanorod grows along the [001] direction, and lattice fringes with 0.28 nm interplanar distance match to the (006) planes of 3R CuSCN.[41]

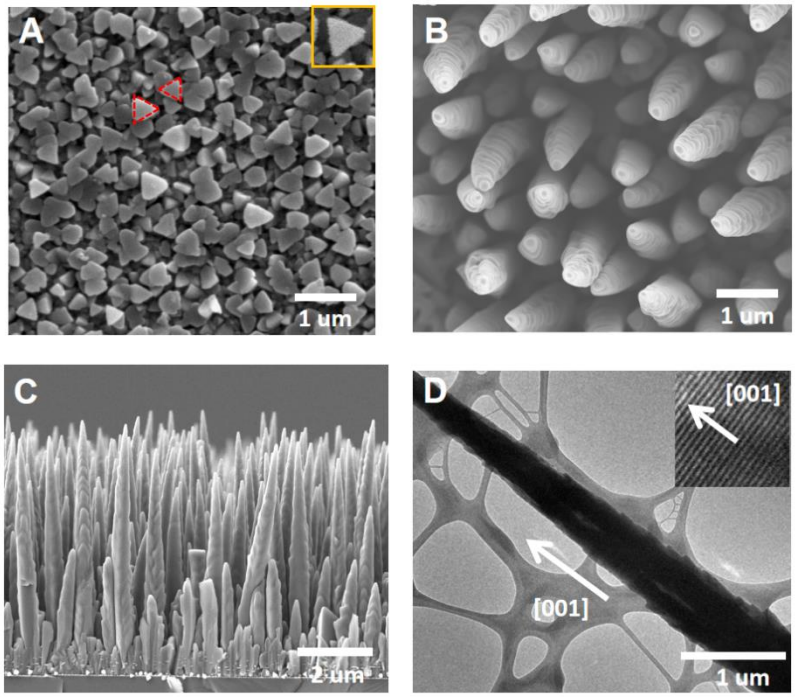


Figure 4. SEM and TEM images of epitaxial 3R CuSCN(003) on Au(111)/Si(111). (A) SEM image (plan-view) of initial 3R CuSCN(003) after 1 minute deposition with 250 nm thickness; (B) SEM image (plan-view) of 3R CuSCN(003) nanorods after 10 minutes deposition; (C) SEM image (cross-sectional view) of 3R CuSCN(003) nanorods after 10 minutes deposition; (D) TEM image of a single 3R CuSCN(003) nanorod and HRTEM image showing 0.28 nm interplanar distance. 3R CuSCN was deposited at -0.4 V in 20 mM $CuSO_4$, 20 mM EDTA, 80 mM KSCN at room temperature.

Although the 3R CuSCN rods are epitaxial, they lack a continuous film underneath the rods, which may cause leakage or short circuits in electronic devices. Therefore, we developed another continuous epitaxial CuSCN with mixed hexagonal and rhombohedral phases (2H&3R CuSCN) when deposited from a bath with $Cu^{2+}/SCN^{-}$ = 1/2. The orientations of the 2H&3R CuSCN film are measured by XRD patterns and pole figure analysis. As shown in Figure S12, 2H&3R CuSCN has a [001] orientation that is highly overlapped with 2H and 3R CuSCN. In order to distinguish and quantify compositions of the 2H phase and 3R phases, we did powder XRD analysis of 2H&3R CuSCN. Figure S13 shows mixed peaks for 2H and 3R CuSCN which confirms the existence of two crystal structures of CuSCN in this work. Rietveld refinement of the diffraction pattern gave 53% hexagonal phase and 47% rhombohedral phase (Rwp 7.0%).

As for in-plane orientation, 2H&3R CuSCN has 6 intense spots in both H(102) at $\chi = 58.73°$ (Figure 5A) and R(104) at $\chi = 50.93°$ (Figure 5D) at the same azimuthal angle, indicating that both 2H and 3R phases are epitaxial. The out-of-plane interface model of the 2H phase/Au(111) and the 3R phase/Au(111) are shown in Figure S14. SEM was used to characterize the morphology of 2H&3R CuSCN. After deposition for 2 minutes, initial 100-200 nm hexagonal crystals (Figure 5B) form a compact dense film with a thickness of 500 nm (Figure 5C). The further growth of CuSCN for 15 minutes exhibits a unique morphology with a dense film (5 um thickness) near the Au surface and ordered hexagonal micro-rods (1 ~ 2 um diameter, 20 ~ 40 um length) vertical to the substrate (Figure 5E, 5F)

with a snowflake-like surface which is possibly due to the competition of 2H and 3R phase growth. The micro-rods morphology with large surface area could be favorable for efficient charge transport in various devices.

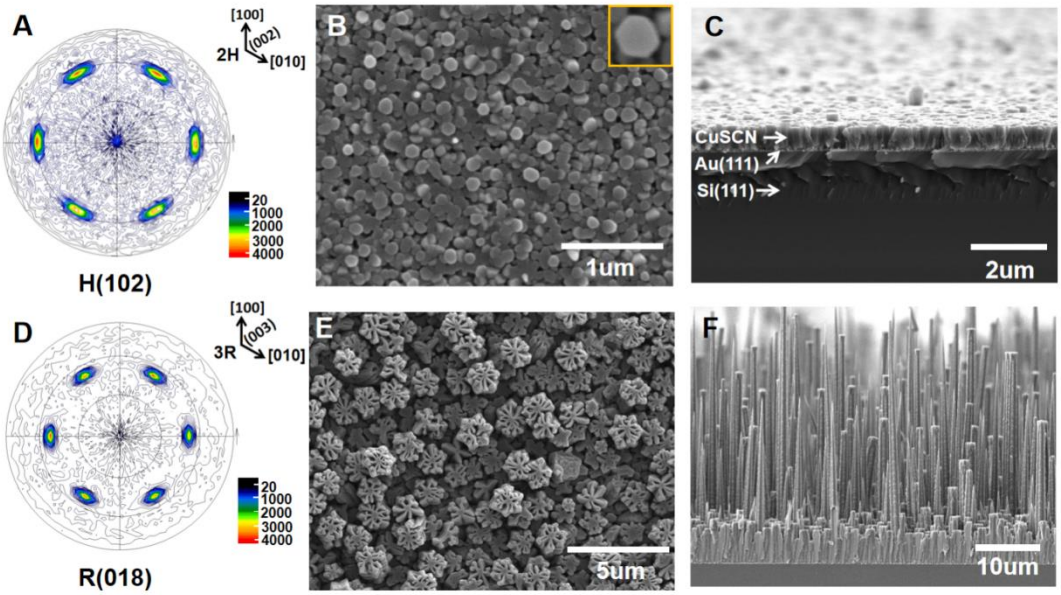


Figure 5. Epitaxial CuSCN with mixed hexagonal and rhombohedral phases. (A) H(102) pole figure for 2H&3R CuSCN; (B) SEM image (plan-view) of 2H&3R CuSCN after 2 minutes deposition; (C) SEM image (cross-sectional view) of 2H&3R CuSCN after 2 minutes deposition with 500 nm thickness; (D) R(104) pole figure for 2H&3R CuSCN; (E) SEM image (plan-view) of 2H&3R CuSCN after 15 minutes deposition; (F) SEM image (cross-sectional view) of 2H&3R CuSCN after 15 minutes deposition. 2H&3R CuSCN was deposited at -0.4 V in 20 mM $CuSO_4$, 20 mM EDTA, 40 mM KSCN at room temperature.

The reason for the effect of the $Cu^{2+}/SCN^-$ ion ratio on the crystal structure of CuSCN is still unclear. A possible hypothesis could be that excess $SCN^-$ ions in solution partially substitute the coordination of Cu(II) with EDTA, and further form $Cu(II)EDTA(SCN)_x$ complex. The complex could be absorbed on the surface of CuSCN in

a specific posture with the low steric hindrance. Then the complex is reduced to CuSCN by releasing EDTA and $SCN^-$. The specific posture causes the Cu-S bond to rotate 120° each time and form 3R packing sequences.

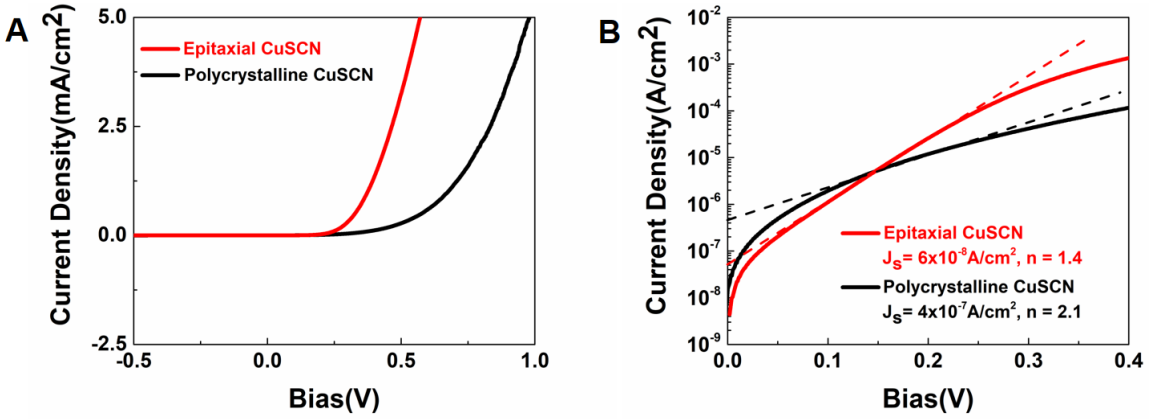


Figure 6. Electronic properties of epitaxial 2H&3R CuSCN. (A) Current density-potential (J-V) plot of Au/CuSCN/Ag diodes; (B) Log(J)-V plot to measure diode quality factor (n) and dark saturation current density ($J_s$). Epitaxial and polycrystalline CuSCN flat films were deposited at -0.4 V and +0.2 V in 20 mM $CuSO_4$, 20 mM EDTA, 40 mM KSCN at room temperature, respectively. The two CuSCN deposits have a constant charge density (0.2 C/cm$^2$) to maintain similar thicknesses (1.2 μm).

The electronic properties of the epitaxial CuSCN were explored by preparing an inorganic heterojunction (Au/CuSCN/Ag). A 2H&3R CuSCN thin flat film with dense and uniform morphology was chosen for fabrication of the diode. The diode was prepared by coating Ag paste on CuSCN to make a rectifying contact (Figure S15A) while Au(111) forms an ohmic contact (Figure S15B).[42] Epitaxial and polycrystalline CuSCN flat films were electrodeposited with the same charge density (0.2 C/cm$^2$) to maintain similar thicknesses (1.2 um) as shown in Figure S16A and Figure S16B, respectively. The cross-

sectional SEM image of Au/epitaxial CuSCN/Ag diode and Au/polycrystalline CuSCN/Ag diode are shown in Figure S16C and Figure S16D. The J-V response of Au/epitaxial CuSCN/Ag exhibits more significant rectifying behavior (Figure 6A). The diode quality factor, n, was used to determine the quality of rectifying behavior. An ideal diode has n = 1.0. In Figure 6B, the epitaxial CuSCN has a diode quality factor of 1.4, whereas a diode produced with polycrystalline CuSCN has a diode quality factor of 2.1. A smaller diode quality factor for epitaxial CuSCN indicates that epitaxy of CuSCN is beneficial to suppressing carrier recombination. The high order and lack of grain boundaries of epitaxial CuSCN could also improve carrier mobility which is favorable to various electronic devices such as perovskite solar cells.

The schematic for epitaxial lift-off of 2H&3R CuSCN foil is shown in Figure 7A. A flat epitaxial 2H&3R CuSCN film (Figure 5C) grows initially on the Au buffer layer on the Si wafer. The Au can then be etched in $KI/I_2$ for effortless lift-off by commercial adhesive tape. Si could be reusable after each fabrication cycle. The result confirms the exceptional chemical stability of CuSCN. Figure 7B shows the photograph of a continuous transparent 2H&3R CuSCN foil with a thickness of 400 nm. The out-of-plane order of the 2H&3R CuSCN foil was confirmed by the XRD pattern in Figure 7C, which only exhibits the {001} family of peaks. The in-plane order was demonstrated by a R(104) pole figure which has six spots (tilt angle: 50.93°) separated azimuthally by 60° (Figure 7D). Hence the 2H&3R CuSCN foil remains highly ordered after Au etching. Figure 7E shows the

optical transparency of the 400 nm thick 2H&3R CuSCN foil. The transmittance spectrum shows 94% average transmittance in the visible range (400 ~ 800 nm). The Tauc plot in Figure 7E shows a 3.85 eV direct band gap, which is exceptionally large compared with other Cu(I)-based p-type semiconductors. The surface of 2H&3R CuSCN foil remained continuous and featureless without cracks after 1000 bending cycles (Figure S17). The highly ordered 2H&3R CuSCN foil could form the basis of future transparent and flexible electronics.

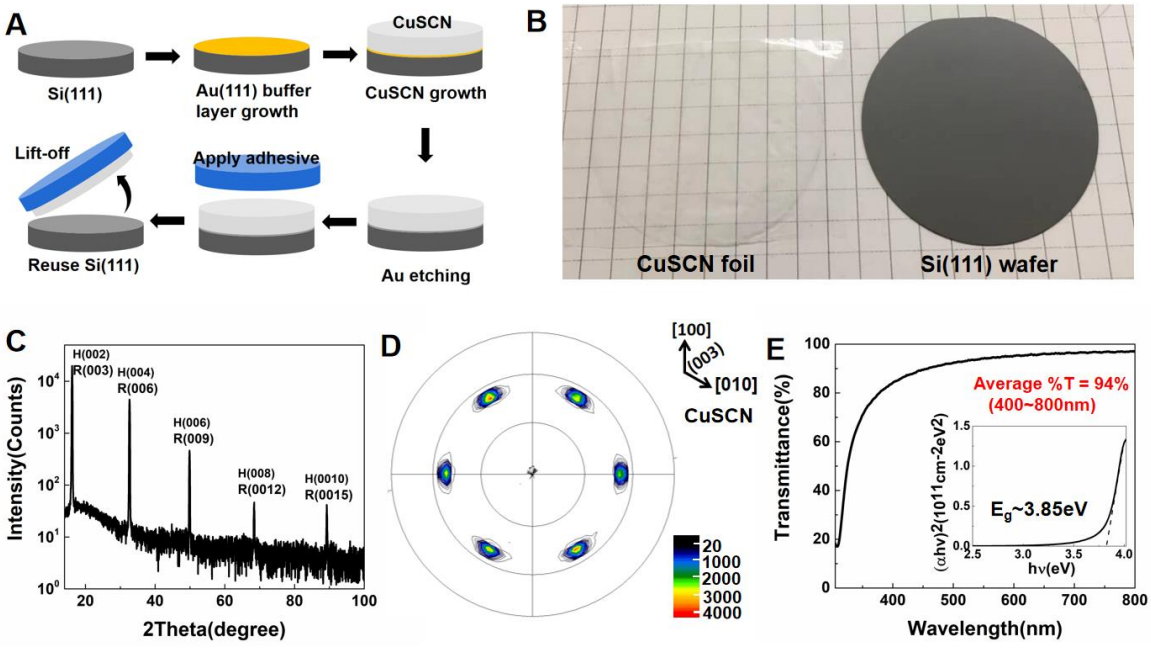


Figure 7. Epitaxial lift-off of highly ordered 2H&3R CuSCN transparent foils. (A) Schematic for epitaxial lift-off 2H&3R CuSCN foil: growth of CuSCN on Au/Si and the following Au etching by $KI/I_2$ solution produce flexible CuSCN foil which could be detached by commercial tape; (B) Photograph of transparent, highly-orderd 2H&3R CuSCN (2 inch diameter) foil with 400 nm thickness; (C) X-ray diffraction pattern of 2H&3R CuSCN foil; (D) R(104) pole figure of 2H&3R CuSCN foil; (E) UV-vis transmittance spectra of 400 nm 2H&3R CuSCN foil showing average 94% transmittance in 400-800 nm visible range and Tauc plot showing 3.85 eV direct bandgap.

# 3. CONCLUSION

We demonstrate an electrochemical method for depositing epitaxial hole transporting CuSCN nanorods with a [001] orientation on the Au(111) surface. CuSCN with the pure 3R structure and 2H & 3R mixture were produced by adjusting the $Cu^{2+}/SCN^-$ ratio in the deposition solution. Epitaxial CuSCN/Au forms an ideal HTM/metal system for various opto-electronic devices. Here, a diode is produced by forming the Au/epitaxial CuSCN/Ag heterojunction. This work also opens interesting avenues for other epitaxial hole transporting layers such as NiO and $CuAlO_2$. Good chemical stability of CuSCN allows Au etching and epitaxial lift-off to produce a CuSCN foil with high optical transparency and large bandgap. The highly ordered 2H&3R CuSCN foil has possible applications such as an efficient HTM in perovskite solar cell via dry-transfer method and flexible transparent electrode. This Au etching method shown here could be a general way to produce various flexible ceramic foils growing on a Au substrate, such as $Bi_2O_3$ and $PbO_2$.

# 4. MATERIALS AND METHODS

## 4.1. Si WAFER PROCESSING FOR Au DEPOSITION

Si(111) wafers (phosphorus-doped, N-type, 0.1-2.0 Ω·cm, Virginia Semiconductor Inc.) were used in this work. RCA procedures were applied to completely remove

organic/inorganic impurities on Si surface. In/Ga alloy was coated on the back of wafers, and then a silver wire was attached by silver paste to achieve good electrical contact. In order to prevent electrodeposition on the back, an insulating layer of Apiezon Type W wax was coated and fully dried. Before use, hydrogen-terminated Si surface was produced by washing wafers with dilute (5%) hydrofluoric acid solution for 30-45 s at room temperature. The Au(111) deposition process (using an Autolab 30 potentiostat) followed our previous report in a three electrode system using Si as working electrode.[33] The epitaxial Au(111) films were grown to a thickness of 28 nm.

## 4.2. ELECTRODEPOSITION OF CuSCN AND FOIL FABRICATION

Electrodeposition of rod-like CuSCN was performed in an aqueous $CuSO_4$-EDTA-KSCN system as previously reported.[17,18,23] The solution was prepared by dissolving 20 mM $Cu(SO_4)\cdot 5H_2O$, 20 mM ethylenediaminetetraacetic acid (EDTA), and various concentrations of KSCN. The concentration of KSCN for 3R CuSCN and 2H&3R CuSCN were 80 mM and 40 mM, respectively. CuSCN films were electrodeposited at a constant potential at -0.4 V on the Au(111)/Si(111) substrate with 300 rpm stirring. A CuSCN foil was produced by immersion in aqueous 0.3 M $I_2$ and 0.6 M KI solution for 60 seconds to completely etch the Au layer. The CuSCN foil was detached from Si substrate by commercial (3M) adhesive tape. It could also serve the basis for future flexible and transparent electronic devices.

## 4.3. ELECTROCHEMICAL ANALYSIS

LSVs were acquired on an Autolab 30 potentiostat using a Au RDE (3 mm diameter) at 1000 rpm rotation rate. The potential scan rate was 10 mV/s and the step size was 1 mV.

## 4.4. DIODE FABRICATION

Au/CuSCN/Ag was fabricated by coating silver print II (GC electronics) on CuSCN/Au/Si. Silver wires were then connected to the silver print and the Au surface, respectively. The values of Au/ CuSCN/Ag diode factor were determined by devices with the same area of 0.25 $cm^2$.

## 4.5. X-RAY DIFFRACTION, SEM AND TEM MEASUREMENTS

X-ray diffraction patterns, pole figures and azimuthal scans were run on a high-resolution Philips X'Pert Materials Research diffractometer using accessories and procedures outlined in our previous report.[43] SEM was done on a FEI Helios Nanolab microscope, and TEM was done on a FEI Tecnai F20 microscope.

**SUPPLEMENTARY INFORMATION**

# EPITAXIAL ELECTRODEPOSITION OF HOLE-TRANSPORT CuSCN NANORODS ON Au(111) AT THE WAFER SCALE AND LIFT-OFF TO PRODUCE FLEXIBLE AND TRANSPARENT FOILS

*Bin Luo, Avishek Banik, Eric W. Bohannan, Jay A. Switzer**

Missouri University of Science & Technology, Department of Chemistry and Graduate Center for Materials Research, Rolla, MO 65409-1170, USA.

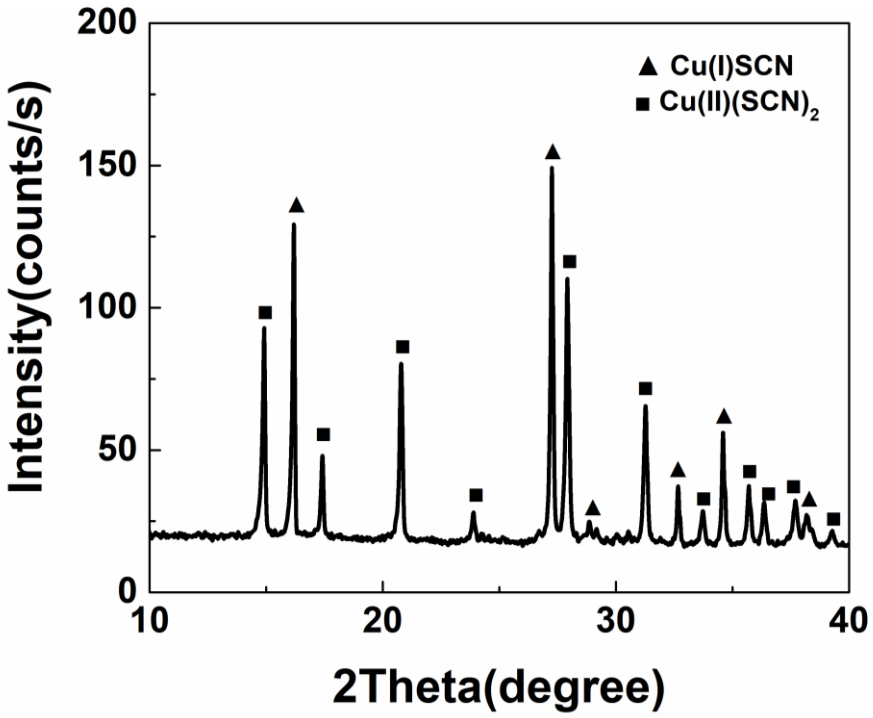


Figure S1. Powder XRD pattern of powder produced by spontaneous precipitation of Cu(I)SCN and $Cu(II)(SCN)_2$ in $CuSO_4$-KSCN bath.

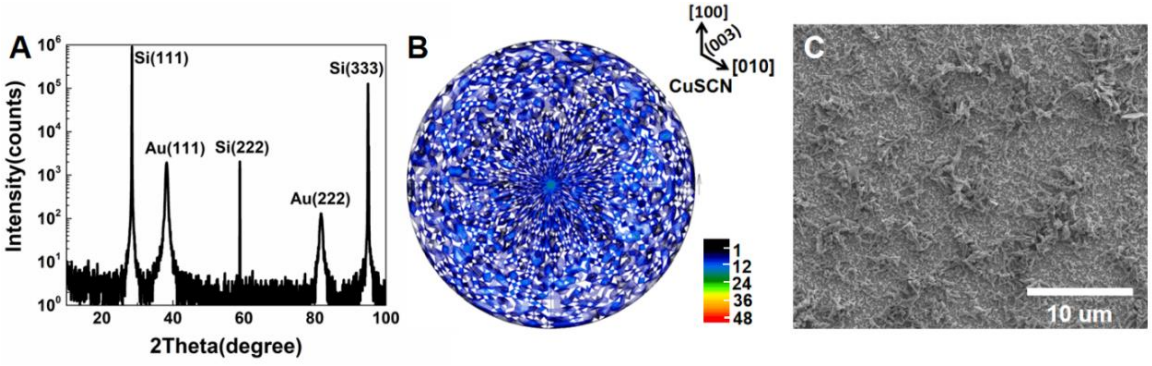


Figure S2. (A) X-ray diffraction pattern of nearly amorphous CuSCN deposited at -0.4 V vs. Ag/AgCl in 20 mM $CuSO_4$ and 80 mM KSCN at room temperature; (B) (104) pole figure of CuSCN; (C) Plan-view SEM image of CuSCN deposited in the same solution.

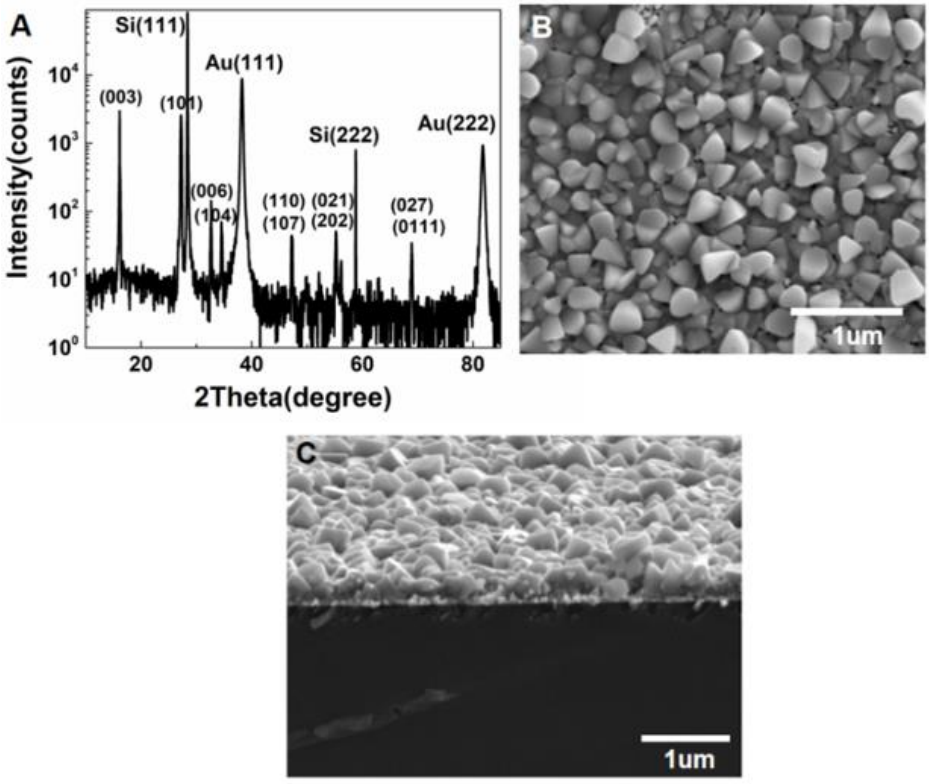


Figure S3. (A) X-ray diffraction pattern of polycrystalline CuSCN with preference in [001] orientation deposited at +0.2 V vs. Ag/AgCl in 20 mM $CuSO_4$, 20 mM EDTA, 80 mM KSCN at room temperature; (B) Plan-view SEM image of CuSCN deposited in the same solution; (C) Cross-sectional view SEM image of CuSCN deposited in the same solution.

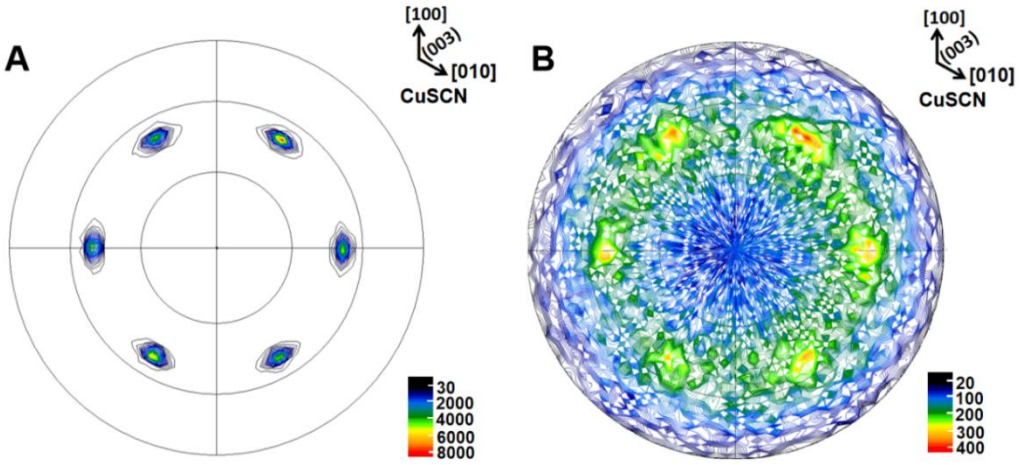


Figure S4. (A) X-ray pole figure (104) of CuSCN deposited -0.4 V vs. Ag/AgCl for 10 s followed by -0.1 V vs. Ag/AgCl for 10 minutes; (B) (104) pole figure of CuSCN deposited at -0.1 V vs. Ag/AgCl for 10 minutes. Solution: 20 mM $CuSO_4$, 20 mM EDTA, 80 mM KSCN.

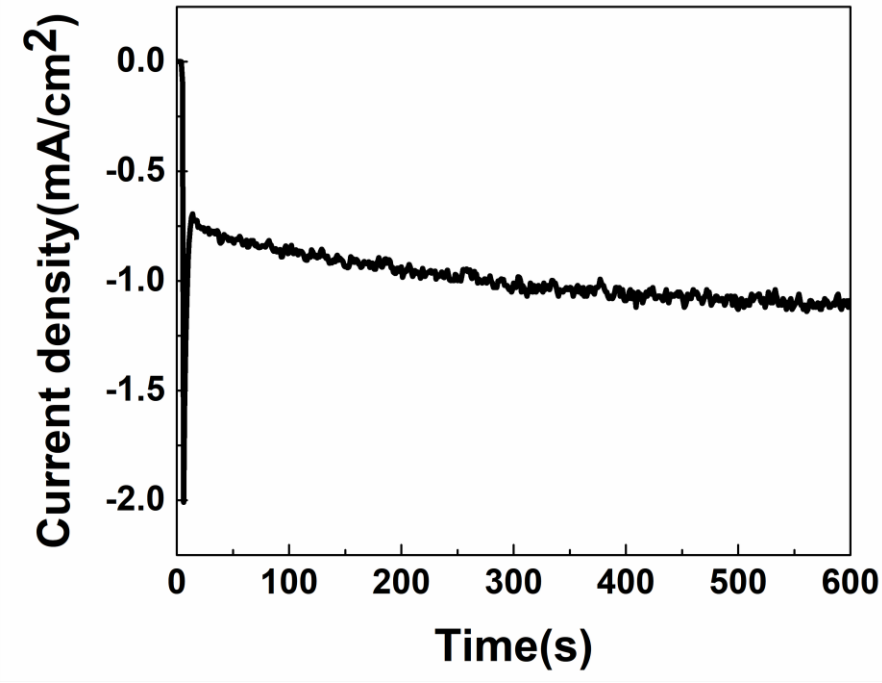


Figure S5. Typical current density-time plot of CuSCN deposited at -0.4 V vs. Ag/AgCl for 10 minutes in 20 mM $CuSO_4$, 20 mM EDTA, 80 mM KSCN at room temperature.

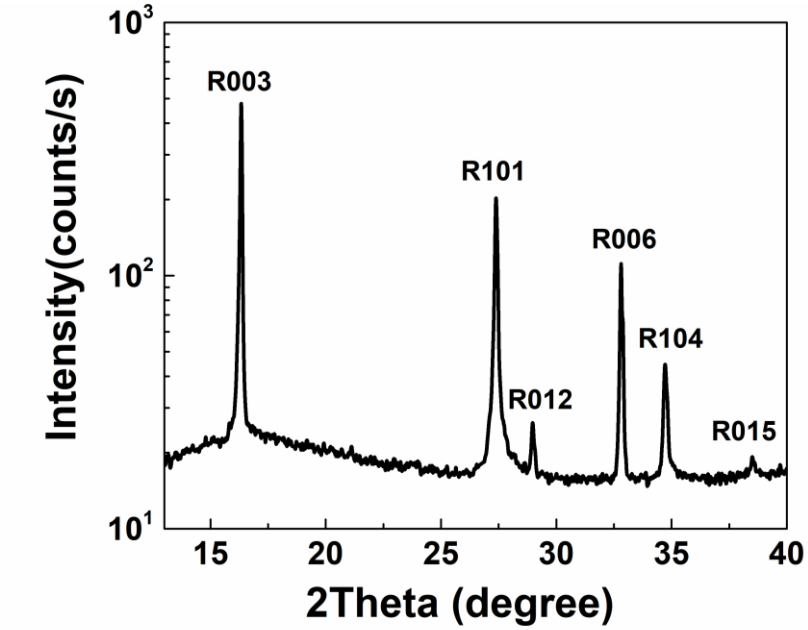


Figure S6. X-ray diffraction pattern of 3R CuSCN powder showing peaks that belong to pure rhombohedral structure. The XRD still shows a slight [001] preference possibly due to the nanorod morphology.

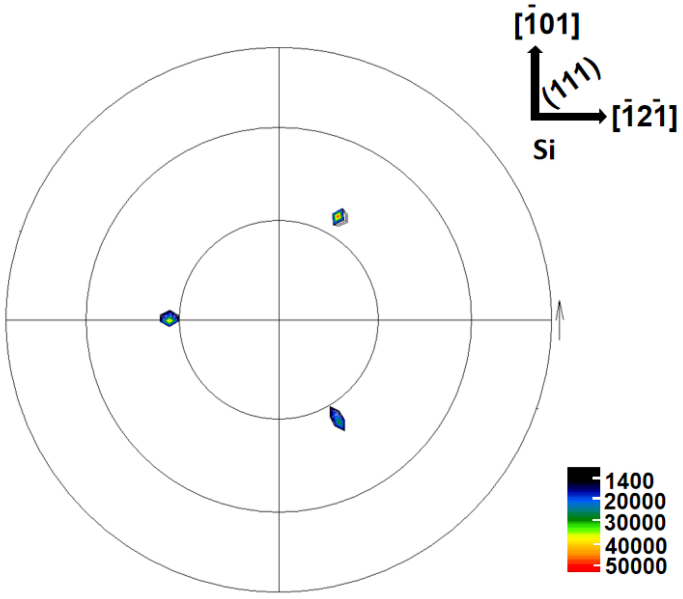


Figure S7. X-ray pole figure (220) of Si(111).

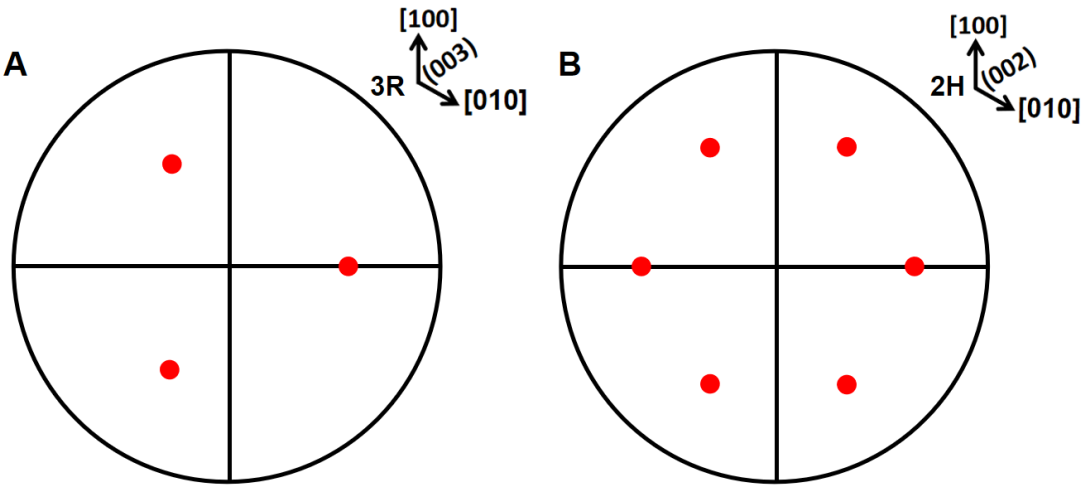


Figure S8. (A) Calculated (104) stereographic projection for rhombohedral 3R CuSCN(003), $\chi = 50.93°$; (B) calculated (102) stereographic projection for hexagonal 2H CuSCN(002), $\chi = 58.73°$.

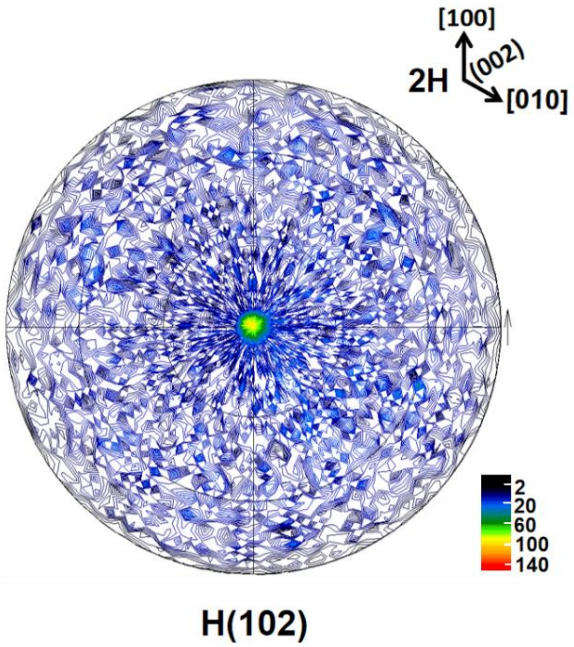


Figure S9. X-ray pole figure H(102) pole figure for 3R CuSCN(003).

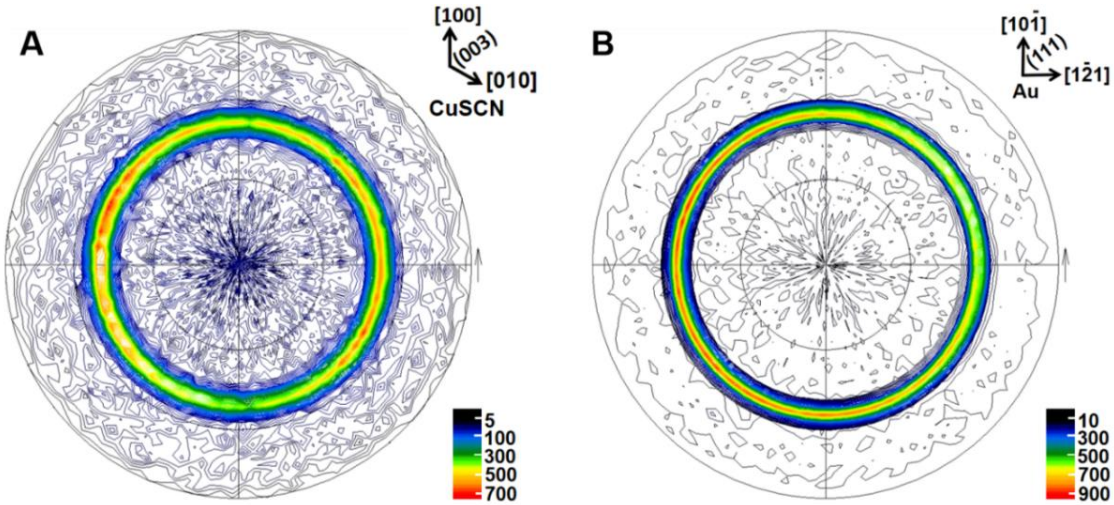


Figure S10. (A) X-ray (104) pole figure for CuSCN deposited on sputtered Au substrate; (B) (200) pole figure for sputtered Au. Sputtered Au on glass has [111] out-of-plane orientation but no in-plane order.

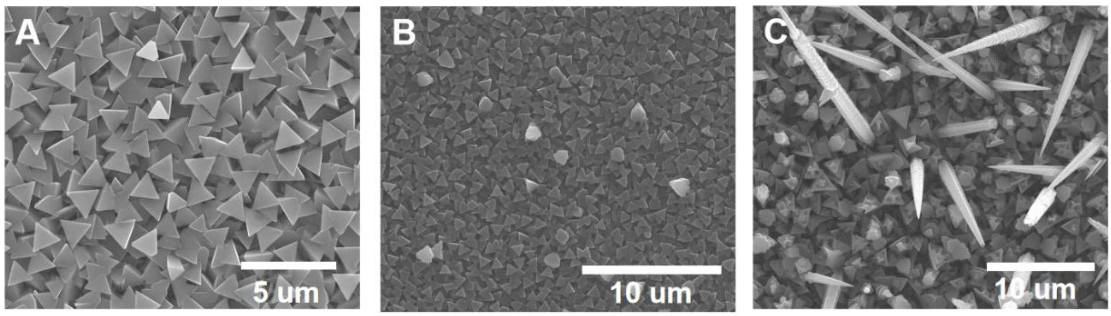


Figure S11. Formation of CuSCN nanorods due to mass transport limitation. CuSCN was nucleated at -0.4 V for 10 s and then grown for various potentials for 15 minutes in 20 mM $CuSO_4$, 20 mM EDTA, 80 mM KSCN at room temperature. (A) SEM image of CuSCN growing at +0.3 V vs. Ag/AgCl under activation control in Figure 1A; (B) SEM image of CuSCN growing at +0.25 V vs. Ag/AgCl close to mass-transport-limited plateau in Figure 1A; (C) SEM image of CuSCN growing at +0.2 V vs. Ag/AgCl on mass-transport-limited plateau in Figure 1A.

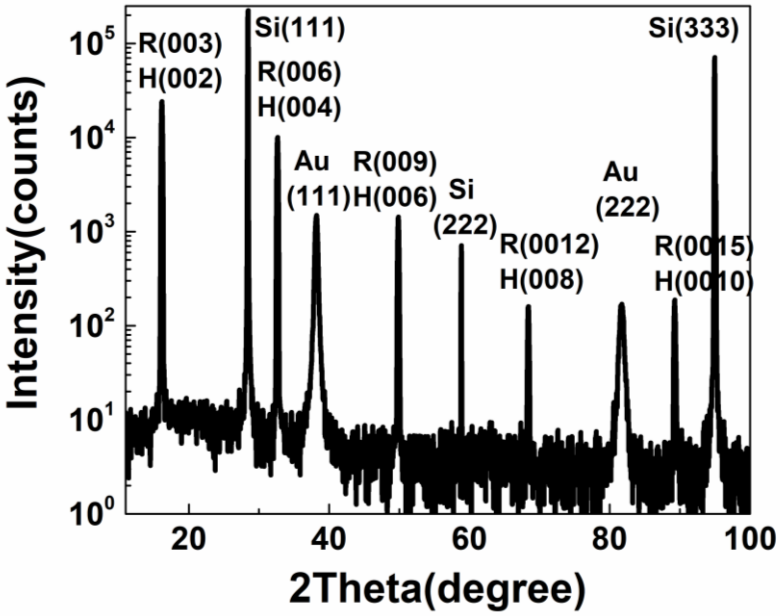


Figure S12. X-ray diffraction pattern of 2H & 3R CuSCN film deposited at -0.4V vs. Ag/AgCl in 20 mM $CuSO_4$, 20 mM EDTA, 40 mM KSCN.

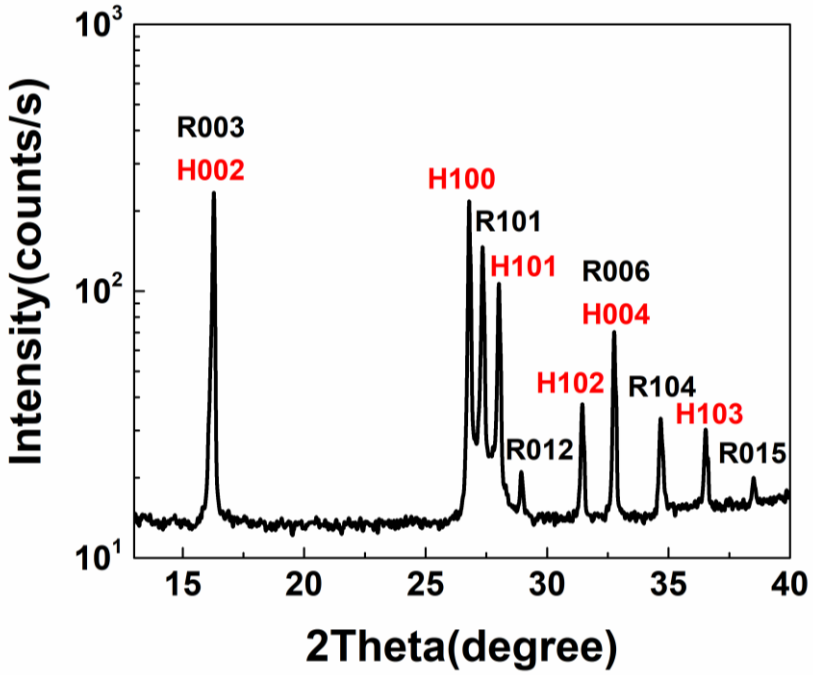


Figure S13. X-ray diffraction pattern of 2H&3R CuSCN powder showing peaks belonging to hexagonal and rhombohedral structures. Rietveld refinement showed that powder was 53% hexagonal and 47% rhombohedral (Rwp 7.0).

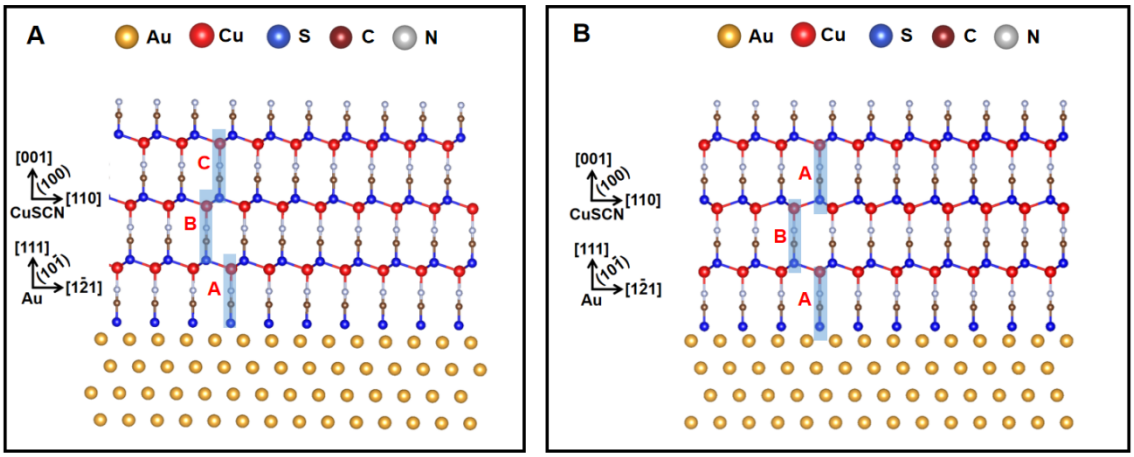


Figure S14. (A) Out-of-plane interface model of 3R CuSCN(003)/Au(111); (B) Out-of-plane interface model of 2H CuSCN(002)/Au(111).

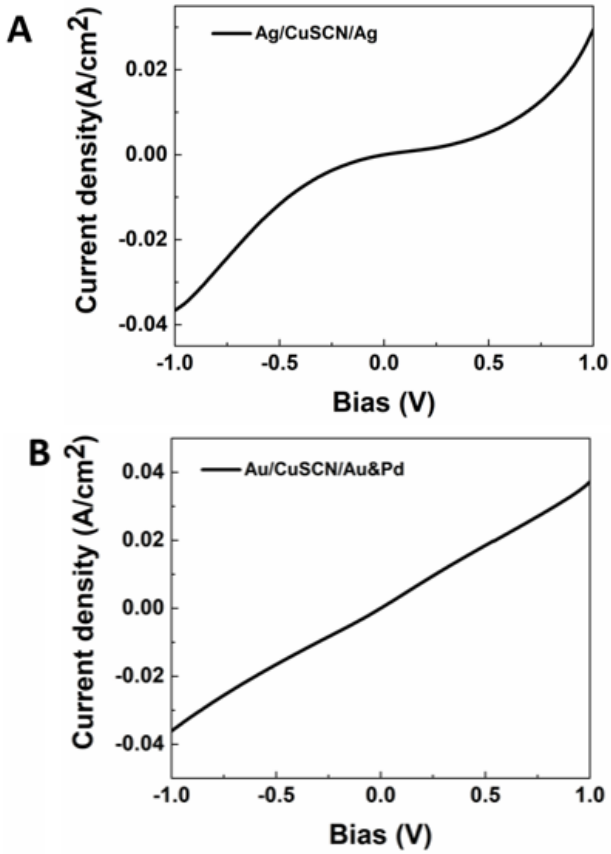


Figure S15. (A) Current density-voltage (J-V) plot of Ag/CuSCN/Ag; (B) J-V plot of Au/CuSCN/Au&Pd. The two Ag contacts form a back-to-back Schottky diode, and the two Au contacts form an ohmic contact.

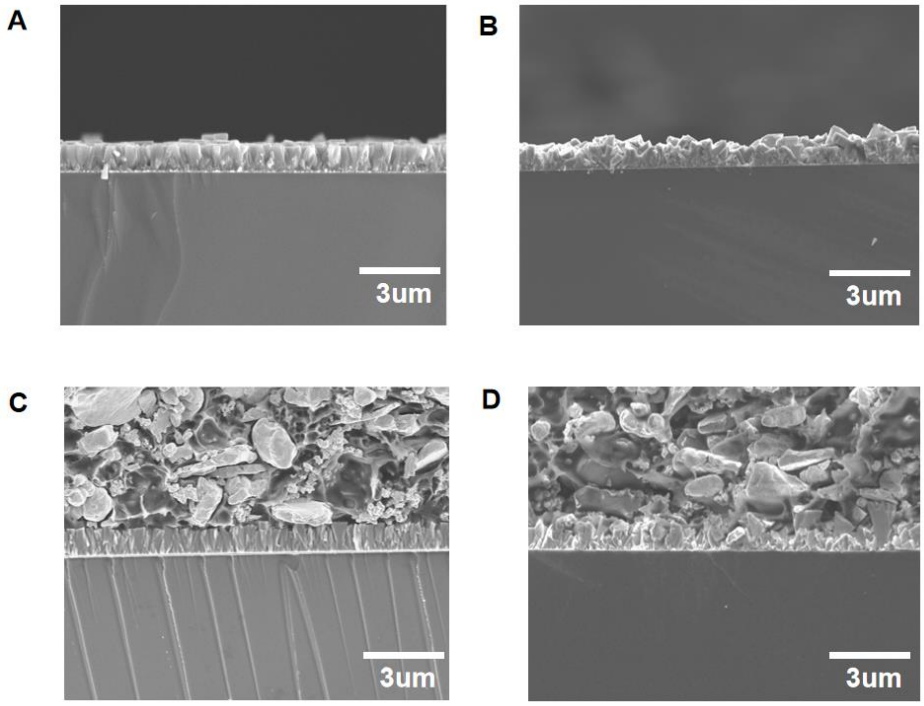


Figure S16. (A) Epitaxial CuSCN flat film growing at -0.4 V vs. Ag/AgCl for 0.2 C/cm$^2$; (B) Polycrystalline CuSCN flat film growing at +0.2 V vs. Ag/AgCl for 0.2 C/cm$^2$; (C) Ag paste on epitaxial CuSCN flat film with 0.2 C/cm$^2$; (D) Ag paste on polycrystalline CuSCN flat film with 0.2 C/cm$^2$. 2H&3R CuSCNs were deposited in 20 mM $CuSO_4$, 20 mM EDTA, 40 mM KSCN at room temperature.

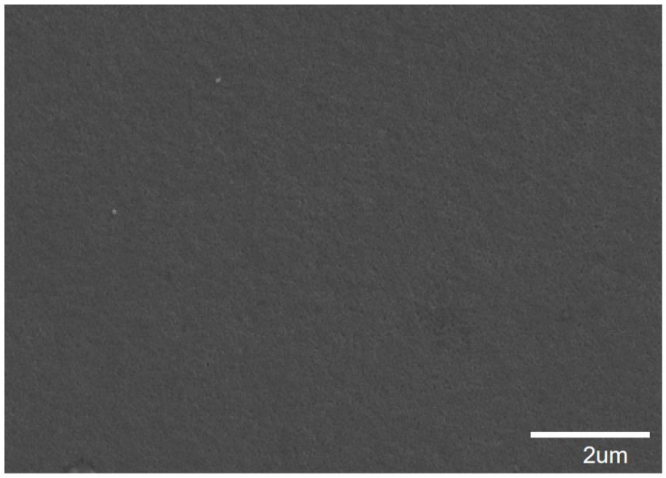


Figure S17. Scanning electron microscopic image of single-crystal-like CuSCN foil showing the face detached from Au after 1000 bending cycles. There are no apparent cracks in the foil after the 1000 bending cycles.

## ACKNOWLEDGMENTS

This material is based on work supported by the U.S. Department of Energy, Office of Basic Energy Sciences, Division of Materials Sciences and Engineering, under grant No. DE-FG02-08ER46518.

## REFERENCES

[1] T. Matsushima *et al.*, "High performance from extraordinarily thick organic light-emitting diodes," *Nature,* vol. 572, no. 7770, pp. 502-506, 2019.

[2] J. Burschka *et al.*, "Sequential deposition as a route to high-performance perovskite-sensitized solar cells," *Nature,* vol. 499, no. 7458, pp. 316-319, 2013.

[3] M. Abdi-Jalebi *et al.*, "Charge extraction via graded doping of hole transport layers gives highly luminescent and stable metal halide perovskite devices," *Science advances,* vol. 5, no. 2, p. eaav2012, 2019.

[4] N. Arora *et al.*, "Perovskite solar cells with CuSCN hole extraction layers yield stabilized efficiencies greater than 20%," *Science,* vol. 358, no. 6364, pp. 768-771, 2017.

[5] L. Pan *et al.*, "Cu2O photocathodes with band-tail states assisted hole transport for standalone solar water splitting," *Nature communications,* vol. 11, no. 1, p. 318, 2020.

[6] A. Perumal *et al.*, "High-efficiency, solution-processed, multilayer phosphorescent organic light-emitting diodes with a copper thiocyanate hole-injection/hole-transport layer," *Advanced Materials,* vol. 27, no. 1, pp. 93-100, 2015.

[7] S. D. Chavhan, T. H. Ou, M.-R. Jiang, C.-W. Wang, and J.-H. Jou, "Enabling high-efficiency organic light-emitting diode with trifunctional solution-processable copper (I) thiocyanate," *The Journal of Physical Chemistry C,* vol. 122, no. 33, pp. 18836-18840, 2018.

[8] L. J. Xu, J. Y. Wang, X. F. Zhu, X. C. Zeng, and Z. N. Chen, "Phosphorescent Cationic Au4Ag2 Alkynyl Cluster Complexes for Efficient Solution-Processed Organic Light-Emitting Diodes," *Advanced Functional Materials,* vol. 25, no. 20, pp. 3033-3042, 2015.

[9] P. Pattanasattayavong *et al.*, "Hole-transporting transistors and circuits based on the transparent inorganic semiconductor copper (I) thiocyanate (CuSCN) processed from solution at room temperature," *Advanced Materials,* vol. 25, no. 10, pp. 1504-1509, 2013.

[10] S. Baig, A. D. Hendsbee, P. Kumar, S. Ahmed, and Y. Li, "Yttrium-doped CuSCN thin film transistor: synthesis and optoelectronic characterization study," *Journal of Materials Chemistry C,* vol. 7, no. 46, pp. 14543-14554, 2019.

[11] N. Wijeyasinghe *et al.*, "p-Doping of Copper (I) Thiocyanate (CuSCN) Hole-Transport Layers for High-Performance Transistors and Organic Solar Cells," *Advanced Functional Materials,* vol. 28, no. 31, p. 1802055, 2018.

[12] N. Wijeyasinghe *et al.*, "Copper (I) thiocyanate (CuSCN) hole-transport layers processed from aqueous precursor solutions and their application in thin-film transistors and highly efficient organic and organometal halide perovskite solar cells," *Advanced Functional Materials,* vol. 27, no. 35, p. 1701818, 2017.

[13] M. T. Sajjad *et al.*, "CuSCN Nanowires as Electrodes for p-Type Quantum Dot Sensitized Solar Cells: Charge Transfer Dynamics and Alumina Passivation," *The Journal of Physical Chemistry C,* vol. 122, no. 9, pp. 5161-5170, 2018.

[14] S. R. Gottam, C.-T. Tsai, L.-W. Wang, C.-Y. Li, C.-C. Lin, and S.-Y. Chu, "Communication—Pseudohalide β-CuSCN Nanorod-Based Thin Film as a Potential Hydrogen Gas Sensor," *Journal of The Electrochemical Society,* vol. 167, no. 2, p. 027513, 2020.

[15] F. Wang, D. Chen, Z. Hu, L. Qin, X. Sun, and Y. Huang, "In situ decoration of CuSCN nanorod arrays with carbon quantum dots for highly efficient photoelectrochemical performance," *Carbon,* vol. 125, pp. 344-351, 2017.

[16] N. Yaacobi-Gross *et al.*, "High-Efficiency Organic Photovoltaic Cells Based on the Solution-Processable Hole Transporting Interlayer Copper Thiocyanate (CuSCN) as a Replacement for PEDOT: PSS," *Advanced Energy Materials,* vol. 5, no. 3, p. 1401529, 2015.

[17] W. Wu, Z. Jin, Z. Hua, Y. Fu, and J. Qiu, "Growth mechanisms of CuSCN films electrodeposited on ITO in EDTA-chelated copper (II) and KSCN aqueous solution," *Electrochimica acta,* vol. 50, no. 11, pp. 2343-2349, 2005.

[18] D. Ramírez, K. Álvarez, G. Riveros, B. González, and E. A. Dalchiele, "Electrodeposition of CuSCN seed layers and nanowires: A microelectrogravimetric approach," *Electrochimica Acta,* vol. 228, pp. 308-318, 2017.

[19] C. Liu, W. Wu, K. Liu, M. Li, G. Hu, and H. Xu, "Orientation growth and electrical property of CuSCN films associated with the surface states," *CrystEngComm,* vol. 14, no. 20, pp. 6750-6754, 2012.

[20] B. Sankapal, E. Goncalves, A. Ennaoui, and M. C. Lux-Steiner, "Wide band gap p-type windows by CBD and SILAR methods," *Thin Solid Films,* vol. 451, pp. 128-132, 2004.

[21] B. Cheng *et al.*, "PMMA interlayer-modulated memory effects by space charge polarization in resistive switching based on CuSCN-nanopyramids/ZnO-nanorods pn heterojunction," *Scientific Reports,* vol. 5, no. 1, p. 17859, 2015.

[22] L. Sun, K. Ichinose, T. Sekiya, T. Sugiura, and T. Yoshida, "Cathodic electrodeposition of p-CuSCN nanorod and its dye-sensitized photocathodic property," *Physics Procedia,* vol. 14, pp. 12-24, 2011.

[23] X. Gan, W. Zhaohui, K. Liu, X. Du, L. Guo, and H. Liu, "Electrochemical Deposition of CuSCN Nanorod Arrays by Using EDTA as Chelating Agent," *Journal of Nanoscience and Nanotechnology,* vol. 17, no. 1, pp. 538-543, 2017.

[24] T. Iwamoto *et al.*, "Electrochemical self-assembly of nanostructured CuSCN/rhodamine B hybrid thin film and its dye-sensitized photocathodic properties," *The Journal of Physical Chemistry C,* vol. 118, no. 30, pp. 16581-16590, 2014.

[25] H.-P. Lin, X.-J. Lin, and D.-C. Perng, "Electrodeposited CuSCN metal-semiconductor-metal high performance deep-ultraviolet photodetector," *Applied Physics Letters,* vol. 112, no. 2, p. 021107, 2018.

[26] Q. Xi *et al.*, "Highly efficient inverted solar cells based on perovskite grown nanostructures mediated by CuSCN," *Nanoscale,* vol. 9, no. 18, pp. 6136-6144, 2017.

[27] P. Pattanasattayavong, V. Promarak, and T. D. Anthopoulos, "Electronic properties of copper (I) thiocyanate (CuSCN)," *Advanced Electronic Materials,* vol. 3, no. 3, p. 1600378, 2017.

[28] W. Luo *et al.*, "Copper thiocyanate/copper iodide based hole transport composites with balanced properties for efficient polymer light-emitting diodes," *Journal of Materials Chemistry C,* vol. 6, no. 18, pp. 4895-4902, 2018.

[29] F. Shan *et al.*, "High-mobility p-type NiO x thin-film transistors processed at low temperatures with Al 2 O 3 high-k dielectric," *Journal of Materials Chemistry C,* vol. 4, no. 40, pp. 9438-9444, 2016.

[30] D. Shi *et al.*, "Spiro-OMeTAD single crystals: Remarkably enhanced charge-carrier transport via mesoscale ordering," *Science advances,* vol. 2, no. 4, p. e1501491, 2016.

[31] S. M. Hatch, J. Briscoe, and S. Dunn, "A self-powered ZnO-nanorod/CuSCN UV photodetector exhibiting rapid response," *Advanced Materials,* vol. 25, no. 6, pp. 867-871, 2013.

[32] J. A. Switzer, M. G. Shumsky, and E. W. Bohannan, "Electrodeposited ceramic single crystals," *Science,* vol. 284, no. 5412, pp. 293-296, 1999.

[33] N. K. Mahenderkar *et al.*, "Epitaxial lift-off of electrodeposited single-crystal gold foils for flexible electronics," *Science,* vol. 355, no. 6330, pp. 1203-1206, 2017.

[34] A. Banik, J. Z. Tubbesing, B. Luo, X. Zhang, and J. A. Switzer, "Epitaxial Electrodeposition of Optically Transparent Hole-Conducting CuI on n-Si (111)," *Chemistry of Materials,* vol. 33, no. 9, pp. 3220-3227, 2021.

[35] L. Petti *et al.*, "Solution-processed p-type copper (I) thiocyanate (CuSCN) for low-voltage flexible thin-film transistors and integrated inverter circuits," *Applied Physics Letters,* vol. 110, no. 11, p. 113504, 2017.

[36] C. Fernando, I. Kumarawadu, K. Takahashi, A. Kitagawa, and M. Suzuki, "Crystal violet dye-sensitized photocurrent by participation of surface states on p-CuSCN photocathode," *Solar energy materials and solar cells,* vol. 58, no. 4, pp. 337-347, 1999.

[37] X. Li and A. A. Gewirth, "Potential-dependent reorientation of thiocyanate on Au electrodes," *Journal of the American Chemical Society,* vol. 125, no. 38, pp. 11674-11683, 2003.

[38] C. Chappaz-Gillot, R. Salazar, S. Berson, and V. Ivanova, "Insights into CuSCN nanowire electrodeposition on flexible substrates," *Electrochimica Acta,* vol. 110, pp. 375-381, 2013.

[39] D. Smith and V. Saunders, "Preparation and structure refinement of the 2H polytype of β-copper (I) thiocyanate," *Acta Crystallographica Section B: Structural Crystallography and Crystal Chemistry,* vol. 38, no. 3, pp. 907-909, 1982.

[40] D. Smith and V. Saunders, "The structure and polytypism of the β modification of copper (I) thiocyanate," *Acta Crystallographica Section B: Structural Crystallography and Crystal Chemistry,* vol. 37, no. 10, pp. 1807-1812, 1981.

[41] L. Li, J. Liang, L. Qin, D. Chen, and Y. Huang, "In situ growth of a P-type CuSCN/Cu 2 O heterojunction to enhance charge transport and suppress charge recombination," *Journal of Materials Chemistry C,* vol. 7, no. 23, pp. 6872-6878, 2019.

[42] G. Wyatt-Moon, D. G. Georgiadou, J. Semple, and T. D. Anthopoulos, "Deep ultraviolet copper (I) thiocyanate (CuSCN) photodetectors based on coplanar nanogap electrodes fabricated via adhesion lithography," *ACS applied materials & interfaces,* vol. 9, no. 48, pp. 41965-41972, 2017.

[43] B. Luo, A. Banik, E. W. Bohannan, and J. A. Switzer, "Epitaxial Electrodeposition of Cu (111) onto an l-Cysteine Self-Assembled Monolayer on Au (111) and Epitaxial Lift-Off of Single-Crystal-like Cu Foils for Flexible Electronics," *The Journal of Physical Chemistry C,* vol. 124, no. 39, pp. 21426-21434, 2020.

# II. EPITAXIAL ELECTRODEPOSITION OF WIDE BANDGAP CUPROUS BROMIDE ON SILVER VIA A SILVER BROMIDE BUFFER LAYER

*Bin Luo, Xiaoting Zhang, John Z. Tubbesing, Avishek Banik, and Jay A. Switzer**

Department of Chemistry and Graduate Center for Materials Research, Missouri University of Science and Technology, Rolla, MO 65409-1170, USA.

## ABSTRACT

Cuprous halides are an important class of wide bandgap p-type semiconductors used in opto-electronics. Cuprous bromide (CuBr) shows potential for short-wavelength devices due to a large exciton binding energy (108 meV) and near-ultraviolet bandgap (3.1 eV). However, the growth of high-quality epitaxial CuBr films by electrodeposition has remained a challenge. Here, we introduce a low-cost electrochemical procedure for producing epitaxial CuBr(111) on a Ag(111) substrate by a [111]-oriented silver bromide (AgBr) buffer layer. The AgBr buffer layer forms during the electrodeposition of the CuBr. The mismatch between CuBr(111) and AgBr(111) is -1.3%. A plausible mechanism for nucleation and growth of the epitaxial CuBr is proposed. X-ray techniques including high resolution x-ray diffraction and x-ray pole figures are used to determine the epitaxial relationship. CuBr(100) is also produced on a Ag(100) surface by a AgBr(100) buffer layer that is rotated in-plane 45° relative to the Ag(100) surface. This in-plane rotation reduces the lattice mismatch from +39.5% for an unrotated film to -1.4% for a 45° rotated film.

# 1. INTRODUCTION

Wide bandgap transparent p-type semiconductor thin films are crucial for various opto-electronic devices such as perovskite solar cells, transparent p-n junctions, transistors, light emitting diodes and flexible electronics.[1-5] Wide bandgap p-type semiconductors could serve as hole transporting materials (HTMs), transparent conductive materials (TCMs) and blue light emitting diode (LED) materials.[6-8] Highly ordered p-type semiconductors provide a low density of defects and suppressed charge recombination possibilities relative to polycrystalline films.[9] Cuprous halides (CuX, where X = Cl, Br, I) are an important class of p-type semiconductors due to their large bandgap, transparency in the visible range, and good hole conducting properties.[10,11] Among them, CuBr is a nontoxic I-VII semiconductor with a γ-polymorph and zinc blende structure (space group, $F\bar{4}3m$) at room temperature. CuBr is a natural p-type semiconductor because of Cu vacancies. CuBr has a near-ultraviolet bandgap (3.1 eV), relatively high transparency (>80%) in the visible range, and an exceptionally large exciton binding energy (108 meV).[12-13] Therefore, CuBr shows great potential for short-wavelength devices such as light-emitting devices, nonlinear optical devices, and UV photodetectors.[14-18] Ultrathin 2D nonlayered CuBr flakes have been used to build UV photodetectors with high photoresponsivity and fast response.[18] Additionally, CuBr has been applied as an inorganic HTM in organic photovoltaics and transistors.[19-21] Although various methods have been used to produce CuBr films such as RF sputtering, chemical vapor deposition, molecular

beam epitaxy, spin-coating, and electrodeposition, most methods produced polycrystalline or textured CuBr films which lack in-plane order as well as out-of-plane order.[22-26] Therefore, a low-cost epitaxial growth of CuBr thin film is needed. Epitaxial electrodeposition is a soft solution deposition method for obtaining low-cost high quality ordered thin films.[27-30] In this work, we show epitaxial electrodeposition of CuBr from a $CuSO_4$-KBr bath at room temperature. The epitaxial growth of CuBr at the wafer scale is achieved on the surface of Ag(100 nm)/Au(10 nm)/Si substrate by employing a AgBr buffer layer which forms spontaneously during the CuBr electrodeposition. The electrochemistry is investigated to explain the formation of the AgBr buffer layer and the epitaxial deposition process.

## 2. EXPERIMENTAL SECTION

### 2.1. Si WAFER ETCHING PROCESS AND Au, Ag DEPOSITION

n-Si (0.2° miscut toward [11 $\bar{2}$ ], 1-3 Ω cm) was purchased from Virginia Semiconductor Inc. Si wafers were washed following standard RCA1 and RCA2 procedures. An In-Ga eutectic alloy was coated on the backside of the Si to make an ohmic contact. Silver wires and insulating wax were further put onto the backside of the Si. Au deposition on Si was performed by our previous method.[30] Prior to deposition, Si was etched with 5% HF solution to produce an H-terminated surface. Then, a pre-polarization potential of -1.9 V vs. Ag/AgCl was applied to the Si sample and the sample was dipped

into a solution containing 0.1 mM $HAuCl_4$, 1 mM KCl, 1 mM $H_2SO_4$ and 0.1 M $K_2SO_4$. A 10 nm thick Au film was obtained by a 10 minute deposition. Ag deposition on Au/Si was achieved in a commercial cyanide-based KROHN solution.[31] A constant current density of -5 mA/cm$^2$ was applied for 20 s to produce a 100 nm thick Ag layer.

## 2.2. ELECTRODEPOSITION OF CuBr

One-step electrodeposition of epitaxial CuBr was carried out from an aqueous $CuSO_4$-KBr solution bath by a three-electrode system. The counter electrode was a Au wire coil and the reference electrode was saturated Ag/AgCl. The bath solution contained 20 mM $Cu(SO_4)\cdot 5H_2O$ and 40 mM KBr. The Ag/Au/Si was pre-polarized at -0.05 V vs. Ag/AgCl, and electrodeposition was performed with 200 rpm magnetic stirring at room temperature.

## 2.3. ELECTROCHEMICAL ANALYSIS

LSVs were acquired with a 3 mm diameter Au RDE and Ag-coated Au RDE at a rotation rate of 1000 rpm. Ag deposition on Au RDE was achieved in a commercial cyanide-based KROHN solution with a constant current density of -5 mA/cm$^2$ applied for 20 s to produce a 100 nm thick Ag layer. CV curves of Ag conversion to AgBr were performed with a 1 cm x 1 cm Ag/Au/glass electrode without stirring. In all measurements, the scan rate was 10 mV/s and the step size was 1 mV.

## 2.4. XRD AND SEM MEASUREMENTS

XRD was performed with a Philips X'Pert Materials Research diffractometer (XRD) with a CuKα radiation source and a Ni filter. Plan-view SEM was performed with a FEI Helios Nanolab Dualbeam.

# 3. RESULTS AND DISCUSSION

## 3.1. ELECTROCHEMICAL ANALYSIS

In order to find a scalable electrochemical method to deposit uniform epitaxial CuBr films, the electrolyte for the deposition of CuBr was chosen as 20 mM $CuSO_4$ and 40 mM KBr. Then, the electrochemistry was explored by using a rotating disk electrode (RDE) which could control the convection to the electrode surface and measure the limiting current following the Levich equation,[32] as shown in Figure 1.

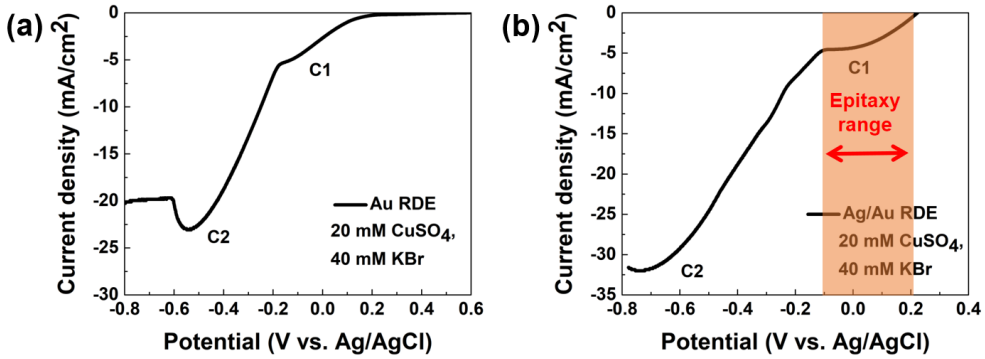


Figure 1. Electrochemical analysis of electrolytes. (a) Linear sweep voltammogram (LSV) of Au rotating disk electrode (RDE) in 20 mM $CuSO_4$, 40 mM KBr with 1000 rpm rotation rate; (b) LSV of Ag/Au RDE in 20 mM $CuSO_4$, 40 mM KBr with 1000 rpm rotation rate. Ag layers were 100 nm thick. The scan rate of both curves was 10 mV/s.

LSVs were first performed on Au RDE because Au is a common inert metal for epitaxial growth, which is shown in Figure 1a. Two cathodic regimes were observed as C1 and C2 as seen earlier.[33] C1 begins at an onset potential +0.2 V and reaches a plateau due to the mass-transfer limit of solution species. C1 is attributed to the reduction of Cu(II) to Cu(I) to form CuBr in the presence of $Br^-$, as given in eqs 1 and 2. C2 manifests itself as a peak which indicates that it is a surface species reduction. C2 is attributed to the further reduction of CuBr to metallic Cu(0), as shown in eq 3.

$$Cu(II) + e^- = Cu^+ \quad (1)$$

$$Cu^+ + Br^- = CuBr \quad (2)$$

$$CuBr + e^- = Cu(0) \quad (3)$$

Although Au serves as a noble inert substrate for some cuprous materials,[6] CuBr could not be grown epitaxially on the Au(111) surface. The CuBr crystals grow without in-plane and out-of-plane order. Since it is well known that halides are strongly adsorbed on the surface of silver, the silver surface is a good candidate for epitaxial growth of CuBr. Figure 1b shows the LSV of Ag(100 nm)/Au RDE in the same electrolyte as 20 mM $CuSO_4$ and 40 mM KBr. In this case, we observed two cathodic regimes which are similar to the Au RDE. The shadowed area shows the potential range (-0.1 V to +0.2 V) of epitaxial deposition of CuBr on Ag. Four samples using varied pre-polarized potentials were examined by XRD analysis, as shown in Figure 2. We found that at -0.05V, CuBr is highly ordered with a [111] orientation with the existence of AgBr(111) (Figure 2a). When the

applied potential is more negative than -0.1V, the formation of AgBr does not occur, and the CuBr that is produced is polycrystalline in nature as confirmd by XRD (Figure 2b,2c). Further negative potentials (≥ -0.2 V) cause the formation of Cu metal (Figure 2d).

It should be noted that epitaxial CuBr could only be achieved with the co-existence of AgBr. This phenomenon reveals that the formation of AgBr is essential for the epitaxial electrodeposition of CuBr. The formation of AgBr is due to the oxidation of Ag metal with adsorbed $Br^-$ anions, as given in eq 4.

$$Ag(0) + Br^- = AgBr + e^- \quad (4)$$

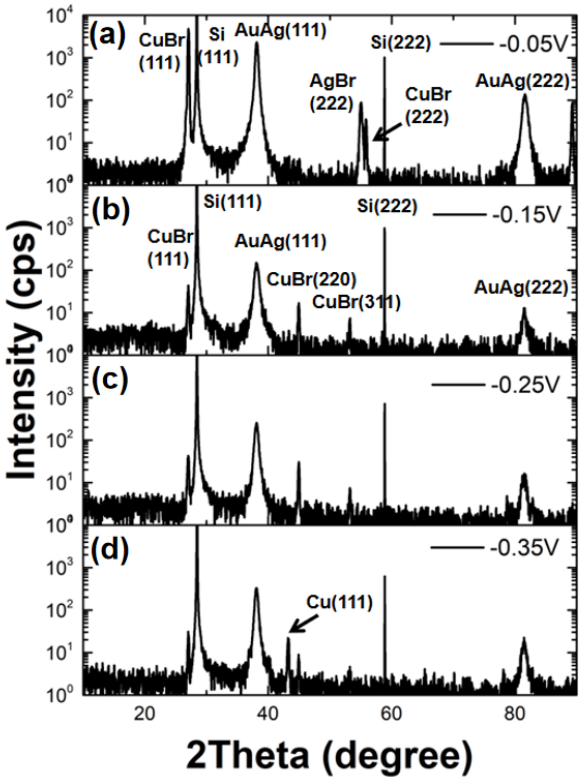


Figure 2. X-ray diffraction analysis of deposited CuBr film on Ag/Au/Si(111) deposited at potentials of (a) -0.05 V, (b) -0.15 V, (c) -0.25 V, (d) -0.35 V to a charge density of 0.12 $C/cm^2$.

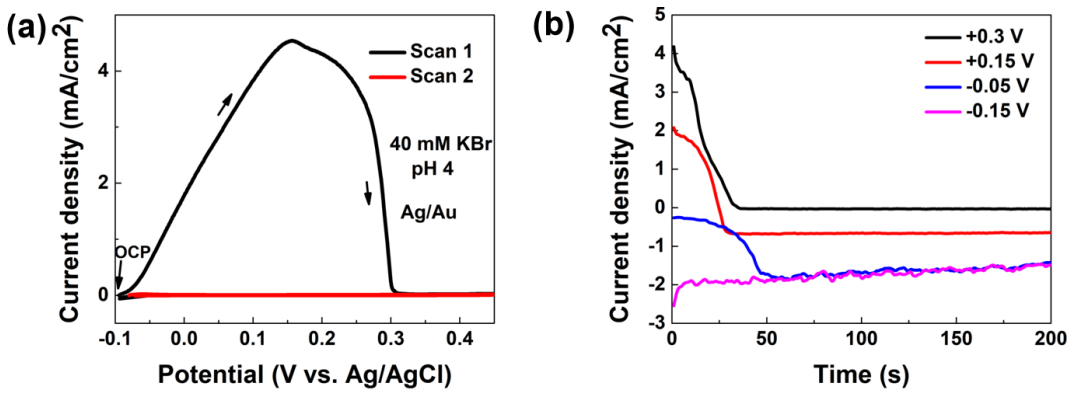


Figure 3. Electrochemical analysis of the formation of AgBr and CuBr deposition. (a) Cyclic voltammogram (CV) of Ag-coated Au electrode in 40 mM KBr solution (pH = 4) without stirring; (b) Current density-time transients for the electrodeposition of epitaxial CuBr at +0.3 V, +0.15 V, -0.05 V and -0.15 V vs. Ag/AgCl in 20 mM $CuSO_4$ and 40 mM KBr with 200 rpm magnetic stirring of the room temperature solution. Positive current densities are anodic.

To gain insight into the epitaxial deposition mechanism of CuBr, the electrochemistry of Ag(0) oxidation to AgBr was further studied by CV on a stationary Ag/Au RDE in 40 mM KBr solution (pH = 4) shown in Figure 3a. When the applied potential is more positive than the OCP at -0.1 V vs Ag/AgCl, Ag(0) oxidation to AgBr occurs in the first scan.[34] This OCP is close the the literature value of -0.15 V vs. Ag/AgCl for the standard reduction potential.[35] The second scan with zero current density confirms the anodic peak is due to oxidation of surface species. This -0.1 V potential limit agrees with our experimental potential range for deposition of epitaxial CuBr. These data reveal the mechanism of epitaxial CuBr on Ag substrate to be via a AgBr buffer layer. Even though the CuBr is deposited by cathodic deposition, the anodic oxidation of Ag to AgBr occurs before the CuBr is deposited.

Current density-time transients at a series of applied potentials were used to gain insight into the anodic formation of AgBr and the cathodic electrodeposition of CuBr. Transients obtained at potentials of +0.3, +0.15, -0.05, and -0.15 V vs. Ag/AgCl were obtained on a Ag-coated Au electrode in a magnetically stirred solution of 20 mM $CuSO_4$ and 40 mM KBr at room temperature. The curve obtained at +0.3 V shows only anodic currents which decay to zero at approximately 75 s. This is consistent with the fact that Cu(II) is not reduced at this potential (see, Fig. 1), and the current is due to the complete oxidation of Ag to AgBr. At +0.15 V the transient begins as an anodic current and switches to cathodic deposition of CuBr with a current density of about -0.5 $mA/cm^2$. The potential that is used to deposit our epitaxial films in this study was -0.05 V. When this potential is applied to the Ag-coated Au electrode, the current is cathodic at all times but it shows an increase in the cathodic current until about 50 s. This is consistent with concurrent oxidation and reduction occurring during the first 50 s. This increase in cathodic current density is not observed when -0.15 V is applied because Ag is not oxidized at this potential. Note that CuBr films deposited at -0.15 V are not epitaxial. The curves obtained at -0.05 and -0.15 V overlap at times greater than 50 s. The cathodic current density for both of these applied potentials slowly decreases at longer times, consistent with the development of a depletion region in the p-type CuBr which tends to block the reduction reaction. To verify that AgBr does serve as the template at -0.05 V deposition, we used 70 wt% $HNO_3$ to completely etch the upper CuBr layer to reveal the buffer AgBr film underneath the CuBr.

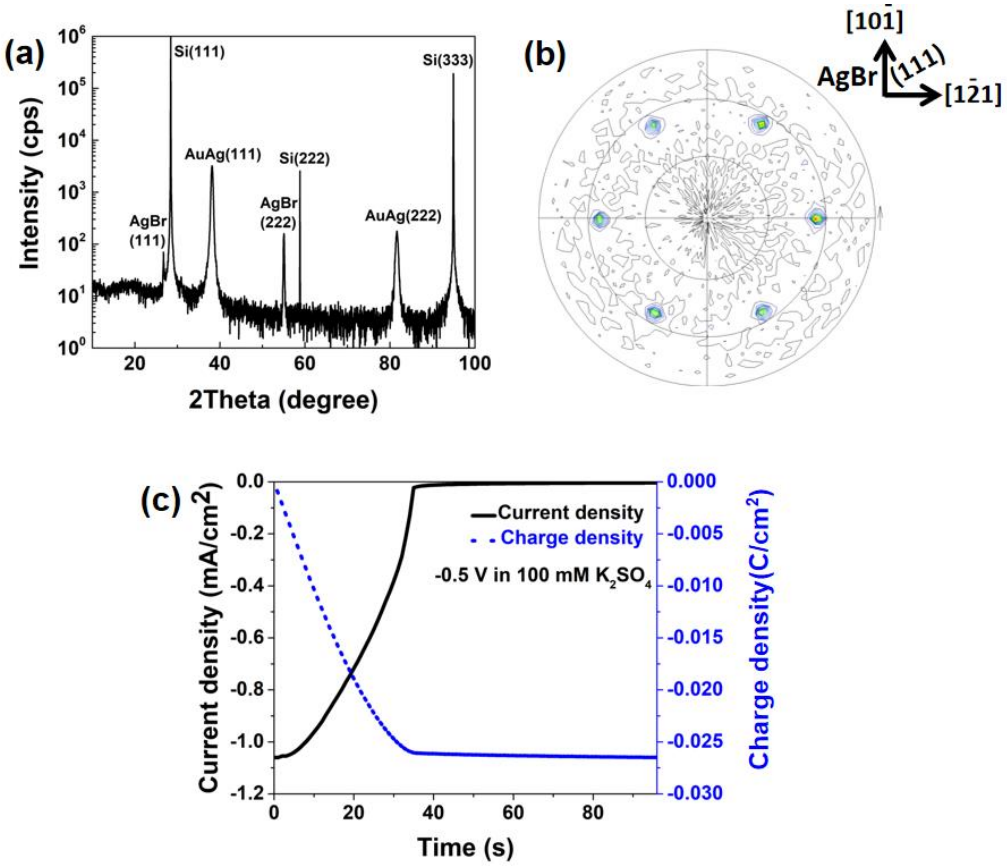


Figure 4. Characterization of epitaxial AgBr(111) buffer layer after 70 wt% $HNO_3$ etching of CuBr film. (a) XRD pattern of AgBr(111) buffer layer; (b) (200) pole figure of AgBr(111) buffer layer; (c) Thickness of the AgBr buffer layer determined to be 80 nm according to the charge density of electrochemical reduction of AgBr to Ag at -0.5 V in 100 mM $K_2SO_4$.

In the XRD pattern shown in Figure 4a, The AgBr buffer layer shows the {111} family of peaks (JCPDS no. 79-0149) confirming the out-of-plane order of the AgBr. In-plane orientation of buffer layer was also tested in Figure 4b. The (200) pole of AgBr(111) shows six intense peaks at a tilt angle of 54.74° showing that AgBr(111) buffer layer is indeed epitaxial. The thickness of AgBr buffer layer was determined to be 80 nm by the charge density of electrochemical reduction of AgBr to Ag at -0.5 V in 100 mM $K_2SO_4$

(Figure 4c). The 80 nm thickness of AgBr corresponds to 29 nm of converted Ag. Considering that the initial thickness of Ag is 100 nm, 29 nm of Ag is consumed to form the 80 nm thick AgBr buffer layer at a -0.05 V deposition potential.

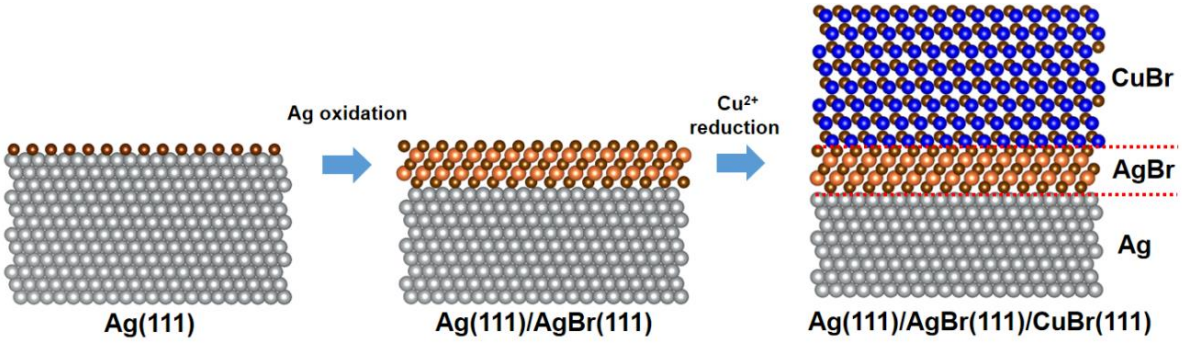


Figure 5. Schematic showing growth of epitaxial CuBr(111) on Ag(111) substrate via a AgBr(111) buffer layer.

The plauasible mechanism is shown in Figure 5. Firstly, $Br^-$ ions are strongly adsorbed on the Ag surface. In the Ag(111) case, a $(\sqrt{3} \times \sqrt{3})R30°$ surface structure of the adsorbed halides is mostly reported.[36-38] Next, a suitable potential (-0.1 V to +0.2 V) forces the Ag atoms in the topmost layer to be oxidized to Ag(I) ions which react with $Br^-$ to form AgBr(111) layers [eq. 4]. Once the AgBr is formed, CuBr starts to nucleate on the surface of AgBr and begins the growth of epitaxial CuBr layers. The epitaxial nucleation of CuBr on AgBr is explained by the low mismatch between the CuBr and AgBr lattices. The lattice parameters of CuBr and AgBr are close to each other and Br atoms on the AgBr lattice surface provide well-controlled nucleation sites for epitaxial CuBr.

### 3.2. X-RAY CHARACTERIZATIONS OF EPITAXIAL CuBr(111) FILM

The out-of-plane and in-plane orientations of CuBr(111) were investigated by X-ray analysis including XRD 2θ scans and X-ray pole figures. A two-inch diameter wafer-scale epitaxial CuBr(111) film is shown in Figure 6a. Figure 6b shows the XRD pattern of the CuBr(111)/AgBr(111)/Ag(111)/Au(111)/Si(111). CuBr exhibits strong and sharp {111} family of peaks (JCPDS no. 06-0292) confirming a high out-of-plane order.

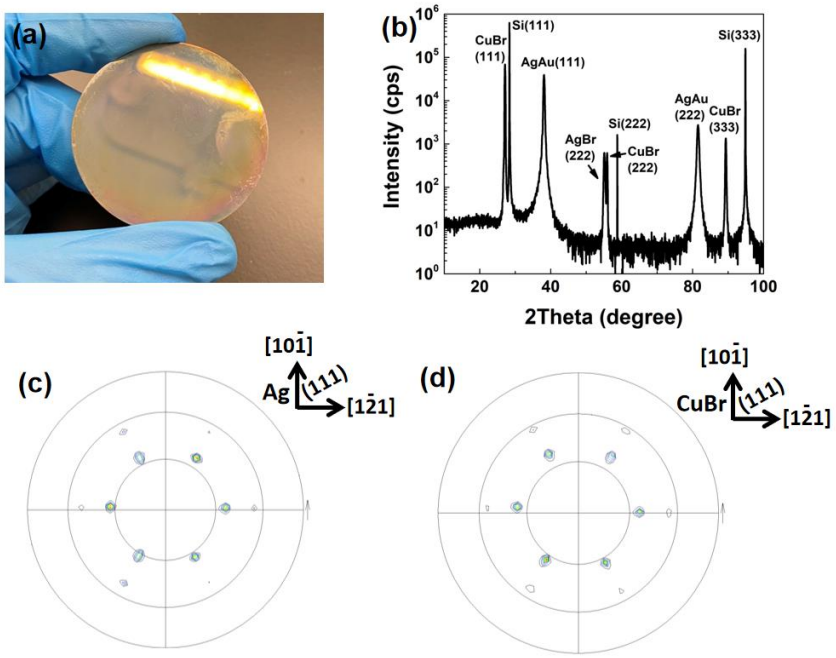


Figure 6. X-ray diffraction analysis of in-plane and out-of-plane orientation of epitaxial CuBr(111) film. (a) 2 inch diameter wafer scale epitaxial CuBr(111) on Ag(111)/Au(111)/Si(111); (b) XRD pattern of CuBr(111)/AgBr(111)/Ag(111)/Au(111)/Si(111); (c) (220) pole of Ag(111); (d) (220) pole of CuBr(111).

A Ag(220) pole (Figure 6c) shows six intense peaks separated by 60° at a tilt angle of 35.5° corresponding to the angle between (111) and (220) planes. Six spots occur

because the Au deposits with in-plane rotational twins relative to Si(111).[30] Six less intense spots at a tilt angle of 54.74° correspond to (400) pole of CuBr(111) due to close 2θ position of Ag(220) pole (2θ = 64.6°) and CuBr(400) pole (2θ = 65.7°). The CuBr(220) pole (Figure 6d) shows similar six intense peaks at a tilt angle of 35.5°, proving that CuBr(111) is epitaxial. The six less intense spots at a tilt angle of 54.74° belong to the (200) pole of Ag(111) due to the close 2θ position of CuBr(220) pole (2θ = 45.1°) and Ag(200) pole (2θ = 44.4°). It should be noted that (200) pole figure of AgBr shown before has the same azimuthal angle as CuBr and Ag. Therefore, the epitaxial relationship determined from these pole figures is CuBr(111)[10$\bar{1}$]//AgBr(111)[10$\bar{1}$]//Ag(111)[10$\bar{1}$]. The CuBr is indeed epitaxial on the buffer layer of AgBr.

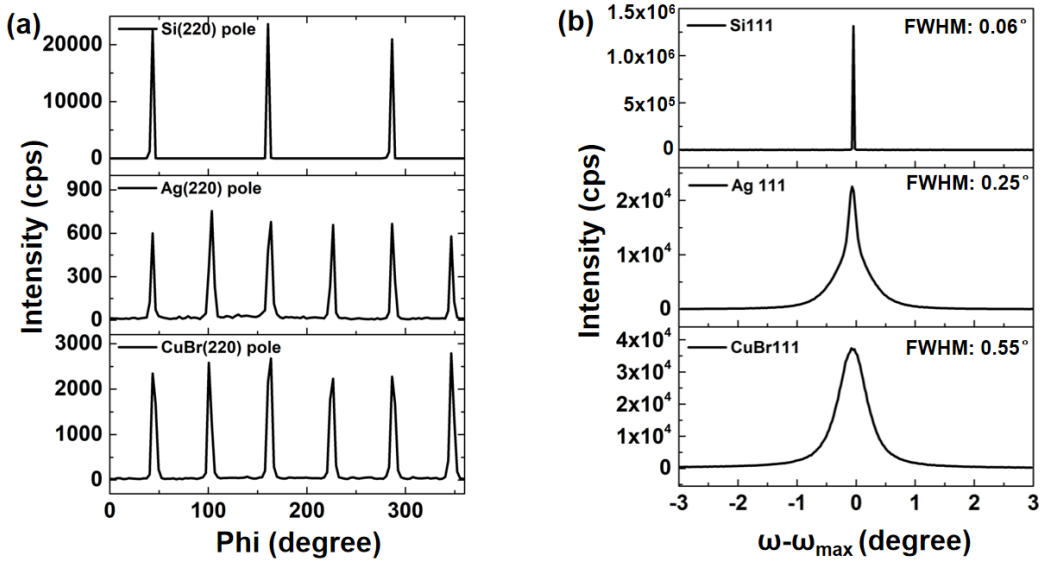


Figure 7. Epitaxial perfection and relationship of epitaxial CuBr(111) film. (a) Azimuthal scans of Si(111), Ag(111) and CuBr(111) at χ = 35.5°; (b) Rocking curves of Si(111), Ag(111) and CuBr(111).

Azimuthal scans were performed for the (220) poles of Si(111), Ag(111) and CuBr(111) at a tilt angle of 35.5° (Figure 7a) by rotating from 0 to 360° azimuthally, which agrees with our obtained epitaxial relationship. Rocking curves were performed by tilting the sample to measure the epitaxial perfection: the sharper the peak, the lower the mosaic spread and better perfection. The FWHMs (full width at half maximum) were recorded as 0.55° for CuBr(111), 0.25° for Ag(111) and 0.06° for Si(111) in Figure 7b. These results of Ag and CuBr are comparable to the best epitaxial films by electrodeposition techniques.[30] The broadening of the peaks is due to mosaic spread during the epitaxial growth.

Beyond X-ray analysis, epitaxial films usually exhibit uniform ordered morphological features which can be examined by electron microscopy. SEM was used to determine the morphology of epitaxial CuBr(111) films. Initial ordered triangular crystals with an average size of 400 nm are formed at -0.05 V with a charge density of 0.02 C/cm$^2$ (Figure 8a). Further growth of crystals leads to uniform epitaxial CuBr films (Figure 8b) at -0.05 V with a charge density of 0.12 C/cm$^2$. By comparing these images with current density-time curve in Figure 3b, we find that the initial crystals image corresponds to deposition times of ~ 30 s in the starting stage, while the uniform films image corresponds to ~ 110 s in the later stage of deposition.

To understand the epitaxial electrodeposition, it is necessary to look at the lattice mismatch between the epitaxial layer and the substrate. Based on lattice constant of CuBr (a = 0.5684 nm), AgBr (a = 0.5774 nm), Ag (a = 0.4085 nm), a mismatch of CuBr/AgBr (-

1.3%) is calculated which is much less than that of CuBr/Ag (+39%). This matched lattice of AgBr is favorable for epitaxial growth of CuBr with less interfacial strains. This relatively low mismatch gives a quantitative explanation as to why the formation of the AgBr(111) buffer layer is essential for epitaxial CuBr.

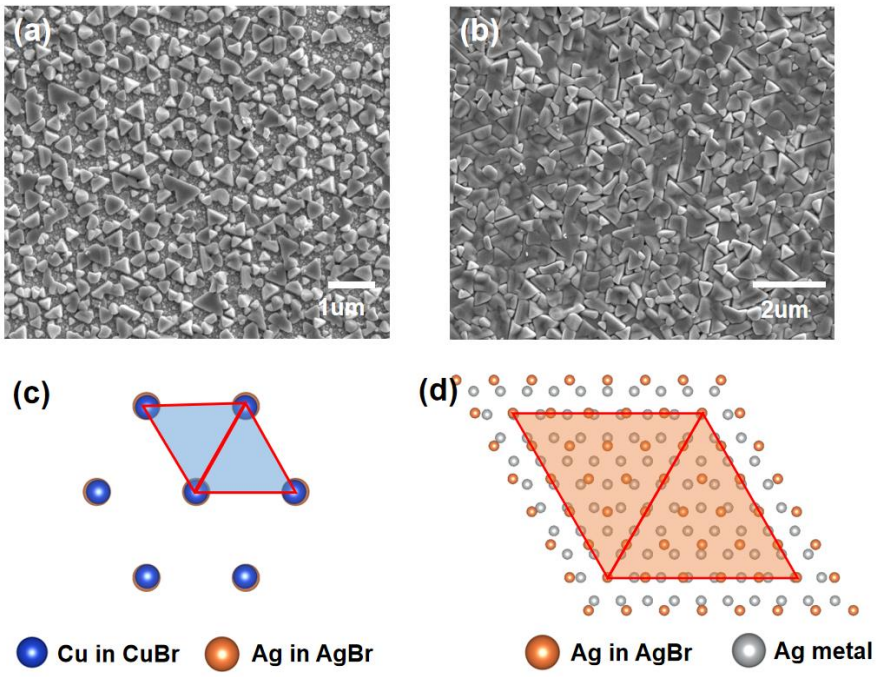


Figure 8. Morphological features and interface models of epitaxial growth of CuBr(111). (a) SEM image of initial CuBr crystals deposited at -0.05V with charge density of 0.02 C/cm$^2$; (b) Uniform CuBr film deposited at -0.05 V with charge density of 0.12 C/cm$^2$; (c) Interface model of Cu (blue) atoms of CuBr(111) with Ag (orange) atoms of AgBr(111) with a mismatch of -1.3%; (d) Interface model of Ag (orange) atoms of AgBr(111) with Ag (gray) atoms of Ag metal. A coincidence site lattice (CSL) is formed by 6 Ag atoms in AgBr with 8 Ag atoms in Ag metal with a CSL mismatch of +0.94%.

An interface model of CuBr(111) on AgBr(111) has been prepared as shown in Figure 8c. Cu (blue) atoms of CuBr(111) align with Ag (orange) atoms of AgBr(111) in a

mismatch of -1.3%. Meanwhile, an interface model of the buffer layer AgBr(111) on Ag(111) is shown in Figure 8d. A coincidence site lattice (CSL) is used to plausibly explain the epitaxial AgBr(111) on Ag(111). 6 Ag atoms in AgBr with 8 Ag atoms in Ag metal form a CSL with a CSL mismatch of +0.94%.

### 3.3. EPITAXIAL CuBr FILM WITH A [100] ORIENTATION

An epitaxial CuBr film with a [100] orientation has also been achieved in this work. CuBr(100) was deposited in one-step at -0.05 V on Ag(100)/Au(100)/Si(100) in a solution of 20 mM $CuSO_4$ and 40 mM KBr at room temperature.

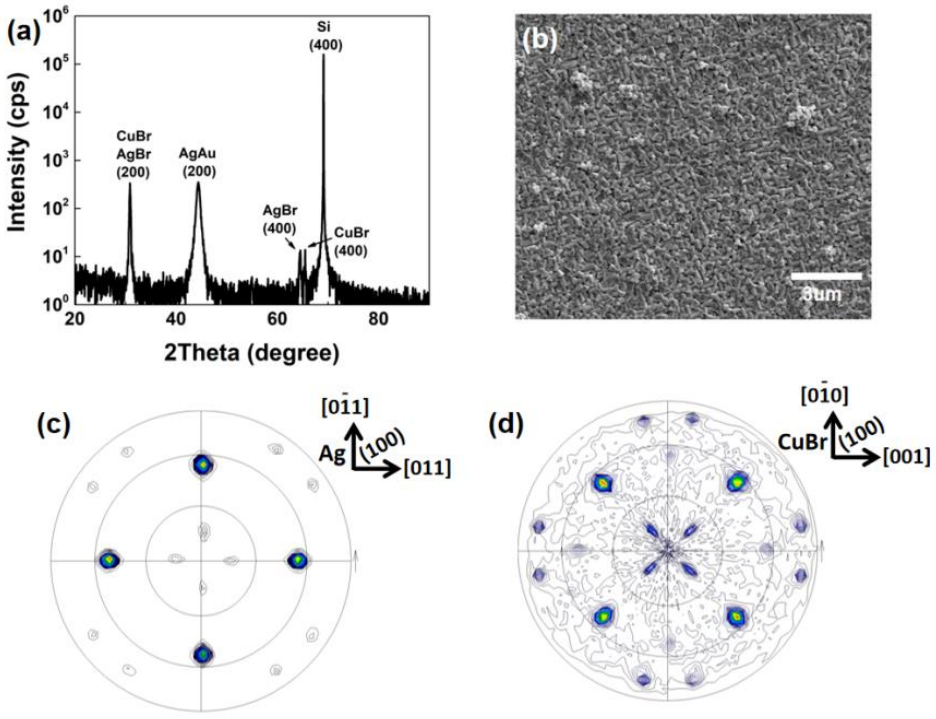


Figure 9. In-plane and out-of-plane orientation of epitaxial CuBr(100) film on Ag(100). (a) XRD of CuBr(100)/AgBr(100)/Ag(100)/Au(100)/Si(100); (b) Plan-view SEM image of epitaxial CuBr(100); (c) (111) pole of Ag(100); (d) (111) pole of CuBr(100).

Figure 9a shows the XRD pattern of CuBr(100)/AgBr(100)/Ag(100) /Au(100)/Si(100). In addition to the substrate peaks, the CuBr {100} family of peaks and AgBr {100} family of peaks were observed, confirming the out-of-plane order of CuBr and the buffer AgBr layer. Figure 9b determines the morphology of the CuBr(100) film to be square by SEM. Figure 9c shows the (111) pole of Ag(100) with four intense spots separated by 90° at a tilt angle of 54.74°. These four spots correspond to the four-fold symmetry of {100} planes. Beside the four major spots, four less intense spots occur at $\chi$ = 15° and eight spots occur at $\chi$ = 77°. This is caused by a small amount of $(\bar{1}22)$ orientation twinning along the {111} slip planes.[39] The (111) pole of CuBr(100) in Figure 9d has the same four intense spots as the Ag(100) substrate separated by 90° at a tilt angle of 54.74° which confirms the CuBr epitaxy.

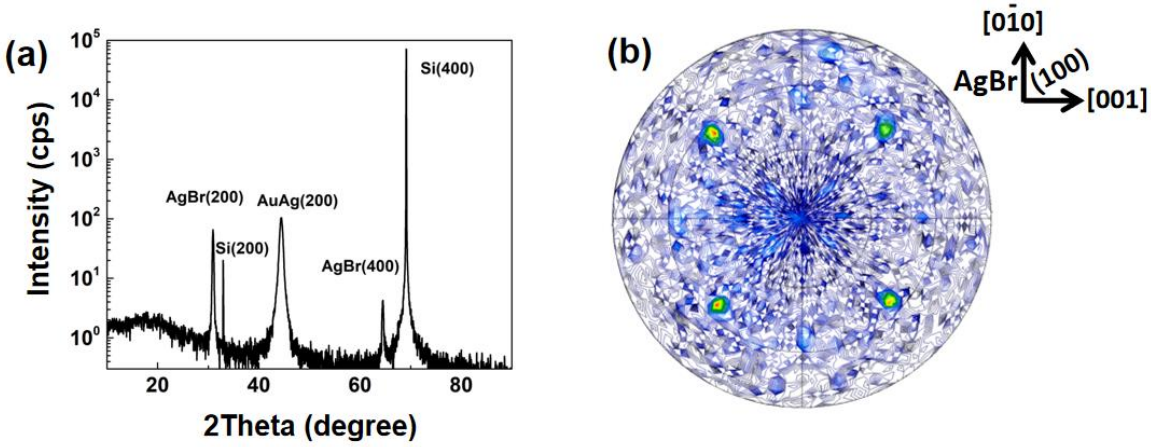


Figure 10. Epitaxial AgBr(100) buffer layer after 70 wt% $HNO_3$ etching of CuBr film. (a) XRD pattern of AgBr(100) buffer layer; (b) (111) pole figure of AgBr(100) buffer layer.

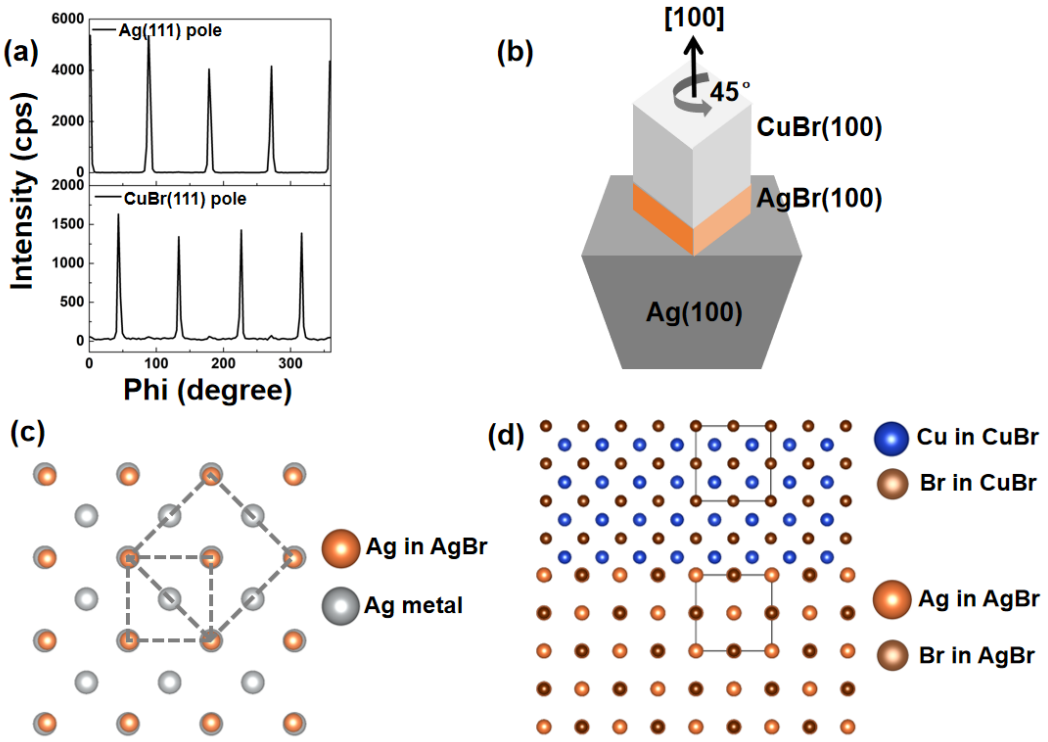


Figure 11. Azimuthal scans and interface models of CuBr(100). (a) Azimuthal scans of Ag(100) and CuBr(100) at $\chi = 54.74°$; (b) Graphical depiction showing the in-plane rotation; (c) Plan-view interface model of Ag atoms in AgBr(100) (orange) with Ag(100) metal (grey) with in-plane 45° rotation with a mismatch of -1.38%; (d) Cross-sectional interface model of CuBr(100) with AgBr(100) with a mismatch of -1.30%.

Interestingly, CuBr(100) was found to be rotated in-plane 45° in the x-ray pole figures compared to the Ag(100). To determine whether this rotation happens in the interface of CuBr/AgBr or AgBr/Ag, the orientation of buffer layer AgBr(100) was tested after removing the CuBr layer (XRD in Figure 10a). The (111) pole of AgBr(100) (Figure 10b) also exhibits four intense spots with 45° in-plane rotation compared to Ag(100). The result means that rotation occurs during the formation of the buffer layer AgBr(100) on Ag(100). This in-plane relationship also provides direct evidence that the AgBr controls

the orientation of CuBr. This 45° rotation was further confirmed by the azimuthal scans (Figure 11a) of the (111) reflection for Ag and CuBr, tilted to $\chi$ = 54.74°. A graphical depiction of CuBr(100)/AgBr(100)/Ag(100) is shown in Figure 11b. Our proposed epitaxial growth is as follows: $Br^-$ halide ions are adsorbed on Ag(100) surface with a c(2 x 2) structure which leads to epitaxial AgBr(100) layers with 45° in-plane rotation. This is consistent with the reported literature.[40] Epitaxial CuBr(100) is further deposited by following the closely matched lattice of AgBr(100). Therefore, the epitaxial relationship is given as CuBr(100)[001]//AgBr(100)[001]//Ag(100)[011]. This in-plane rotation can effectively reduce the mismatch between AgBr(100) and Ag(100). As shown in Figure 11c, The mismatch between a 45° rotated lattice of AgBr(100) and Ag(100) is -1.4%, whereas for an unrotated lattice the mismatch is +39.5%. A cross-sectional view interface model of CuBr(100) on AgBr(100) is shown in Figure 11d. Although the space groups of CuBr ($F\bar{4}3m$) and AgBr ($Fm\bar{3}m$) are different, the unit cells of the two lattices are closely matched with a mismatch of -1.3%.

## 4. CONCLUSIONS

We provide an electrochemical synthetic route for depositing an epitaxial wide bandgap p-type semiconductor CuBr on ordered Ag substrates. Formation of a AgBr buffer layer is essential for the deposition of epitaxial CuBr. Epitaxial films of both CuBr(111) and CuBr(100) are deposited. The CuBr(100) and AgBr(100) buffer layer show an in-plane

rotation of 45° compared to the Ag(100) substrate. This work also opens an interesting method to obtain epitaxial AgBr films by oxidation of epitaxial Ag films. This method may apply to other silver halide and pseudohalide semiconductors such as AgI and AgSCN. Meanwhile, electrochemical production of epitaxial CuBr/AgBr systems could be a promising way to fabricate epitaxial transparent p-n junctions for light-emitting diodes and photodetectors.

## ACKNOWLEDGMENTS

This material is based on work supported by the U.S. Department of Energy, Office of Basic Energy Sciences, Division of Materials Sciences and Engineering, under grant No. DE-FG02-08ER46518.

## REFERENCES

[1] N. Arora *et al.*, "Perovskite solar cells with CuSCN hole extraction layers yield stabilized efficiencies greater than 20%," *Science,* vol. 358, no. 6364, pp. 768-771, 2017.

[2] J. Garnier, R. Parize, E. Appert, O. Chaix-Pluchery, A. Kaminski-Cachopo, and V. Consonni, "Physical properties of annealed ZnO nanowire/CuSCN heterojunctions for self-powered UV photodetectors," *ACS Applied Materials & Interfaces,* vol. 7, no. 10, pp. 5820-5829, 2015.

[3] N. Wijeyasinghe *et al.*, "p-Doping of Copper (I) Thiocyanate (CuSCN) Hole-Transport Layers for High-Performance Transistors and Organic Solar Cells," *Advanced Functional Materials,* vol. 28, no. 31, p. 1802055, 2018.

[4] T. Matsushima *et al.*, "High performance from extraordinarily thick organic light-emitting diodes," *Nature,* vol. 572, no. 7770, pp. 502-506, 2019.

[5] Y. Ji *et al.*, "Ultraflexible and high-performance multilayer transparent electrode based on ZnO/Ag/CuSCN," *ACS applied materials & interfaces,* vol. 10, no. 11, pp. 9571-9578, 2018.

[6] B. Luo, A. Banik, E. W. Bohannan, and J. A. Switzer, "Epitaxial Electrodeposition of Hole Transport CuSCN Nanorods on Au (111) at the Wafer Scale and Lift-off to Produce Flexible and Transparent Foils," *Chemistry of Materials,* vol. 34, no. 3, pp. 970-978, 2022.

[7] G. Hautier, A. Miglio, G. Ceder, G.-M. Rignanese, and X. Gonze, "Identification and design principles of low hole effective mass p-type transparent conducting oxides," *Nature communications,* vol. 4, no. 1, p. 2292, 2013.

[8] S.-D. Baek, D.-K. Kwon, Y. C. Kim, and J.-M. Myoung, "Violet light-emitting diodes based on p-CuI thin film/n-MgZnO quantum dot heterojunction," *ACS applied materials & interfaces,* vol. 12, no. 5, pp. 6037-6047, 2020.

[9] D. Shi *et al.*, "Spiro-OMeTAD single crystals: Remarkably enhanced charge-carrier transport via mesoscale ordering," *Science advances,* vol. 2, no. 4, p. e1501491, 2016.

[10] P. Yuan *et al.*, "Ether-Soluble $Cu_{53}$ Nanoclusters as an Effective Precursor of High-Quality CuI Films for Optoelectronic Applications," *Angewandte Chemie International Edition,* vol. 58, no. 3, pp. 835-839, 2019.

[11] D. Ahn and S.-H. Park, "Cuprous halides semiconductors as a new means for highly efficient light-emitting diodes," *Scientific Reports,* vol. 6, no. 1, pp. 1-9, 2016.

[12] R. K. Vijayaraghavan *et al.*, "Influence of Oxygen Plasma on the Growth, Structure, Morphology, and Electro-Optical Properties of p-Type Transparent Conducting CuBr Thin Films," *The Journal of Physical Chemistry C,* vol. 118, no. 40, pp. 23226-23232, 2014.

[13] K. Rajani, S. Daniels, M. Rahman, A. Cowley, and P. J. McNally, "Deposition of earth-abundant p-type CuBr films with high hole conductivity and realization of p-CuBr/n-Si heterojunction solar cell," *Materials Letters,* vol. 111, pp. 63-66, 2013.

[14] F. O. Lucas, A. Cowley, S. Daniels, and P. McNally, "CuBr blue light emitting electroluminescent thin film devices," *physica status solidi (c),* vol. 8, no. 9, pp. 2919-2922, 2011.

[15] R. K. Vijayaraghavan, D. Chandran, R. K. Vijayaraghavan, A. P. McCoy, S. Daniels, and P. J. McNally, "Highly enhanced UV responsive conductivity and blue emission in transparent CuBr films: implication for emitter and dosimeter applications," *Journal of Materials Chemistry C,* vol. 5, no. 39, pp. 10270-10279, 2017.

[16] R. C. Miller, W. Nordland, S. Abrahams, J. Bernstein, and C. Schwab, "Nonlinear optical properties of the cuprous halides," *Journal of Applied Physics,* vol. 44, no. 8, pp. 3700-3702, 1973.

[17] S. Kondo and T. Saito, "CuBr films on KBr exhibiting $10^2$ or $10^3$ times higher efficiency of free-exciton luminescence than those on usual substrates such as $Al_2O_3$," *Applied physics letters,* vol. 90, no. 20, p. 201915, 2007.

[18] C. Gong *et al.*, "Self-confined growth of ultrathin 2D nonlayered wide-bandgap semiconductor CuBr flakes," *Advanced Materials,* vol. 31, no. 36, p. 1903580, 2019.

[19] R. Bhargav *et al.*, "Copper bromide as an efficient solution-processable hole transport layer for organic solar cells: effect of solvents," *ACS omega,* vol. 4, no. 3, pp. 6028-6034, 2019.

[20] T.-M. Kim, H.-S. Shim, M.-S. Choi, H. J. Kim, and J.-J. Kim, "Multilayer epitaxial growth of lead phthalocyanine and $C_{70}$ using CuBr as a templating layer for enhancing the efficiency of organic photovoltaic cells," *ACS applied materials & interfaces,* vol. 6, no. 6, pp. 4286-4291, 2014.

[21] H. Zhu, A. Liu, and Y.-Y. Noh, "Transparent inorganic copper bromide (CuBr) p-channel transistors synthesized from solution at room temperature," *IEEE Electron Device Letters,* vol. 40, no. 5, pp. 769-772, 2019.

[22] O. Schäf, P. Lauque, J.-L. Seguin, M. Eyraud, and P. Knauth, "Microstructure and ammonia gas sensitivity of sputtered films of the mixed ionic–electronic conductor CuBr," *Thin Solid Films,* vol. 389, no. 1-2, pp. 5-7, 2001.

[23] C. M. Chang, L. M. Davis, E. K. Spear, and R. G. Gordon, "Chemical vapor deposition of transparent, p-type cuprous bromide thin films," *Chemistry of Materials,* vol. 33, no. 4, pp. 1426-1434, 2021.

[24] A. Yanase and Y. Segawa, "Two different in-plane orientations in the growths of cuprous halides on MgO (001)," *Surface science,* vol. 329, no. 3, pp. 219-226, 1995.

[25] T. Harada, S. Tao, T. Imamura, K. Moriya, N. Saito, and K. Tanaka, "Preparation of transparent CuI–CuBr alloy thin films by solution processing," *Japanese Journal of Applied Physics,* vol. 57, no. 2S2, p. 02CB05, 2017.

[26] H. Li, R. Liu, H. Kang, Y. Zheng, and Z. Xu, "Growth and characterization of highly oriented CuBr thin films through room temperature electrochemical route," *Electrochimica acta,* vol. 54, no. 2, pp. 242-246, 2008.

[27] J. A. Koza, J. C. Hill, A. C. Demster, and J. A. Switzer, "Epitaxial electrodeposition of methylammonium lead iodide perovskites," *Chemistry of Materials,* vol. 28, no. 1, pp. 399-405, 2016.

[28] A. Banik, E. W. Bohannan, and J. A. Switzer, "Epitaxial electrodeposition of $bii_3$ and topotactic conversion to highly ordered solar light-absorbing perovskite $(CH_3NH_3)_3Bi_2I_9$," *Chemistry of Materials,* vol. 32, no. 19, pp. 8367-8372, 2020.

[29] B. Luo, A. Banik, E. W. Bohannan, and J. A. Switzer, "Epitaxial Electrodeposition of Cu (111) onto an l-Cysteine Self-Assembled Monolayer on Au (111) and Epitaxial Lift-Off of Single-Crystal-like Cu Foils for Flexible Electronics," *The Journal of Physical Chemistry C,* vol. 124, no. 39, pp. 21426-21434, 2020.

[30] N. K. Mahenderkar *et al.*, "Epitaxial lift-off of electrodeposited single-crystal gold foils for flexible electronics," *Science,* vol. 355, no. 6330, pp. 1203-1206, 2017.

[31] M. V. Kelso, J. Z. Tubbesing, Q. Chen, and J. A. Switzer, "Epitaxial electrodeposition of chiral metal surfaces on silicon (643)," *Journal of the American Chemical Society,* vol. 140, no. 46, pp. 15812-15819, 2018.

[32] A. J. Bard, L. R. Faulkner, and H. S. White, *Electrochemical methods: fundamentals and applications*. John Wiley & Sons, 2022.

[33] A. Banik, J. Z. Tubbesing, B. Luo, X. Zhang, and J. A. Switzer, "Epitaxial Electrodeposition of Optically Transparent Hole-Conducting CuI on n-Si (111)," *Chemistry of Materials,* vol. 33, no. 9, pp. 3220-3227, 2021.

[34] B. Jović, V. Jović, and D. Dražić, "Kinetics of chloride ion adsorption and the mechanism of AgCl layer formation on the (111),(100) and (110) faces of silver," *Journal of Electroanalytical Chemistry,* vol. 399, no. 1-2, pp. 197-206, 1995.

[35] D. Lide, "CRC handbook of physics and chemistry 74th ed., publ," ed: CRC press, 1993.

[36] G. N. Salaita, F. Lu, L. Laguren-Davidson, and A. T. Hubbard, "Structure and composition of the Ag (111) surface as a function of electrode potential in aqueous halide solutions," *Journal of electroanalytical chemistry and interfacial electrochemistry,* vol. 229, no. 1-2, pp. 1-17, 1987.

[37] A. G. Shard and V. R. Dhanak, "Chlorine adsorption on silver (111) at low temperatures," *The Journal of Physical Chemistry B,* vol. 104, no. 12, pp. 2743-2748, 2000.

[38] T. Yamada, K. Ogaki, S. Okubo, and K. Itaya, "Continuous variation of iodine adlattices on Ag (111) electrodes: in situ STM and ex situ LEED studies," *Surface science,* vol. 369, no. 1-3, pp. 321-335, 1996.

[39] C. M. Hull and J. A. Switzer, "Electrodeposited epitaxial Cu (100) on Si (100) and lift-off of single crystal-like Cu (100) foils," *ACS applied materials & interfaces,* vol. 10, no. 44, pp. 38596-38602, 2018.

[40] T. Shimooka, J. Inukai, and K. Itaya, "Adlayer structures of cl and br and growth of bulk AgBr layers on Ag (100) electrodes," *Journal of The Electrochemical Society,* vol. 149, no. 2, p. E19, 2001.

# III. EPITAXIAL ELECTRODEPOSITION OF Cu(111) ONTO AN L-CYSTEINE SELF-ASSEMBLED MONOLAYER ON Au(111) AND EPITAXIAL LIFT-OFF OF SINGLE-CRYSTAL-LIKE Cu FOILS FOR FLEXIBLE ELECTRONICS

*Bin Luo, Avishek Banik, Eric W. Bohannan, and Jay A. Switzer**

Department of Chemistry and Graduate Center for Materials Research, Missouri University of Science and Technology, Rolla, MO 65409-1170, USA.

## ABSTRACT

Functional self-assembled monolayers (SAMs) of thiols on single crystal metals provide two-dimensional soft templates for highly-ordered growth of crystalline materials. An epitaxial Cu(111) film is electrodeposited on a self-assembled monolayer of the amino acid L-cysteine on Au(111). Epitaxy is confirmed, with the Cu(111) following the Au(111) in-plane and out-of-plane orientation with a small amount of twinned [511] orientation, which is shown by X-ray analysis. The mismatch between Cu(111) and the Au(111) substrate is -11.37%. This mismatch is lowered to -0.29% by forming a coincident site lattice in which 9 unit meshes of Cu coincide with 8 unit meshes of Au. Defect-mediated and coordination-controlled electrodeposition mechanisms are illustrated as two possible deposition mechanisms. The carboxylic (-COOH) and amine ($-NH_2$) functional groups of the L-cysteine molecule are shown to be crucial for epitaxy of Cu, because a 1-butanethiol SAM on Au(111) which has no functional groups yields a textured film with no in-plane order. The ($\sqrt{3}$ x$\sqrt{3}$)R30° surface structure of L-cysteine SAM and c(4 x 2) surface structure

of 1-butanethiol SAM on Au(111) are discussed. A 3D model of the Cu lattice on the L-cysteine SAM on Au(111) is proposed. Possible coordination to the Cu is shown, which facilitates the epitaxial nucleation and 2D growth of Cu. The Cu(111) films have potential as a substrate for catalysts for $CO_2$ reduction, photovoltaic devices, spintronic devices and high temperature superconductors. Direct epitaxial lift-off of the Cu film without etching gives a single-crystal-like Cu(111) foil. The Cu(111) foil exhibits a low resistivity of $3.75 \times 10^{-8}$ Ω.m and good bending stability, showing only a 12% increase in resistance after $10^4$ bending cycles. Cu(111) foils can be utilized as inexpensive, highly-ordered conductive substrates for flexible electronics such as wearable solar cells, sensors and flexible displays. Here, we show an example by electrodepositing epitaxial cuprous oxide on a Cu(111) foil.

KEYWORDS: L-cysteine, SAM, electrodeposition, epitaxy, copper, single-crystal, flexible electronics

## 1. INTRODUCTION

In Nature, biominerals such as calcite and magnetite are crystallized at inorganic-organic interfaces to produce highly-ordered inorganic materials with intricate shapes and unique orientations.[1] The crystallization occurs on ordered organic layers with functional groups that control the crystal growth. Functional self-assembled monolayers (SAMs) can serve as biomimetic models for the complex biomolecules that direct the crystallization.[2,3] Functional SAMs of thiols on single crystal metals provide two-dimensional soft templates

for highly-ordered growth of crystalline materials, such as calcite,[4-7] anthracene,[8] and MOFs.[9,10]

Electrodeposition, like biomineralization, is a soft-solution process in which solid materials are crystallized from solution precursors. [11] Epitaxial electrodeposition has been shown to be a simple, low-cost, technology to produce highly-ordered metals[12,13] and semiconductors[14,15] on single-crystal surfaces. However, epitaxial growth on SAMs by electrochemical means has not yet been demonstrated. Although SAM-templated metal electrodeposition has been developed for micro/nano device substrates and pattern formation,[16,17] the electrodeposited metal films were polycrystalline. Polycrystalline electronic materials suffer from electron-hole recombination at grain boundaries.[18]

A single-crystal-like metal film refers to highly-ordered metal with specific in-plane and out-of-plane orientation which can be determined by X-ray analysis. A single-crystal-like Cu film can serve as an inexpensive, highly-ordered conductive substrate for the epitaxial growth of grain boundary-free electronic materials for catalysts,[19] spintronic devices[20] and high temperature superconducting materials.[21] The control of interfacial energies afforded by SAMs enables the epitaxial lift-off of a single-crystal like metal foil that could serve as a conducting substrate for flexible electronic devices such as wearable solar cells,[22] sensors[23] and flexible displays.[24]

Here, we show an electrochemical method to produce epitaxial Cu(111) films on the SAM of the amino acid L-cysteine on Au(111) and lift-off of single-crystal-like Cu foils

for flexible electronics. Our hypothesis is that the functional groups on the L-cysteine SAM are important in directing the epitaxial growth of Cu. In order to test this hypothesis and to determine the role of functional groups in the L-cysteine molecule in the growth of epitaxial Cu, Cu was also electrodeposited onto a SAM of 1-butanethiol on Au(111). The 1-butanethiol molecule does not contain any functional group that can coordinate to Cu(II) ions. The step-by-step electrochemical deposition and lift-off procedure is depicted in Scheme 1. Epitaxial Au(111) was electrodeposited on Si(111) to produce an ordered substrate (Scheme 1A), and an L-cysteine SAM was grown on the Au(111) surface in solution (Scheme 1B). Using the as-prepared L-cysteine SAM on Au(111)/Si(111), an epitaxial Cu(111) film was directly electrodeposited (Scheme 1C). After the deposition, the Cu(111) foil was completely detached from the Au surface by commercial tape without etching (Scheme 1D). Epitaxial perfection and the relationship of the Cu(111) film relative to the Au(111) are determined using X-ray pole figures. Epitaxial Cu(111) films offer a highly-ordered substrate suitable for future flexible electronics at a lower cost than Cu single crystals. In this work, a Cu(111) single-crystal-like foil was used as a substrate for the electrodeposition of epitaxial cuprous oxide ($Cu_2O$) that could serve as a flexible solar cell.[25] This research opens interesting new avenues for epitaxial electrodeposition on functional SAM templates.

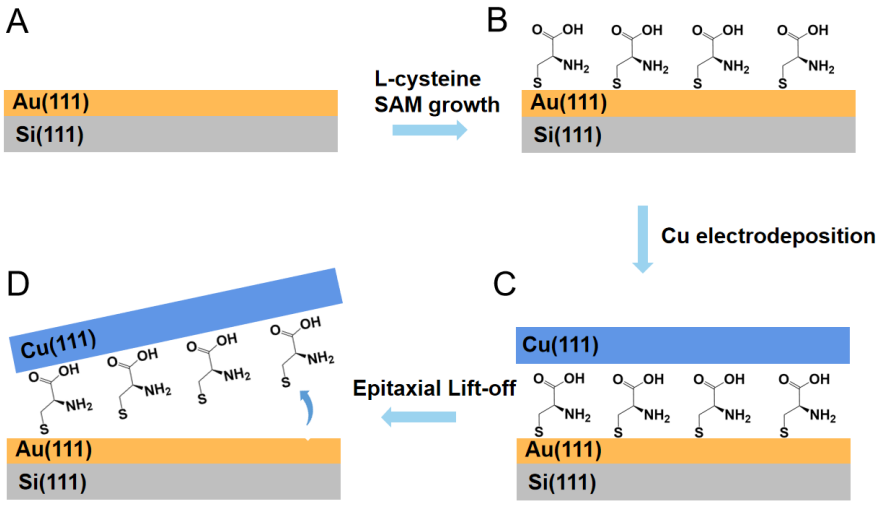


Scheme 1. Epitaxial electrodeposition of Cu(111) onto an L-cysteine self-assembled monolayer on Au(111)/Si(111) and epitaxial lift-off of single-crystal-like Cu foil. (A) Au(111) electrodeposited on Si(111).; (B) L-cysteine SAM grown on Au(111) surface in 10 mM L-cysteine solution for 24 h; (C) Cu(111) electrodeposition from a 20 mM Cu(II) solution at –0.25 V versus Ag/AgCl; (D) Single-crystal-like Cu(111) foil completely detached from the Au surface.

## 2. EXPRIMENTAL SECTION

### 2.1. Si WAFER ETCHING PROCESS AND Au DEPOSITION

N-type Si(111) with a miscut angle of 0.2° towards [11$\bar{2}$] and a resistivity of 1.15 Ω·cm was used. The wafers were purchased from Virginia Semiconductor Inc. and were hydrogen-terminated before use. Wafers were etched in 5% HF acid for 3 minutes to remove the native oxide layer, and then soaked in 90 °C DI water for 15 min to form a $SiO_x$ layer, then etched again with 5% HF acid for 30 s. Gallium-indium eutectic was applied to the back of the Si wafers to form an ohmic contact, followed by silver wire and silver print II (GC electronics) as a back contact. Melted Apiezon Type W wax was used to insulate

the back of the Si substrates. The Au layer was directly electrodeposited onto the Si substrate using a prepolarized bias applied before the immersion of the sample into the solution to prevent the oxidation of Si in the aqueous environment. The plating solution was 0.1 mM $HAuCl_4$, 1 mM KCl, 1 mM $H_2SO_4$ and 0.1 M $K_2SO_4$.[12,26] A potential of -1.9 V vs. Ag/AgCl electrode was used for Au deposition. The Au films were deposited for 30 minutes at room temperature with 200 rpm stirring. An Autolab 30 potentiostat was used for deposition.

## 2.2. PREPARATION OF SELF-ASSEMBLED MONOLAYER PREPARATION ON Au(111)

L-cysteine SAMs were prepared by immersion of the Au(111)/Si(111) substrate into a nitrogen-saturated 10 mM solution of the amino acid L-cysteine in water at room temperature for 24 h. 1-Butanethiol SAMs were prepared by immersion of the Au(111)/Si(111) substrate into a 10 mM solution of 1-butanethiol in ethanol at room temperature, bubbled with nitrogen, for 24 h. Samples were then rinsed with ethanol, DI water and blown dry in a stream of air.

## 2.3. ELECTRODEPOSITION OF COPPER FILMS

Copper was electrodeposited from a plating solution containing 20 mM $CuSO_4$, 100 mM $K_2SO_4$, and 12 mM $H_2SO_4$ in deionized (DI) water at pH 1.8 at room temperature. Ag/AgCl served as the reference electrode, and a Au coil served as a high surface area

counter electrode. A -0.25 V versus Ag/AgCl potential was applied to the Au(111)/Si(111), and the deposition was carried out for various deposition times at room temperature, stirring at 250 rpm. After the deposition, films were rinsed with DI water and dried in air. Free-standing Cu(111) foils were detached from the Au(111) substrates by peeling off the Cu(111) film using adhesive tape.

## 2.4. ELECTRODEPOSITION OF $Cu_2O$ ON A Cu(111) FOIL

Prior to $Cu_2O$ deposition, the Cu(111) foil was washed with 2% dilute HCl solution to remove oxide layers on the surface formed by aerial oxidation. $Cu_2O$ was electrodeposited from a plating solution containing 0.2 M $CuSO_4$, 0.2 M $C_4H_6O_6$ (L-tartaric acid), and 3.0 M NaOH. A cathodic current density of 1.0 mA/cm$^2$ was passed for 1200 s at a temperature of 60 °C and a stir rate of 250 rpm. Electrodeposition of $Cu_2O$ films was done using either an EG&G Model 273A or an Autolab 30 potentiostat/galvanostat.

## 2.5. LINEAR SWEEP VOLTAMMETRY (LSV)

LSVs were acquired on a 1cm x 1cm SAM treated or untreated Au-coated glass electrode in a solution stirred at 1000 RPM. The Au-coated glass electrode was purchased from DRLi Deposition Research Lab, Inc. The 100 nm Au with [111] out-of-plane orientation but no in-plane order is coated on a 40 nm titanium adhesion layer on the glass. The potential was scanned at a scan rate of 20 mV/s.

### 2.6. X-RAY DIFFRACTION MEASUREMENTS

The X-ray diffraction data was acquired using a Philips X'Pert Materials Research diffractometer (XRD) with a CuKα radiation source. 2θ scans were acquired using a 2-bounce hybrid monochromator (PW3147/00) as the incident optic module with a 0.18° parallel plate collimator (PW3098/18) attached to a proportional detector (PW3011/20) on the diffracted beam side. A crossed slit collimator (PW3084/62) with 2 mm divergence slit and 2 mm mask with a Ni filter as the incident optic module and a 0.27° parallel plate collimator (PW3098/27) equipped with a flat graphite monochromator (PW3121/00) as the diffracted beam module were used for X-ray pole figure measurements. The stereographic projections and interface models were constructed using CaRIine crystallography 3.1 and VESTA 3.4.0 software, respectively.

### 2.7. SEM MEASUREMENTS

The surface morphology and thickness of Cu film was measured by plan-view and cross-sectional micrographs obtained with a FEI Helios Nanolab Dualbeam scanning electron microscope with accelerating voltages ranging from 5 to 15 kV.

## 3. RESULTS & DISCUSSION

Prior to the electrodeposition of epitaxial films, the electrochemistry of SAMs on Au and the electrodeposition of Cu onto these SAMs was studied using a sputtered Au on

glass working electrode. The existence of the L-cysteine SAM on Au(111)/glass was first verified by LSV in 0.1M NaOH solution by scanning from -0.2 V to -1 V, as shown in Figure S1. There is a sharp peak around -0.7 V vs. Ag/AgCl corresponding to desorption of L-cysteine SAM, which agrees with previous reports.[27,28] As shown in Figure 1, the stability of L-cysteine SAM (black dash line) and 1-butanethiol SAM (green dash line) are confirmed because no desorption peak is observed in the potential range from -0.5 V to 0.4 V. The existence of SAMs cause negative shifts of the initial potential for Cu bulk deposition compared with bare Au(111)/glass surface (red solid line), showing a 50 mV negative shift on L-cysteine SAM (black solid line) and 200 mV negative shift on 1-butanethiol SAM (green solid line), respectively. A smaller negative shift on L-cysteine SAM than on 1-butanethiol SAM indicates that Cu is easier to nucleate on the surface of L-cysteine SAM, probably because of strong coordination between L-cysteine and Cu(II). This is also confirmed by the additional reductive peak of L-cysteine SAM at 0.135 V, which shows that Cu(II) complexed at the L-cysteine film is reduced to Cu(I).[27,29] The 1-butanethiol SAM does not have the cathodic peak because it lacks functional groups coordinating to Cu(II) ions. Based on the above LSV analysis, Cu deposition on SAMs/Au(111)/Si(111) were performed under constant potential at -0.25 V versus Ag/AgCl in the same solution. Typical current-time curves are shown in Figure S2. The Faradaic efficiency for deposition of Cu on L-cysteine SAM/Au(111)/Si(111) was measured based on the total charge passed versus the total Cu content in the film. The

average Faradaic efficiency was 59%, giving a thickness of 220 nm of Cu for every 1 C/cm$^2$ of cathodic charge (Table S1 in the Supporting Information).

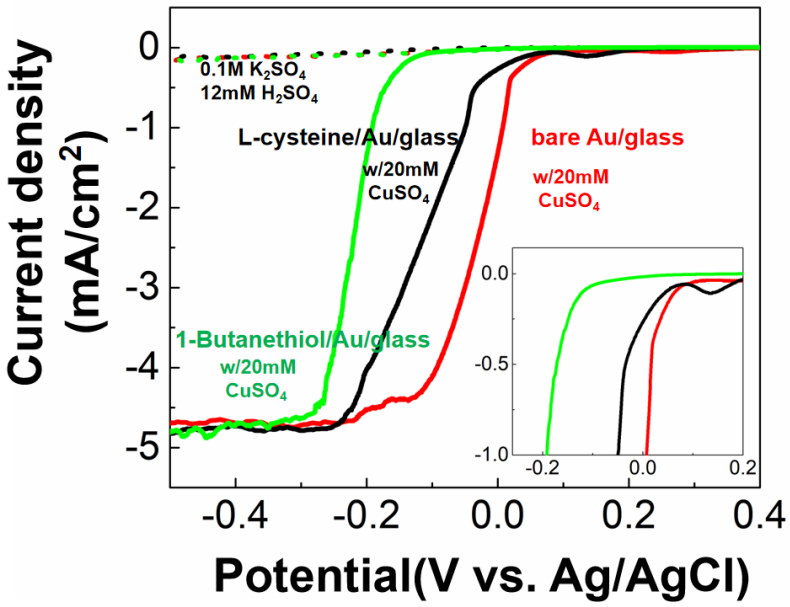


Figure 1. Linear sweep voltammograms of the electrolyte with (solid lines) and without (dash line) Cu(II). Green lines are 1-butanethiol SAM/Au/glass surfaces; black lines are L-cysteine SAM/Au/glass surfaces; Red lines are bare Au/glass surfaces. Inset shows the initial potential for Cu bulk deposition with a 50 mV negative shift on L-cysteine SAM and 200 mV negative shift on 1-butanethiol SAM compared with a bare Au/glass surface. In addition, a reduction peak is observed at ~0.1V on the L-cysteine SAM consistent with Cu(II) complexed at the L-cysteine SAM being reduced to Cu(I).

Figure 2 shows schematic diagrams of Cu films on L-cysteine SAM/Au(111)/Si(111) (Figure 2A) and 1-butanethiol SAM/Au(111)/Si(111) (Figure 2B). The Cu grown on L-cysteine SAM/Au(111)/Si(111) for 200 s has a strong [111] out-of-plane orientation, following the out-of-plane orientation of Au(111) (Figure 2C), whereas Cu grown on 1-

butanethiol SAM/Au(111)/Si(111) shows all of the reflections of polycrystalline Cu, but has a [111] texture (Figure 2D).

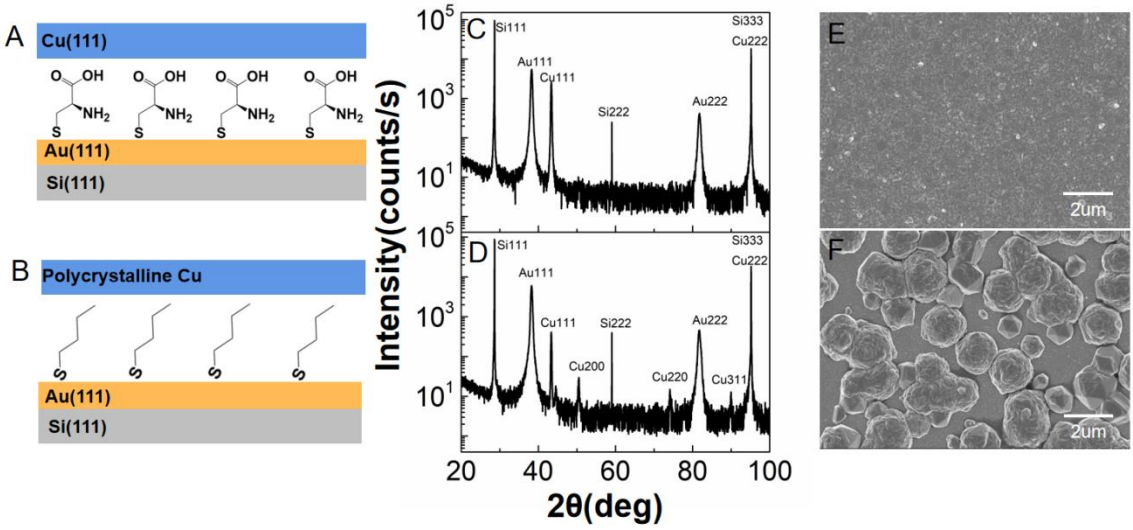


Figure 2. Out-of-plane orientation and surface morphology of electrodeposited Cu films on SAMs. (A) Schematic diagram of epitaxial Cu film on L-cysteine SAM/Au(111)/Si(111); (B) Schematic diagram of polycrystalline Cu film on 1-butanethiol SAM/Au(111)/Si(111); (C) Out-of-plane x-ray diffraction of epitaxial Cu film on L-cysteine SAM/Au(111)/Si(111); (D) Out-of-plane X-ray diffraction of polycrystalline Cu film on 1-butanethiol SAM/Au(111)/Si(111), consistent with polycrystalline growth of Cu; (E) Plan-view SEM image of smooth Cu on L-cysteine/Au(111); (F) Plan-view SEM image of rough and mushroom-like Cu on 1-butanethiol/Au(111).

The Cu grown on the L-cysteine SAM is featureless and compact, indicating the homogeneous nucleation and 2D growth of Cu on the surface of the L-cysteine SAM (Figures 2E, S3A), whereas the Cu grown on the 1-butanethiol SAM is nodular, with a mushroom-like morphology (Figures 2F, S3B). The nodular morphology and polycrystalline nature suggest that the Cu deposition occurs on top of the 1-butanethiol

SAM, but that the SAM does not control the orientation due to the lack of functional groups that can direct the epitaxial growth. Due to the lack of affinity between the 1-butanethiol SAM surface and Cu, the metal cannot nucleate and spread on the SAM surface. Once Cu starts nucleating with a variety of orientations, it prefers to grow on itself instead of the SAM, forming the 3D nodular morphology (Figure S4). That is, the overpotential for growth of Cu on Cu is lower than the overpotential for nucleation of Cu on the 1-butanethiol SAM.

The in-plane ordering was probed with a (200) pole figure for Cu and Au film, and (220) pole figure for the Si substrate (Figure 3). The orientation of the SAMs relative to the Au and Si cannot be determined by this method, because the SAMs are too thin to diffract X-rays. The Si(220) pole (Figure 3A) shows three intense spots at a tilt angle ($\chi$) of 35.5°. This corresponds to the 3-fold symmetry of the (111) plane and the angle between the (220) and (111) planes of 35.5°. The Au(200) pole (Figure 3B) shows six intense spots at a tilt angle ($\chi$) of 54.74°. The spots occur at a tilt angle corresponding to the angle between the (111) and (200) planes. Although the (111) plane only has 3-fold symmetry, there are six spots because the Au deposits with both a parallel and antiparallel in-plane orientations relative to the Si(111).[12] The Cu(200) pole figure of Cu/L-cysteine shows six spots separated 60° azimuthally at a tilt angle ($\chi$) of 54.74°, revealing that the Cu film (Figure 3C) indeed grows epitaxially, which agrees with the tilt angle of the calculated

stereographic projection for single-crystal-like Cu(111) shown in Figure S5A in the Supporting Information.

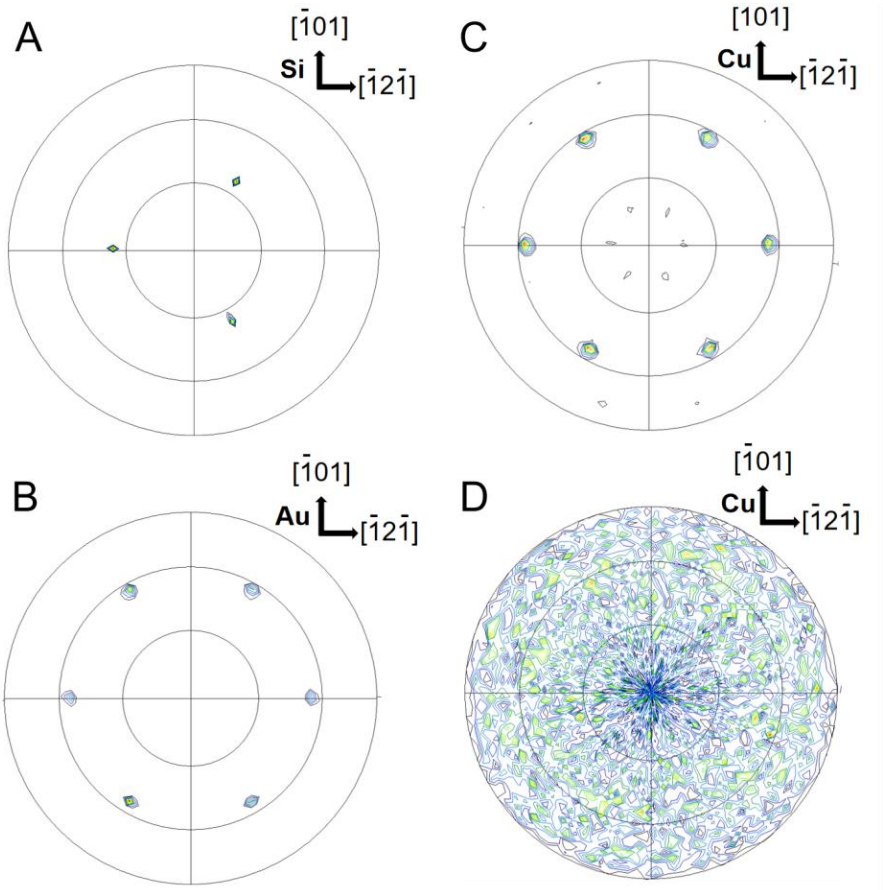


Figure 3. In-plane orientation of electrodeposited Cu films on SAMs. (A) (220) pole figure for Si(111); (B) (200) pole figure for Au(111) substrate; (C) (200) pole figure for Cu on L-cysteine SAM; (D) (200) pole figure for Cu on 1-butanethiol SAM. The concentric grid lines on the pole figures correspond to 30° increments of the tilt angle, $\chi$.

An epitaxial relationship consistent with these pole figures is Cu(111)[ $\bar{1}$ 01]//Au(111)[$\bar{1}$01]//Si(111)[$\bar{1}$01]. In addition to the 6 high intensity major spots, minor spots occur at $\chi = 15°$ and $\chi = 77°$. These low intensity spots arise from a small amount of

the [511] orientation, which is the result of twinning along {111} slip planes, according to the calculated stereographic projection of Cu(111) in Figure S5B. Owing to the very low intensity of the [511] orientation compared to the [111] orientation as shown in the 2.5D projection Cu(200) pole figure in Figure S6A, we can only see some of the spots from the [511] orientation in Figure 3C. The polycrystalline nature of Cu on 1-butanethiol SAM is also confirmed by probing the in-plane orientation, as shown in Figure 3D and more specifically in Figure S6B. No spots are observed in the (200) pole figure Cu deposited on the 1-butanethiol SAM, consistent with an absence of in-plane order. Therefore, these results indicate the importance of the -COOH and -$NH_2$ functional groups of L-cysteine in directing the epitaxial growth of Cu on Au(111).

Azimuthal scans were acquired for the Cu films on the L-cysteine SAM by setting the 2θ equal to the (200) reflection for Au and Cu, respectively, and tilting to $\chi = 54.74^{o}$ (Figure 4A, 4B). The scans were then recorded as the sample was rotated from 0 to $360^{o}$ azimuthally. By overlaying the Cu azimuthal with the Au azimuthal, it is clear that the Cu follows the in-plane orientation of the Au substrate. Interface models of Cu(111) with Au(111) are shown in Figure 4C. Cu with lattice parameter 0.3615 nm and fcc space group $Fm\bar{3}m$ is deposited onto the L-cysteine monolayer on Au with lattice parameter 0.40786 nm and fcc space group $Fm\bar{3}m$. The mismatch between lattice of Cu (111) and Au (111) is -11.37%. This mismatch is lowered to -0.29% by forming a coincident site lattice in which 9 unit meshes of Cu coincide with 8 unit meshes of Au.

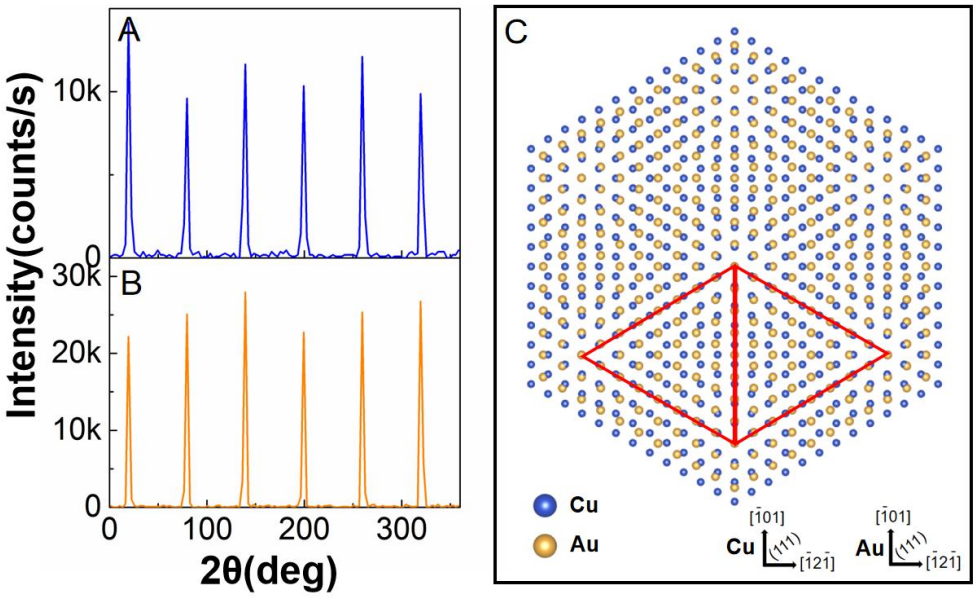


Figure 4. Epitaxy perfection and relationship of Cu(111) to Au(111) substrate. (A) Azimuthal scan of Cu(111) at $\chi = 54.74°$; (B) Azimuthal scan of Au(111) at $\chi = 54.74°$; (C) Interface model of Cu(111) (blue) with Au (111) (yellow). A coincidence site lattice is formed by 9 unit meshes of Cu coinciding with 8 unit meshes of Au which results in a mismatch of -0.29%.

The existence of SAMs between Au/Cu interface after Cu deposition was confirmed by a peel-off test (Figure S7). The control of interfacial energies afforded by SAMs enables the lift-off of Cu foil. Cu foils from 1-butanethiol SAM/Au (Figure S7A) and L-cysteine SAM/Au (Figure S7B) can be easily peeled-off by commercially available tape, whereas, Cu on bare Au (Figure S7C) cannot be lifted-off due to the very strong intermetallic interaction between the Cu film and Au substrate. In addition, from the cross-sectional SEM image shown in Figure S3A, the uniform Cu film clearly has not adhered to the substrate well since there is a gap between the Cu film and Au, which supports the fact that the SAM still being there. According to this phenomenon, we believe that the L-

cysteine SAM functions as an interfacial template, instead of desorption or replacement during Cu electrodeposition.

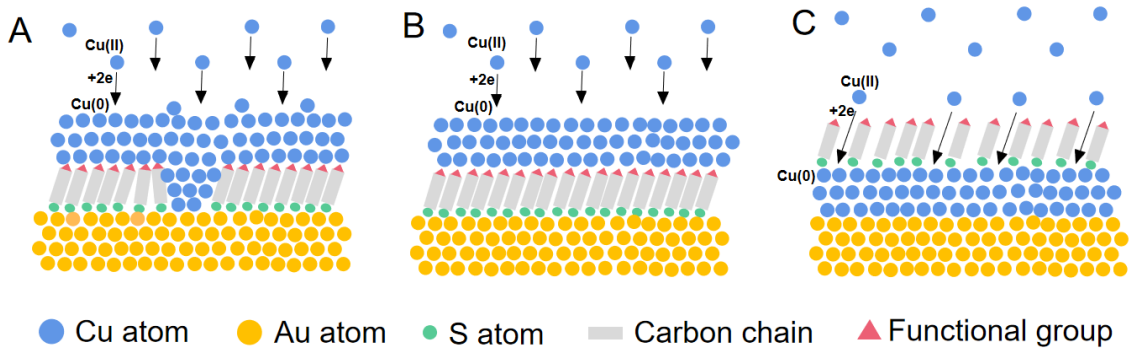


Figure 5. Schematic of three possible mechanisms of Cu(111) deposition on L-cysteine SAM/Au(111). (A) Defect-mediated deposition: Cu nucleates from the defects in the SAM and grows on top of the SAM; (B) Coordination-controlled deposition: Cu nucleates and grows directly on top of SAM via functional groups; (C) UPD replacement deposition: Cu deposits underneath SAM connecting to the Au surface.

To get a better insight on the growth and epitaxial lift-off of Cu films, three distinctly different possible mechanisms are depicted in Figure 5 and described as follows. First, a more commonly employed strategy is illustrated in Figure 5A known as defect mediated electrodeposition.[30-32] In this mechanism, Cu nucleates and grows at SAM-free areas or defects in the SAM. In this case, the epitaxial relationship between Cu and Au can be easily explained because nucleation of Cu directly starts at the Au(111) surface. The second, less explored deposition scheme, illustrated in Figure 5B is coordination-controlled electrodeposition,[33,34] that is achieved by electrochemical reduction of ions coordinated to a SAM. This relies on the chemical functionality of SAM molecules and promises a more

active control of the deposition process. This mechanism is likely, because the -COOH and -$NH_2$ groups in L-cysteine molecule exhibit strong complexing ability with Cu(II) ions, and is the reason that cysteine-modified Au electrodes have been applied in sensitive detection of Cu ions.[35] A possible structure of the Cu(L-cysteine)$_2$ complex at the gold surface is shown in Figure S8. Each Cu(II) ion is complexed by two cysteine molecules having -COOH and -$NH_2$ groups to form four coordinate covalent bonds to Cu(II).[27] In the third possible mechanism, illustrated in Figure 5C, UPD of Cu takes place reversibly through the SAM layer, so Cu grows underneath the SAM in contact with the Au.[36] This mechanism is consistent with the Cu orientation being determined by the Au. However, this mechanism appears unlikely, because it cannot explain why the Cu film can be easily lifted off from Au surface, due to the very strong intermetallic interaction between a Cu film and Au substrate. From the SEM analysis (Figures 2E and 2F) and the fact that the film is easy peeled-off to form a single-crystal-like foil supports the idea that the formation of epitaxial Cu(111) on L-cysteine/Au(111) is more likely via coordination-controlled mechanism in Figure 5B.

Further, it is well known that the alkanethiols are arranged in a ($\sqrt{3}$ x$\sqrt{3}$)R30° or c(4 x 2) structure with the tilt angle of 30° from the surface normal.[37-39] The 1-butanethiol SAM on Au(111) has been confirmed to have a high coverage c(4 x 2) phase, as shown in Figure S9, with a rectangular structure of ($2\sqrt{3}$ × 3)R30° for the adlayer of 1-butanethiol.[40,41] Because of the relatively flexible carbon chain in the 1-butanethiol molecule, 1-butanethiol

molecules could be either parallel (conformation I) or tilted (conformation II) relative to the normal direction of the Au(111) plane. Also, the SAM molecule parameters, such as the tilt angle α (30°), and the twist angle of the alkane chains β (+35° and -55°), and the tilt direction δ (23°), are well established for alkanethiols,[5] as shown in Figure S10.

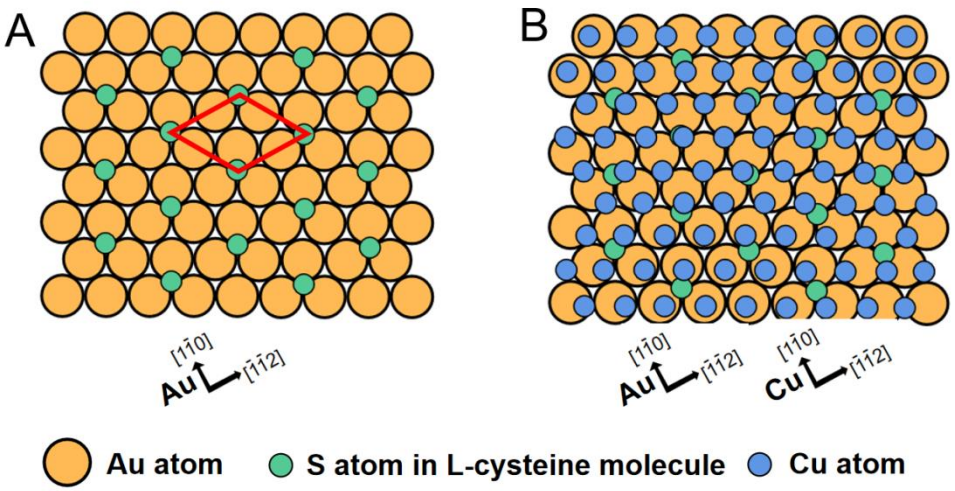


Figure 6. 2D schematic drawing of surface structure of L-cysteine SAM on Au(111) plane and Cu lattices on L-cysteine SAM. (A) (√3 x√3)R30° structure for L-cysteine SAM on Au(111); (B) Cu(111) lattice on (√3 x√3)R30° structure of L-cysteine SAM on Au(111).

However, there is still controversy about the actual surface structure about L-cysteine SAM on Au(111).[42-45] L-cysteine is a small and highly polar chiral molecule in which a variety of intermolecular forces, such as hydrogen and electrostatic bonding, can govern its packing on a gold surface. L-cysteine SAM on Au(111) has been mostly reported as an hexagonal lattice of (√3 x√3)R30°,[42,43] however, utilizing different preparation conditions for L-cysteine SAM, (3√3 x 6)R30° structures[44] and (4 x √7)R19° structures[45]

were also observed. Here we take the (√3 x√3)R30° structure for standard model of L-cysteine SAM on Au(111), as shown in Figure 6A. The green spots indicate the adsorption site of the L-cysteine molecule especially the position of Au-S bond. The unit cell contains one molecule, and its area is 0.2165 $nm^2$ with 33% surface coverage. With the above data, and the known parameters for the orientation of the L-cysteine molecules in SAM with respect to an Au(111) film, a model can be constructed in which only the positions of the different Cu, Au atoms and L-cysteine molecules are taken into account (Figure 6B).

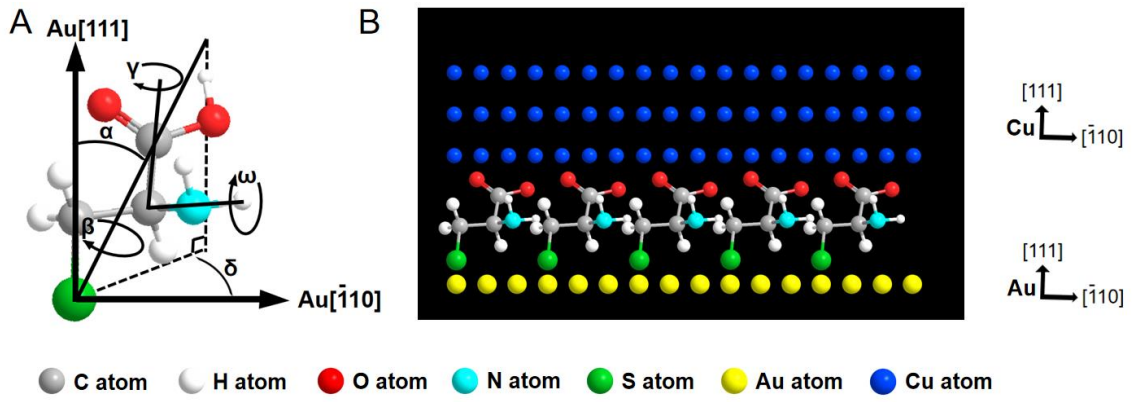


Figure 7. 3D models of L-cysteine and Cu lattice on L-cysteine SAM on Au(111). (A) L-cysteine and its degrees of freedom. In our model, the tilt angle α is 30° and the tilt direction δ is 23°. The twist angle for the (√3 x √3)R30° model is β= 55°. The carboxylic acid endgroup is free to rotate around γ and the amino endgroup is free to rotate around ω; (B) 3D model of Cu with their {111} faces on L-cysteine SAM on Au(111).

As shown in Figure 7A, L-cysteine SAM molecule parameters are also established as the tilt angle α (30°), and the twist angle of the alkane chains β (55°), and the tilt direction δ (23°) following the typical (√3 x√3)R30° SAM.[5] A simple 3D model is constructed which

takes into account all known parameters of a SAM of thiols on Au(111) as shown in Figure 7B. To get a better idea about the precise interactions between the -COOH and -$NH_2$ groups of the SAM and the Cu lattice, spatial conformation of L-cysteine molecule on Au(111) is drawn as Figure S11A following reported papers[44] and possible coordination site of L-cysteine SAM is shown in Figure S11B. Possible coordination site of two adjacent molecules, in which -COOH, -$NH_2$ groups and Cu(II) form four coordinate complexation, matches with Cu lattice by every 7 unit meshes of Cu with 2 unit meshes of L-cysteine SAM (Figure S11C) and results in a mismatch of +3.41%. The Cu can subsequently nucleate or spread on these sites. The information available about the orientation of the -COOH and -$NH_2$ groups of the thiols is limited, as well as the effect of hydrogen bonding and "multiple layers" effect, so what actually happens may be more complicated. However, it is still of general interest to create such a model because it illustrates the complexity of the problem of epitaxial growth behavior of Cu on organic substrates. In addition, because the SAM is a soft, compliant surface, it may be easier to minimize the effect of lattice mismatch than might be observed with a hard, inorganic substrate.

One application of metal electrodeposition on SAMs is to produce thin metallic foils and/or to fabricate nano/micropatterned electrodes, molds and replica of different materials.[17] Although Cu foils from different SAM have been obtained, no epitaxial Cu films have been reported. Polycrystalline electronic materials suffer from electron-hole recombination at grain boundaries. Although an epitaxial Cu foil has been be prepared by

electrodeposition on a Si wafer,[46] the orientation is only [100], and the lifting off process requires HF solution etching that limits its commercial application.[26]

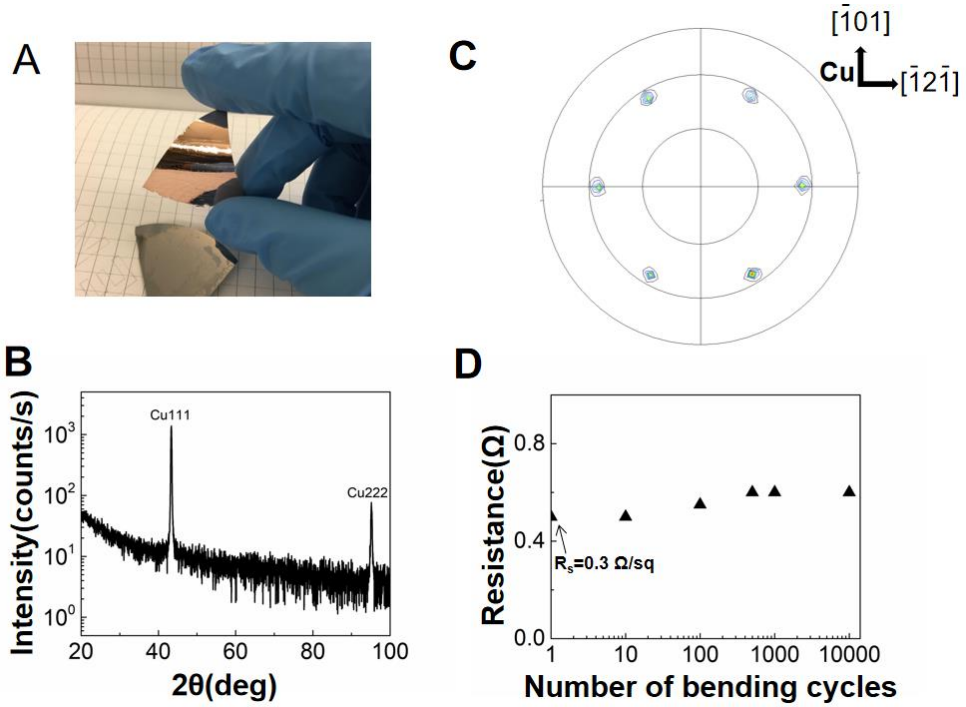


Figure 8. Out-of-plane orientation, in-plane orientation, two-electrode resistance and flexibility of a 128 nm thick single-crystal-like Cu(111) foil lifted-off from L-cysteine/Au(111)/Si(111). (A) Optical image of 128 nm thick Cu(111) foil; (B) Out-of-plane x-ray diffraction of Cu(111) foil; (C) (200) pole figure of Cu(111) foil; (D) Two-electrode resistance of 128 nm thick 2 cm x 2 cm Cu(111) foil as a function of bending cycles.

The epitaxial electrodeposition of Cu film on L-cysteine/Au(111) allows for simple epitaxial lift-off of the Cu(111) film to produce flexible single-crystal-like Cu(111) foils, as shown in Figure 8A. A polymer adhesive (tape or hot glue) is applied to the deposited Cu surface as a support and facilitator for easy foil separation without any other operation

like etching. The resultant single-crystal-like Cu foil has X-ray reflections solely from the {111} family in the 2θ diffraction pattern (Figure 8B), and the Cu(200) pole figure again shows six high intensity spots at $\chi = 54.74°$ from the Cu(111), each separated azimuthally by 60° (Figure 8C). A small amount of the [511] orientation twinning within the foil sometimes cannot be seen in 2D pole figure because of very low intensity. The as-prepared Cu foil exhibits a low resistivity of $3.75 \times 10^{-8}$ Ω·m, which compares with the bulk resistivity of copper of $1.72 \times 10^{-8}$ Ω·m. The 2 cm x 2 cm copper foil with 128 nm thickness exhibits a sheet resistance of only 0.3 Ω/square. The endurance of the Au foils as a function of two-electrode resistance is measured by subjecting the foils to as many as 10,000 bending cycles (Figure 8D). The resistance of 128-nm-thick Cu foil increased by 12% after 10,000 cycles of bending.

In order to know whether the L-cysteine SAM film lifted together with the Cu film, we did two tests as shown in Figure S12. Figure S12A shows the LSV of L-cysteine SAM/Au/glass after peeling off Cu foil in 0.1M NaOH from $-0.2V_{Ag/AgCl}$ to $-1V_{Ag/AgCl}$. The curve shows no sharp desorption peak of L-cysteine around -0.7 V indicating that the L-cysteine SAM does not remain on the Au substrate after peeling off the Cu film. Figure S12B shows a peel test after re-deposition of Cu on the Au/glass substrate after peeling off the Cu foil. Even using the same electrodeposition conditions, re-deposited Cu foil cannot be peeled off again, which is consistent with the LSV test. These results indicate that L-cysteine SAM is lifted with the as-deposited Cu foil. Although -SH group has relatively

strong interaction with Au substrate, the interaction between Cu/L-cysteine appears to be stronger than the -SH/Au interaction.

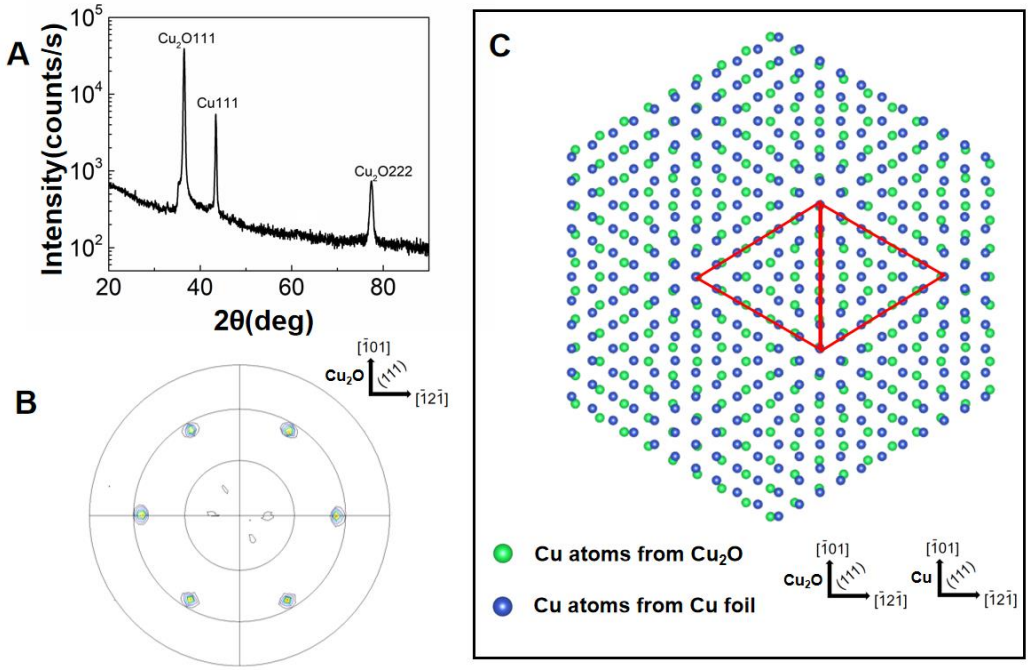


Figure 9. Out-of-plane orientation, in-plane orientation and interface model of epitaxial $Cu_2O(111)$ electrodeposited on Cu(111) foil lifted-off from L-cysteine SAM. (A) Out-of-plane x-ray diffraction of $Cu_2O(111)$ on Cu(111) foil; (B) (200) pole figure for $Cu_2O(111)$; (C) Interface model of $Cu_2O$ (111) (green) with Cu (111) (blue). A coincidence site lattice is formed by 5 unit meshes of Cu from $Cu_2O$ film coinciding with 6 unit meshes of Cu from Cu foil and results in a mismatch of -1.58%.

Such a single-crystal-like epitaxial Cu foil can serve as a simple, large area and low-cost substrate for the epitaxial growth of grain boundary-free flexible electronic materials. In this paper, we present an example of utilizing the Cu foil as a substrate to electrodeposit epitaxial $Cu_2O(111)$. The deposition of $Cu_2O$ was performed from a solution containing 0.2 M $CuSO_4$, 0.2 M $C_4H_6O_6$ (L-tartaric acid), and 3.0 M NaOH at a constant

cathodic current density of 1.0 mA/cm$^{-2}$ at 60 °C for 1200 s. As shown in the XRD patterns in Figure 9A, the epitaxial $Cu_2O$ followed the out-of-plane orientation of Cu(111) foil The $Cu_2O$(200) pole figure shown in Figure 9B again shows six high intensity spots at $\chi = 54.74°$ from the $Cu_2O$(111), each separated azimuthally by 60° (Figure 9B) consistent with in-plane orientation. An epitaxial relationship consistent with the pole figure is $Cu_2O(111)[\bar{1}01]//Cu(111)[\bar{1}01]$. Low intensity spots at $\chi = 15°$ and $\chi = 77°$ due to $Cu_2O$ are the result of a small amount of the [511] orientation twinning along {111} slip planes, following the orientation of [511] orientation of Cu foil. An interface model of $Cu_2O$(111) on Cu(111) is shown in Figure 9C. $Cu_2O$ with lattice parameter 0.42696 nm and primitive space group $Pn\bar{3}m$ is deposited onto Cu with lattice parameter 0.3615 nm and fcc space group $Fm\bar{3}m$. A coincidence site lattice can be formed by six Cu atoms in the $Cu_2O$ plane to every seven Cu atoms in the Cu plane. The misfit for this coincidence lattice is -1.58%, compared with the calculated unit cell misfit of 18.1%. This type of flexible, epitaxial $Cu_2O$/Cu system could pave the way for single crystalline and flexible solar cells.[25] The of Cu(111) foil substrate could also be used to grow cuprous halide films for inexpensive and flexible blue LED devices.[47]

## 4. CONCLUSIONS

As an example of epitaxial growth on SAMs by electrochemical means, we show that epitaxial Cu films can be electrodeposited on an L-cysteine self-assembled monolayer

on the single-crystal-like Au(111) surface. Cu follows the Au(111) out-of-plane and in-plane orientation with a small amount of twinned [511] orientation. Defect-mediated and coordination-controlled electrodeposition mechanisms are two possible deposition mechanisms. Because of the functional groups -COOH and -$NH_2$ providing strong coordination interaction with Cu(II), Cu on L-cysteine/Au(111) grows epitaxially, whereas Cu on 1-butanethiol/Au(111) yields a textured Cu film with no in-plane order. The L-cysteine SAM allows Cu(111) to be easily lifted off, which is evidence that the Cu film grows on top of the L-cysteine SAM. The Cu(111) foil can also be used as a highly-ordered, conductive substrate for flexible electronic materials. Here, we electrodeposit epitaxial $Cu_2O$ on surface of a Cu(111) foil that could be used to produce a flexible solar cell.

This research also opens interesting new avenues for epitaxial electrodeposition on functional SAM templates. The epitaxial growth can be tuned by varying the functional groups on the SAM. Other metals such as Pt, semiconductors such as $Cu_2O$, and topological insulators such as $Bi_2Te_3$ have potential to be epitaxially electrodeposited on a SAM with suitable functional groups to produce flexible devices. Because the L-cysteine molecule is chiral, it may also be possible to effect chiral crystallization on the SAM surface by electrodeposition.

## SUPPLEMENTARY INFORMATION

# EPITAXIAL ELECTRODEPOSITION OF Cu(111) ONTO AN L-CYSTEINE SELF-ASSEMBLED MONOLAYER ON Au(111) AND EPITAXIAL LIFT-OFF OF SINGLE-CRYSTAL-LIKE Cu FOILS FOR FLEXIBLE ELECTRONICS

*Bin Luo, Avishek Banik, Eric W. Bohannan, and Jay A. Switzer**

Department of Chemistry and Graduate Center for Materials Research, Missouri University of Science and Technology, Rolla, MO 65409-1170, USA.

## SUPPLEMENTARY FIGURES

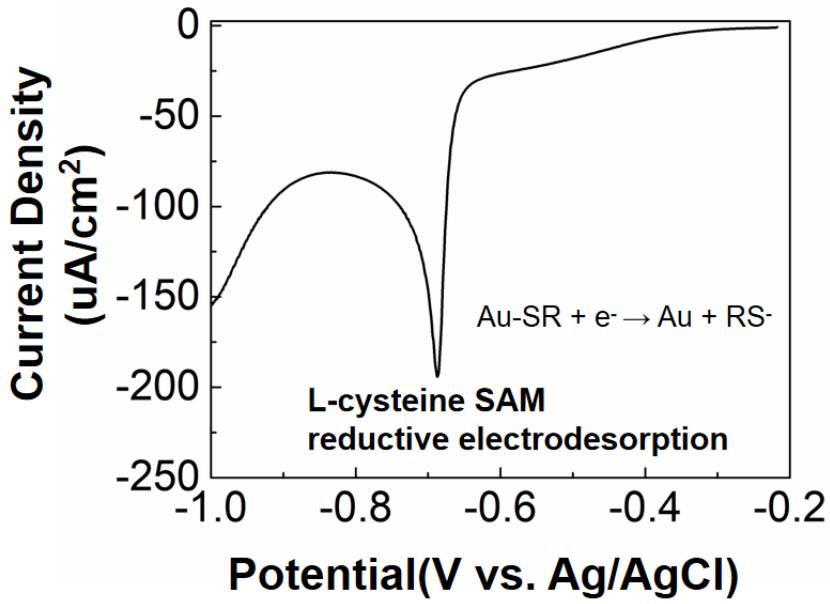


Figure S1. Typical LSV of L-cysteine SAM/Au(111)/glass in 0.1M NaOH from -0.2$V_{Ag/AgCl}$ to -1$V_{Ag/AgCl}$ showing sharp desorption peak of L-cysteine around -0.7 V.

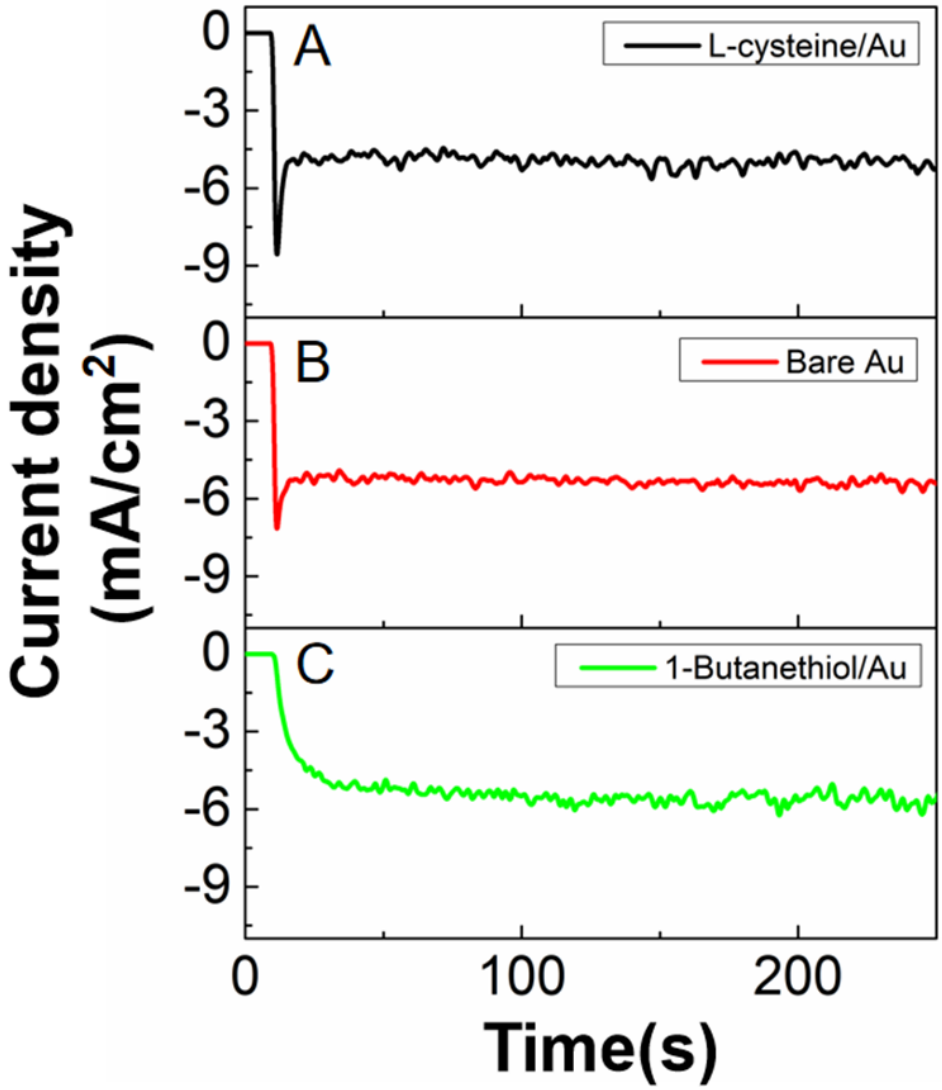


Figure S2. Typical current-time curves of Cu deposition on (A) L-cysteine/Au(111)/Si(111), (B) bare Au(111)/Si(111) and (C) 1-butanethiol/Au(111)/Si(111) at -0.25 V vs $V_{Ag/AgCl}$ in 100 mM $K_2SO_4$, 12 mM $H_2SO_4$ and 20 mM $CuSO_4$ at room temperature.

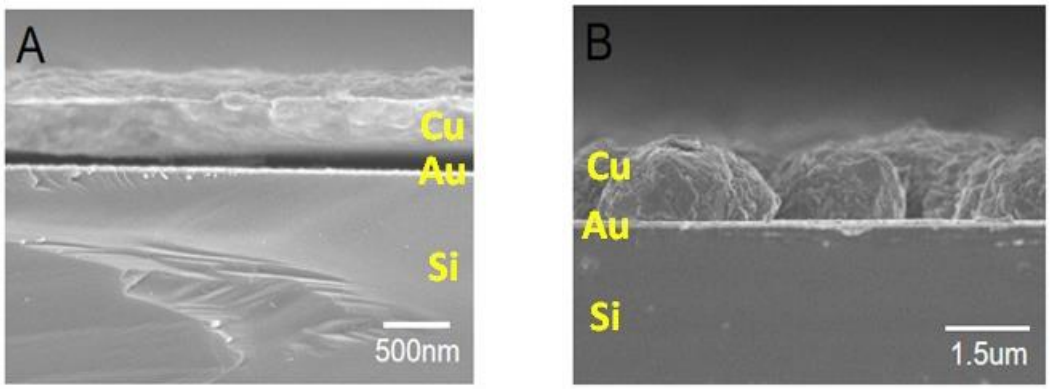


Figure: S3. Scanning electron microscope (SEM) images of Cu films on two kinds of SAMs. (A) cross-section view SEM image of smooth Cu on L-cysteine/Au(111)/Si(111); (B) cross-section view SEM image of mushroom-like Cu on 1-butanethiol/Au(111)/Si(111).

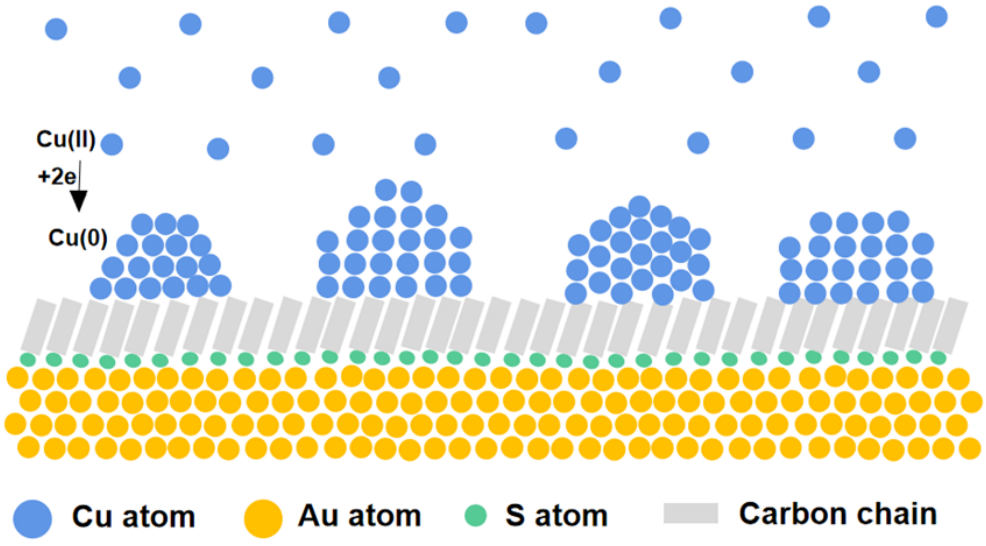


Figure S4. Schematic representation of proposed mechanism of polycrystalline Cu deposition on 1-butanethiol SAM/Au(111). Due to the lack of functional groups that can direct the epitaxial growth, Cu starts nucleating with a variety of orientations and prefers to grow on itself instead of the SAM, forming the 3D globular morphology.

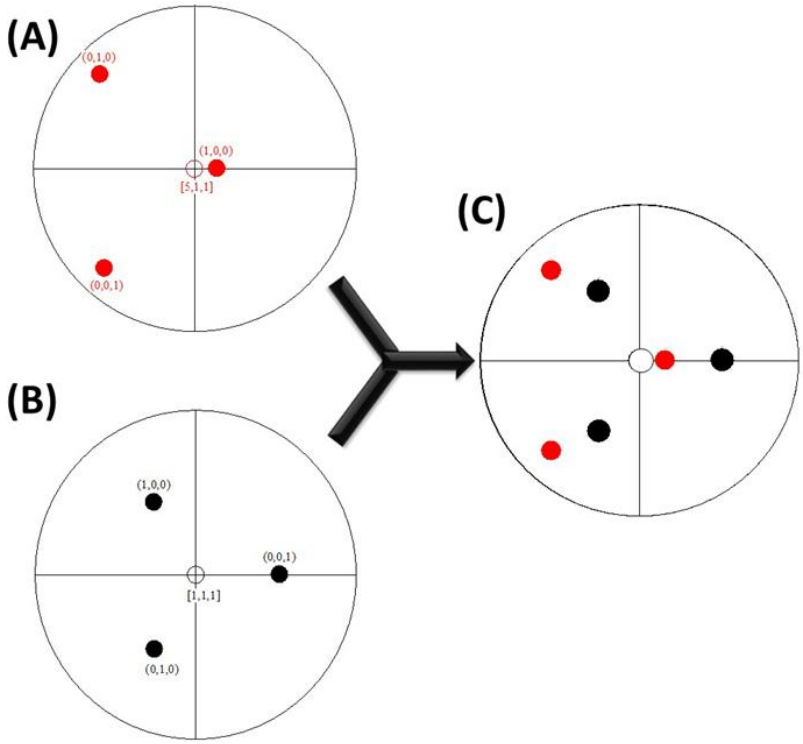


Figure S5. Stereographic projections for (200) pole of ideal single crystal Cu(111) having [111] (A) or [511] (B) out-of-plane orientation. Overlaying both the (200) poles for a single domain (C).

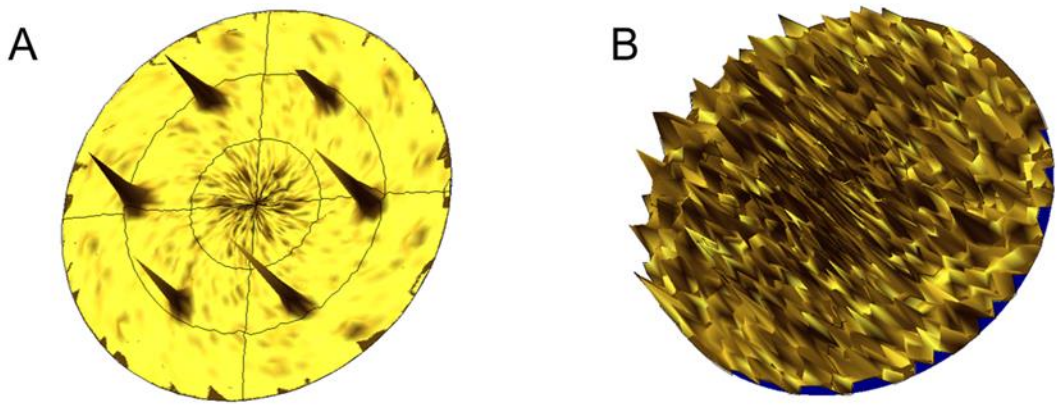


Figure S6. 2.5D projections of Cu (200) pole figures of Cu/L-cysteine/Au(111)/Si(111) (A) and Cu/1-butanethiol/Au(111)/Si(111) (B).

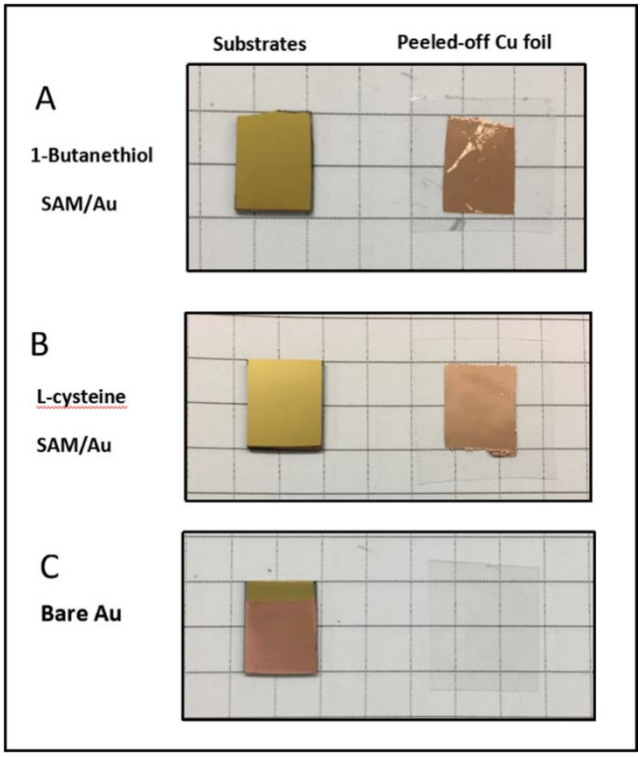


Figure S7. Peel test of Cu foil from (A) 1-butanethiol/Au/glass, (B) L-cysteine/Au/glass and (C) bare Au/glass substrates. The exhibited Cu surfaces are the inner faces contacting with SAMs before peel-off operation by tape.

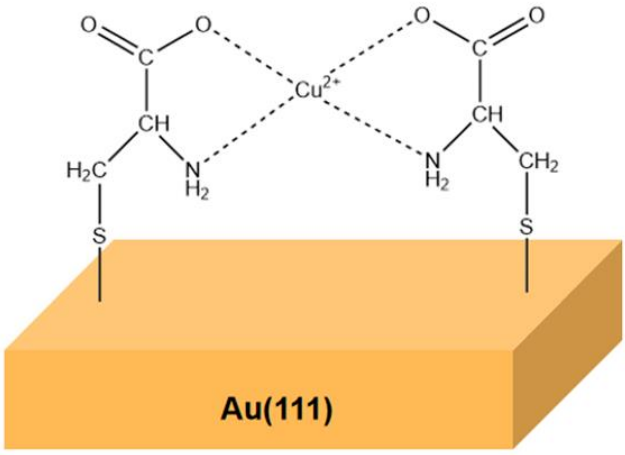


Figure S8. Possible structure of the Cu(L-cysteine)$_2$ complex at a gold surface.

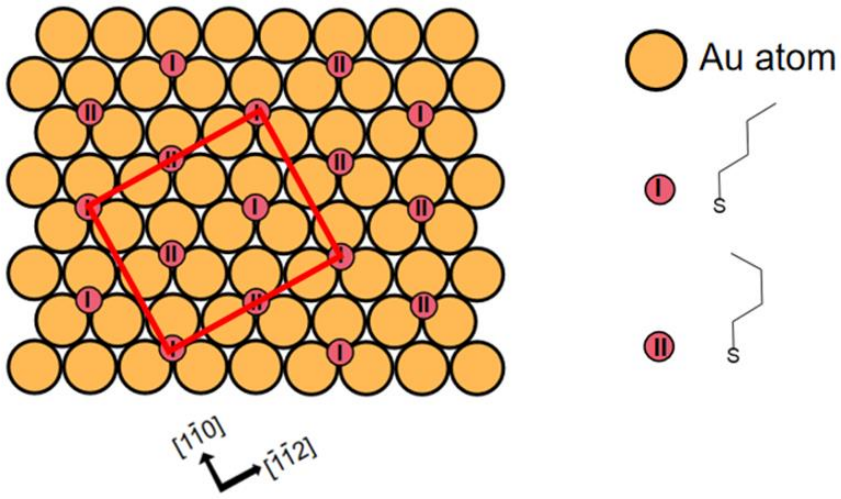


Figure S9. 2D schematic drawing of c(4 x 2) structure for the adlayer of 1-butanethiol SAM on Au(111). 1-butanethiol molecules could be either parallel (conformation I) or tilted (conformation II) relative to the normal direction of the Au(111) plane.

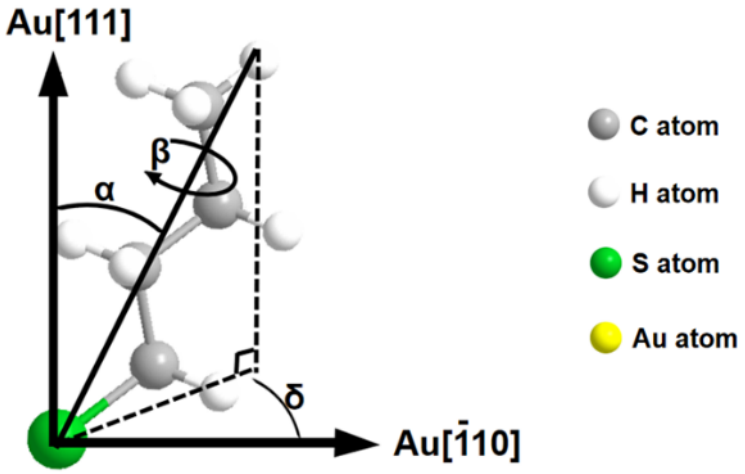


Figure S10. 3D model of 1-butanethiol and its degrees of freedom. In this model, the tilt angle α is 30° and the tilt direction δ is 23°. The twist angle for the c(4 x 2) model is β= +35° and -55°.

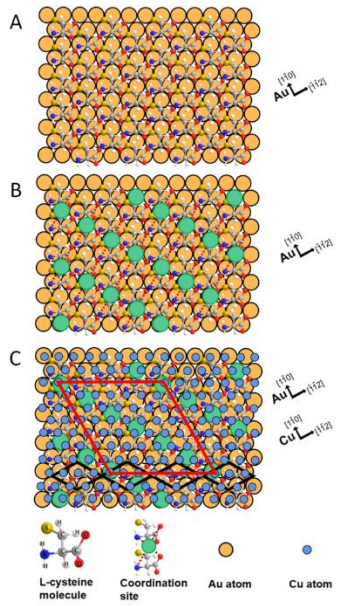


Figure S11. Schematic drawing of possible coordination site of L-cysteine SAM and relationship with Cu lattice on Au(111). (A) Possible spatial conformation of L-cysteine molecule on Au(111); (B) possible coordination site of L-cysteine SAM; (C) Diagram of Cu lattice matching with coordination site of L-cysteine SAM in every 7 unit meshes of Cu with 2 unit meshes of L-cysteine SAM and results in a mismatch of +3.41%.

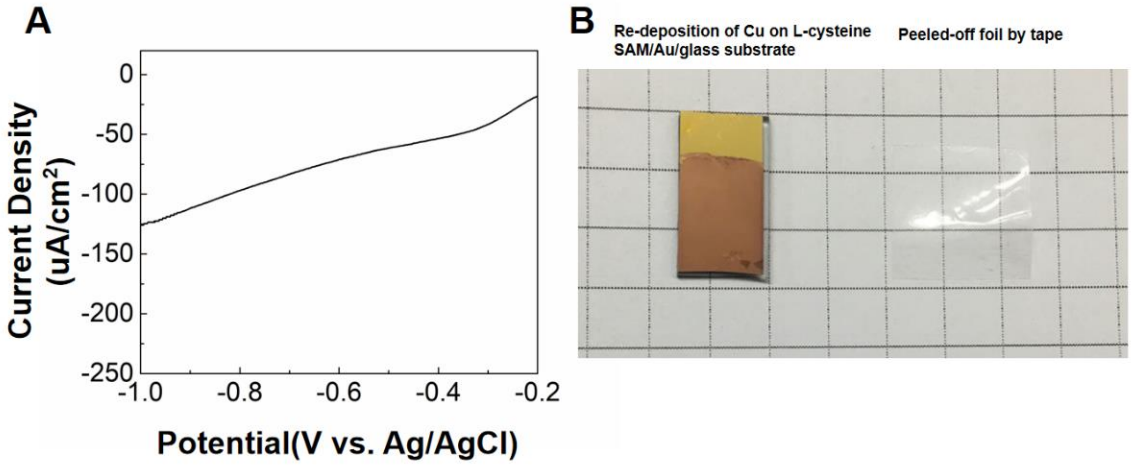


Figure S12. Evidence for L-cysteine SAM lifted together with the Cu(111) film. (A) LSV of L-cysteine SAM/Au/glass after peeling off Cu foil in 0.1M NaOH from -0.2$V_{Ag/AgCl}$ to -1$V_{Ag/AgCl}$ showing no sharp desorption peak of L-cysteine around -0.7 V; (B) Peel test of re-deposition of Cu on L-cysteine SAM/Au/glass substrate after peeling off Cu foil. Re-deposited Cu foil cannot be peeled off again.

## SUPPLEMENTARY TABLES

Table S1: Properties of Cu deposited on L-cysteine/Au(111)/Si(111).

| **Category** | **Time (s)** | **Charge (C)** | **Area ($cm^2$)** | **Thickness Calculated (nm)** | **Thickness experimental (nm)** | **Faradaic Efficiency** | **Experimental resistivity (Ω·m)** |
|---|---|---|---|---|---|---|---|
| Cu/L-cysteine /Au/Si(111) | 600 | 3.69 | 2 | 678 | 400 | 59% | $3.75x10^{-8}$ |

## ACKNOWLEDGMENT

This material is based on work supported by the U.S. Department of Energy, Office of Basic Energy Sciences, Division of Materials Sciences and Engineering, under grant No. DE-FG02-08ER46518.

# REFERENCES


[1] S. Mann *et al.*, "Crystallization at inorganic-organic interfaces: biominerals and biomimetic synthesis," *Science,* vol. 261, no. 5126, pp. 1286-1292, 1993.

[2] J. C. Love, L. A. Estroff, J. K. Kriebel, R. G. Nuzzo, and G. M. Whitesides, "Self-assembled monolayers of thiolates on metals as a form of nanotechnology," *Chemical reviews,* vol. 105, no. 4, pp. 1103-1170, 2005.

[3] J. Aizenberg, A. J. Black, and G. M. Whitesides, "Control of crystal nucleation by patterned self-assembled monolayers," *Nature,* vol. 398, no. 6727, pp. 495-498, 1999.

[4] J. Aizenberg, A. J. Black, and G. M. Whitesides, "Oriented growth of calcite controlled by self-assembled monolayers of functionalized alkanethiols supported on gold and silver," *Journal of the American Chemical Society,* vol. 121, no. 18, pp. 4500-4509, 1999.

[5] A. M. Travaille *et al.*, "Highly oriented self-assembled monolayers as templates for epitaxial calcite growth," *Journal of the American Chemical Society,* vol. 125, no. 38, pp. 11571-11577, 2003.

[6] J. Ihli *et al.*, "Strain-relief by single dislocation loops in calcite crystals grown on self-assembled monolayers," *Nature communications,* vol. 7, no. 1, p. 11878, 2016.

[7] A. M. Travaille, E. G. Steijven, H. Meekes, and H. van Kempen, "Thermodynamics of epitaxial calcite nucleation on self-assembled monolayers," *The Journal of Physical Chemistry B,* vol. 109, no. 12, pp. 5618-5626, 2005.

[8] A. L. Briseno *et al.*, "Patterned growth of large oriented organic semiconductor single crystals on self-assembled monolayer templates," *Journal of the American Chemical Society,* vol. 127, no. 35, pp. 12164-12165, 2005.

[9] E. Biemmi, C. Scherb, and T. Bein, "Oriented growth of the metal organic framework $Cu_3(BTC)_2(H_2O)_3$ xH2O tunable with functionalized self-assembled monolayers," *Journal of the American Chemical Society,* vol. 129, no. 26, pp. 8054-8055, 2007.

[10] J. Liu *et al.*, "Deposition of metal-organic frameworks by liquid-phase epitaxy: The influence of substrate functional group density on film orientation," *Materials,* vol. 5, no. 9, pp. 1581-1592, 2012.

[11] E. A. Kulp and J. A. Switzer, "Electrochemical biomineralization: The deposition of calcite with chiral morphologies," *Journal of the American Chemical Society,* vol. 129, no. 49, pp. 15120-15121, 2007.

[12] N. K. Mahenderkar *et al.*, "Epitaxial lift-off of electrodeposited single-crystal gold foils for flexible electronics," *Science,* vol. 355, no. 6330, pp. 1203-1206, 2017.

[13] M. V. Kelso, J. Z. Tubbesing, Q. Chen, and J. A. Switzer, "Epitaxial electrodeposition of chiral metal surfaces on silicon (643)," *Journal of the American Chemical Society,* vol. 140, no. 46, pp. 15812-15819, 2018.

[14] J. A. Switzer, M. G. Shumsky, and E. W. Bohannan, "Electrodeposited ceramic single crystals," *Science,* vol. 284, no. 5412, pp. 293-296, 1999.

[15] J. A. Switzer, H. M. Kothari, P. Poizot, S. Nakanishi, and E. W. Bohannan, "Enantiospecific electrodeposition of a chiral catalyst," *Nature,* vol. 425, no. 6957, pp. 490-493, 2003.

[16] B. Völkel *et al.*, "Electrodeposition of copper and cobalt nanostructures using self-assembled monolayer templates," *Surface science,* vol. 597, no. 1-3, pp. 32-41, 2005.

[17] Z. She, A. DiFalco, G. Hähner, and M. Buck, "Electron-beam patterned self-assembled monolayers as templates for Cu electrodeposition and lift-off," *Beilstein Journal of Nanotechnology,* vol. 3, no. 1, pp. 101-113, 2012.

[18] J. A. Koza, J. C. Hill, A. C. Demster, and J. A. Switzer, "Epitaxial electrodeposition of methylammonium lead iodide perovskites," *Chemistry of Materials,* vol. 28, no. 1, pp. 399-405, 2016.

[19] R. Reske, H. Mistry, F. Behafarid, B. Roldan Cuenya, and P. Strasser, "Particle size effects in the catalytic electroreduction of $CO_2$ on Cu nanoparticles," *Journal of the American Chemical Society,* vol. 136, no. 19, pp. 6978-6986, 2014.

[20] A. Frisk, H. Ali, P. Svedlindh, K. Leifer, G. Andersson, and T. Nyberg, "Composition, structure and magnetic properties of ultra-thin Fe/Ni multilayers sputter deposited on epitaxial Cu/Si (001)," *Thin Solid Films,* vol. 646, pp. 117-125, 2018.

[21] N. Kashima *et al.*, "Development of Cu substrate for low cost coated conductors," *IEEE transactions on applied superconductivity,* vol. 19, no. 3, pp. 3299-3302, 2009.

[22] B. A. Nejand, P. Nazari, S. Gharibzadeh, V. Ahmadi, and A. Moshaii, "All-inorganic large-area low-cost and durable flexible perovskite solar cells using copper foil as a substrate," *Chemical Communications,* vol. 53, no. 4, pp. 747-750, 2017.

[23] J. Sun *et al.*, "Piezo-phototronic effect improved performance of n-ZnO nano-arrays/p-$Cu_2O$ film based pressure sensor synthesized on flexible Cu foil," *Nano Energy,* vol. 32, pp. 96-104, 2017.

[24] C. Ramesh *et al.*, "Structural and optical properties of GaN film on copper and graphene/copper metal foils grown by laser molecular beam epitaxy," *Journal of Nanoscience and Nanotechnology,* vol. 20, no. 6, pp. 3929-3934, 2020.

[25] R. Iwanowski and D. Trivih, "Cu/$Cu_2O$ Schottky barrier solar cells prepared by multistep irradiation of a $Cu_2O$ substrate by H+ ions," *Solar Cells,* vol. 13, no. 3, pp. 253-264, 1985.

[26] P. Prod'Homme, F. Maroun, R. Cortes, and P. Allongue, "Electrochemical growth of ultraflat Au (111) epitaxial buffer layers on H–Si (111)," *Applied Physics Letters,* vol. 93, no. 17, p. 171901, 2008.

[27] W. Yang, J. J. Gooding, and D. B. Hibbert, "Characterisation of gold electrodes modified with self-assembled monolayers of L-cysteine for the adsorptive stripping analysis of copper," *Journal of Electroanalytical Chemistry,* vol. 516, no. 1-2, pp. 10-16, 2001.

[28] M. Matsunaga, T. Nakanishi, T. Asahi, and T. Osaka, "Effect of surface coverage of gold (111) electrode with cysteine on the chiral discrimination of DOPA," *Chirality: The Pharmacological, Biological, and Chemical Consequences of Molecular Asymmetry,* vol. 19, no. 4, pp. 295-299, 2007.

[29] D. M. Arrigan, "A study of L-cysteine adsorption on gold via electrochemical desorption and copper (II) ion complexation," *Analyst,* vol. 124, no. 11, pp. 1645-1649, 1999.

[30] J. Sondag-Huethorst, H. Van Helleputte, and L. Fokkink, "Generation of electrochemically deposited metal patterns by means of electron beam (nano) lithography of self-assembled monolayer resists," *Applied Physics Letters,* vol. 64, no. 3, pp. 285-287, 1994.

[31] P. Schilardi, O. Azzaroni, and R. Salvarezza, "A novel application of alkanethiol self-assembled monolayers in nanofabrication: Direct molding and replication of patterned conducting masters," *Langmuir,* vol. 17, no. 9, pp. 2748-2752, 2001.

[32] N. S. Pesika, A. Radisic, K. J. Stebe, and P. C. Searson, "Fabrication of complex architectures using electrodeposition into patterned self-assembled monolayers," *Nano Letters,* vol. 6, no. 5, pp. 1023-1026, 2006.

[33] T. Baunach *et al.*, "A New Approach to the Electrochemical Metallization of Organic Monolayers: Palladium Deposition onto a 4, 4′-Dithiodipyridine Self-Assembled Monolayer," *Advanced Materials,* vol. 16, no. 22, pp. 2024-2028, 2004.

[34] Z. She *et al.*, "Coordination controlled electrodeposition and patterning of layers of palladium/copper nanoparticles on top of a self-assembled monolayer," *Nanoscale,* vol. 11, no. 29, pp. 13773-13782, 2019.

[35] A.-C. Liu, D.-c. Chen, C.-C. Lin, H.-H. Chou, and C.-h. Chen, "Application of cysteine monolayers for electrochemical determination of sub-ppb copper (II)," *Analytical Chemistry,* vol. 71, no. 8, pp. 1549-1552, 1999.

[36] M. Nishizawa, T. Sunagawa, and H. Yoneyama, "Underpotential deposition of copper on gold electrodes through self-assembled monolayers of propanethiol," *Langmuir,* vol. 13, no. 20, pp. 5215-5217, 1997.

[37] K. D. Truong and P. A. Rowntree, "Formation of self-assembled butanethiol monolayers on au substrates: Spectroscopic evidence for highly ordered island formation in sub-monolayer films," *The Journal of Physical Chemistry,* vol. 100, no. 51, pp. 19917-19926, 1996.

[38] R. Yamada, H. Wano, and K. Uosaki, "Effect of temperature on structure of the self-assembled monolayer of decanethiol on Au (111) surface," *Langmuir,* vol. 16, no. 13, pp. 5523-5525, 2000.

[39] C. Vericat, M. Vela, and R. Salvarezza, "Self-assembled monolayers of alkanethiols on Au (111): surface structures, defects and dynamics," *Physical Chemistry Chemical Physics,* vol. 7, no. 18, pp. 3258-3268, 2005.

[40] Y. Wang, Q. Chi, N. S. Hush, J. R. Reimers, J. Zhang, and J. Ulstrup, "Gold mining by alkanethiol radicals: vacancies and pits in the self-assembled monolayers of 1-propanethiol and 1-butanethiol on Au (111)," *The Journal of Physical Chemistry C,* vol. 115, no. 21, pp. 10630-10639, 2011.

[41] J. Yan *et al.*, "Controlling the stereochemistry and regularity of butanethiol self-assembled monolayers on Au (111)," *Journal of the American Chemical Society,* vol. 136, no. 49, pp. 17087-17094, 2014.

[42] A. Kühnle, T. R. Linderoth, M. Schunack, and F. Besenbacher, "L-cysteine adsorption structures on Au (111) investigated by scanning tunneling microscopy under ultrahigh vacuum conditions," *Langmuir,* vol. 22, no. 5, pp. 2156-2160, 2006.

[43] A. Dakkouri, D. Kolb, R. Edelstein-Shima, and D. Mandler, "Scanning tunneling microscopy study of L-cysteine on Au (111)," *Langmuir,* vol. 12, no. 11, pp. 2849-2852, 1996.

[44] J. Zhang, Q. Chi, J. U. Nielsen, E. P. Friis, J. E. Andersen, and J. Ulstrup, "Two-dimensional cysteine and cystine cluster networks on Au (111) disclosed by voltammetry and in situ scanning tunneling microscopy," *Langmuir,* vol. 16, no. 18, pp. 7229-7237, 2000.

[45] Q.-M. Xu, L.-J. Wan, C. Wang, C.-L. Bai, Z.-Y. Wang, and T. Nozawa, "New structure of L-cysteine self-assembled monolayer on Au (111): Studies by in situ scanning tunneling microscopy," *Langmuir,* vol. 17, no. 20, pp. 6203-6206, 2001.

[46] C. M. Hull and J. A. Switzer, "Electrodeposited epitaxial Cu (100) on Si (100) and lift-off of single crystal-like Cu (100) foils," *ACS applied materials & interfaces,* vol. 10, no. 44, pp. 38596-38602, 2018.

[47] C. Yang, M. Kneiß, F.-L. Schein, M. Lorenz, and M. Grundmann, "Room-temperature domain-epitaxy of copper iodide thin films for transparent CuI/ZnO heterojunctions with high rectification ratios larger than 109," *Scientific reports,* vol. 6, no. 1, p. 21937, 2016.

# SECTION

# 2. CONCLUSIONS & FUTURE WORK

## 2.1. CONCLUSIONS

Epitaxial electrodeposition is a simple and powerful soft-solution method to produce in-plane and out-of-plane ordered thin films. Epitaxial semiconductors and metals exhibit superior performance in a variety of electronic devices. Wide bandgap p-type semiconductors have attracted significant attention in optoelectronics such as perovskite solar cells, transparent electrodes, thin film transistors, short wavelength LEDs and UV photodetectors. Epitaxial electrodeposition is shown to be useful to produce some wide bandgap semiconductors including CuSCN and cuprous halides. An epitaxial copper thin film was also electrodeposited on L-cysteine self-assembled monolayer modified Au(111) surface and lifted-off as a low-cost flexible single-crystal-like metal substrate for flexible electronic devices.

Paper I introduces an electrochemical method for depositing epitaxial hole transporting CuSCN nanorods with a [001] orientation on the Au(111) surface. Epitaxial CuSCN grows with a high degree of in-plane as well as out-of-plane order with +0.22% coincidence site lattice mismatch on Au(111). An epitaxial CuSCN/Au structure forms an ideal HTM/metal system. To study the electronic properties of the obtained epitaxial CuSCN, a Au/epitaxial CuSCN/Ag heterojunction has a diode quality factor of 1.4,

whereas a diode produced with polycrystalline CuSCN has a diode quality factor of 2.1. A highly ordered and transparent CuSCN foil was produced by epitaxial lift-off following a triiodide etch of the thin Au layer. The 400 nm thick CuSCN foil had an average 94% transmittance in the visible range and a 3.85 eV direct bandgap.

Paper II provides an electrochemical synthetic route for depositing epitaxial wide bandgap p-type cuprous halide CuBr thin films on two different orientations of Ag surfaces. Epitaxial films of CuBr(111) and CuBr(100) are successfully deposited. A plausible mechanism is proposed to explain the nucleation and growth of the epitaxial CuBr thin films. We found that the formation of a AgBr buffer layer during the electrodeposition process is essential for the deposition of epitaxial CuBr. The CuBr(100) and AgBr(100) buffer layer exhibit an in-plane rotation of 45° compared to the Ag(100) substrate which could significantly reduce the lattice mismatch from +39.5% for an unrotated film to -1.4% for a 45° rotated film.

Paper III presents the epitaxial electrodeposition of Cu films on a L-cysteine self-assembled monolayer modified Au(111) surface. Cu follows the out-of-plane and in-plane orientation of Au(111) with a small amount of twinned [511] orientation. Possible deposition mechanisms are explained. Cu on L-cysteine SAM grows epitaxially, whereas Cu on 1-butanethiol SAM yields a polycrystalline structure. The Cu(111) foil could be easily lifted off without etching agents to serve as a low-cost highly ordered metal substrate. The Cu(111) foil exhibits a low resistivity of $3.75 \times 10^{-8}$ Ω.m and good bending stability.

Only a 12% resistance increase was found after $10^4$ bending cycles. To explore the potential of this Cu foil for flexible electronic devices, we achieved epitaxial $Cu_2O$ on the surface of the Cu(111) foil as a potential flexible solar cell structure.

## 2.2. FUTURE WORK

More future work will be focused on low-mismatched CuCl(111) on Si(111), p-$Co(OH)_2$/n-Si(111) photoanode and epitaxial Prussian blue (220) on Au(100).

**2.2.1. Epitaxial Electrodeposition of Low-Mismatched CuCl(111) on Si(111).** Due to wide bandgap (3.4 eV), large exciton binding energy (190 meV), negligible built-in field, and close lattice matched (mismatch -0.18%) to silicon substrates, γ-CuCl with zincblende structure has drawn attention for highly efficient LEDs compatible to Si technology. Since Si processes are mature in the semiconductor industry and the photovoltaic industry, CuCl/Si could be a potential candidate for low-cost blue LED structure. Electrodeposition for producing epitaxial CuCl on Si still remains a challenge. Polycrystalline or textured CuCl films could result in electron-hole recombination at the grain boundaries. The proposed work for epitaxial CuCl(111)/Si(111) includes:

1. Design the electrochemical bath and conditions for epitaxial deposition of CuCl.

2. Achieve the epitaxial growth of CuCl(111) on Si(111) and analyze the growth mechanism since Si surface is easy to be oxidized to be $SiO_x$.

3. Explore the potential of CuCl/Si for blue-LED applications.

Preliminary work on CuCl(111)/Si(111) is shown in APPENDIX A.

**2.2.2. Electrodeposited Crystalline $Co(OH)_2$ Nanosheets on N-Si(111) for Photoelectrochemical Water Splitting.** Photoelectrochemical water splitting into oxygen and hydrogen is a sustainable strategy for converting solar energy into fuels. Silicon photoanode for photoelectrochemical water splitting is one of the most intriguing methods because of high efficiency, low cost and commercialization potential. Various transition-metals and semiconductors such as cobalt, nickel and iron have been well studied as oxygen catalysts. Our group previously reported an efficient n-Si/$SiO_x$/Co/CoOOH photoanode as a metal-insulator-semiconductor junction. Here, we plan to directly electrodeposit pure wide bandgap p-type $Co(OH)_2$ ($E_g$ = 2.85 eV) nanosheets on Si as an efficient catalyst as well as a hole-selective layer. Although some $Co(OH)_2$/Si photoanodes have been studied, $CoO_x$ and Co metal could co-deposit with $Co(OH)_2$, which may influence the water splitting performance. The proposed work includes:

1. Electrodeposit $Co(OH)_2$ on n-Si(111) by reduction of $[Co(en)_3]^{3+}$ in an alkaline electrolyte and analyze the deposits by XRD, SEM and TEM.

2. Study the photoelectrochemical water splitting performance of $Co(OH)_2$ nanosheets on n-Si(111).

3. Investigate the long-term stability of the water splitting device.

Preliminary work on $Co(OH)_2$ nanosheets on n-Si(111) photoelectrochemical water splitting is shown in APPENDIX B.

**2.2.3. Epitaxial Electrodeposition of Prussian Blue (220) on Au(100).** Prussian blue (PB), $Fe^{III}_4[Fe^{II}(CN)_6]_3$, and its analogues are a class of microporous metal-organic frameworks. They are interesting as active materials for battery materials especially post-lithium batteries such as sodium-ion batteries and potassium-ion batteries. Their open channels accommodate $Na^+$ and provide reversible and fast charging and discharging processes in aqueous solution. Their low cost and low-temperature synthesis make them promising for mass production as low-cost cathode materials. Epitaxial PB could have a potential to show better stability and have faster charging and discharging processes due to ordered channels. Our group previously reported epitaxial PB(111) on Au(110). Here, we plan to explore other orientations of epitaxial PB by electrodeposition. Different orientations of PB could be used to analyze the effect of the channel directions to the performance of this kind of cathode materials. The proposed work includes:

1. Electrodeposit epitaxial PB(220) on the Au(100) surface and analyze the epitaxy by XRD, SEM and TEM.

2. Compare the charge and discharge performance of <111> and <110> oriented PB thin films.

3. Develop other epitaxial PB analogues such as copper hexacyanoferrate (CuHCF), manganese hexacyanoferrate (MnHCF) and nickel hexacyanoferrate (NiHCF).

Preliminary work on epitaxial electrodeposition of Prussian blue (220) on Au(100) is shown in APPENDIX C.

# APPENDIX A.

## PRELIMINARY WORK ON EPITAXIAL ELECTRODEPOSITION OF LOW-MISMATCHED CUCl(111) ON Si(111)

Preliminary work has shown that CuCl(111) can be directly electrodeposited on a n-Si(111) surface from an electrochemical bath containing 100 mM $CuSO_4$ and 170 mM NaCl with Ar bubbled for 30 mins. The electrodeposition was performed at the constant potential of -0.2 V vs. Ag/AgCl at room temperature. Figure A.1 shows some X-ray analysis of CuCl(111)/Si(111). Figure A.1A shows the XRD of CuCl(111)/Si(111) where CuCl(111) and Si(111) are highly overlapped. In the enlarged XRD patterns as shown in Figure A.1B, we found that the (111), (222), (333) peaks of CuCl and Si have 0.18, 0.22, 0.32 degree differences, respectively. As shown in Figure A.1C and Figure A.1D, the in-plane orientation of CuCl(111) is confirmed by the (220) pole of CuCl(111) that six intense spots show up at a tilt angle of $\chi = 35.5°$, whereas the (220) pole of Si(111) only shows three spots at the same tilt angle.

More additional characterizations have been performed including azimuthal scans, rocking curves, interface models and SEM as shown in Figure A.2. Epitaxial relationships and perfection have been studied by using azimuthal scans and rocking curves. Figure A.2A shows azimuthal scans of CuCl(111) and Si(111) at $\chi = 35.5°$. We can see that CuCl(111) follows the in-plane orientation of the Si(111) substrate. Figure A.2B shows rocking curves for CuCl(111) and Si(111). CuCl(111) has a FWHM of 1.10 which is larger than that of Si(111) (FWHM: 0.06). One reason could be the mosaic spread during the epitaxial growth. Another reason could be that the ordered $SiO_x$ layer with less perfection is formed to serve as a template for the epitaxial growth of CuCl. The cross-sectional interface model (Figure

A.2C) and plan-view interface model (Figure A.2D) show the crystal structures of the closely matched CuCl(111)/Si(111). Figure A.2E shows a SEM image of the morphology of CuCl(111) on Si(111). Large triangular CuCl(111) crystals are observed in an ordered alignment. Figure A.2F shows the in-plane domain analysis of CuCl(111) on Si(111). We found that almost 80% of CuCl(111) crystals are antiparallel and 20% of CuCl(111) crystals are parallel with the in-plane orientation of the Si(111) substrate. Until now, we have only been able to produce ordered crystals instead of continuous films. In order to practically use this CuCl/Si structure for LEDs, investigation of growing continuous CuCl films will be needed in the future.

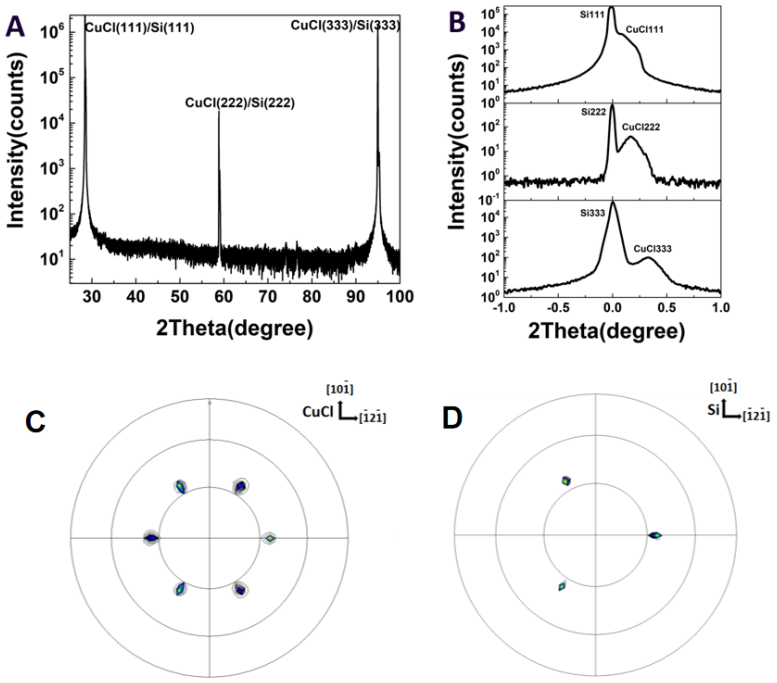


Figure A.1. XRD and pole figures of CuCl(111)/Si(111). (A) XRD of CuCl(111)/Si(111); (B) Enlarged view of {111} family peaks of CuCl(111) and Si(111); (C) (220) pole of CuCl(111); (D) (220) pole of Si(111).

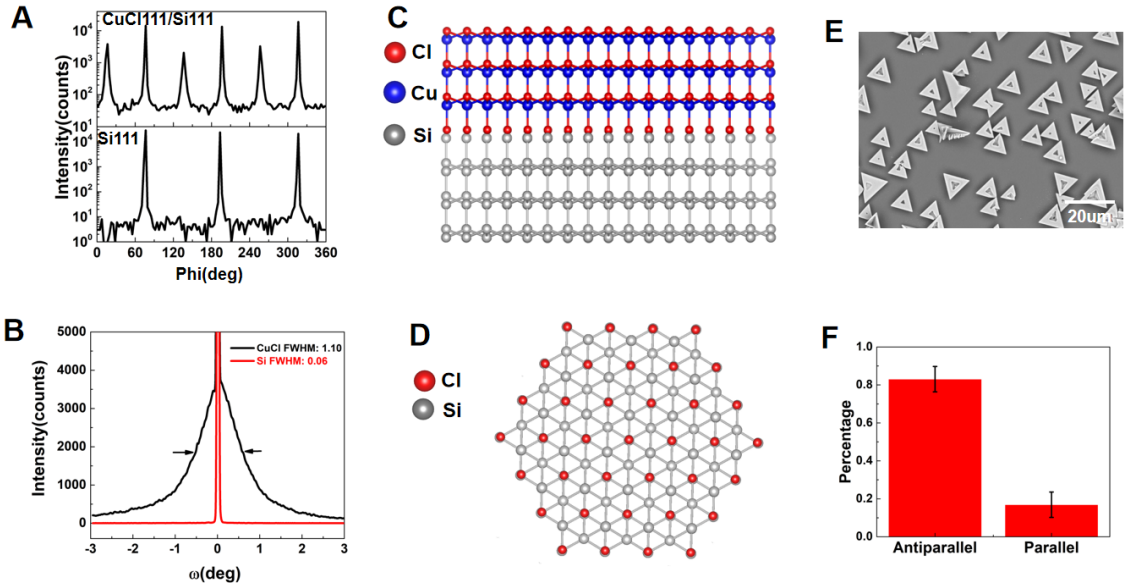


Figure A.2. Azimuthal scans, rocking curves, interface models and SEM of CuCl(111) on Si(111). (A) Azimuthal scans of CuCl(111) and Si(111) at $\chi = 35.5°$; (B) Rocking curves for CuCl(111) and Si(111); (C) Cross-sectional interface model of CuCl(111) on Si(111); (D) Plan-view interface model of CuCl(111) on Si(111); (E) SEM image of CuCl(111) triangular crystals on Si(111); (F) In-plane domain analysis of CuCl(111) on Si(111).

# APPENDIX B.

## PRELIMINARY WORK OF ELECTRODEPOSITED CRYSTALLINE $Co(OH)_2$ NANOSHEETS ON N-Si(111) FOR PHOTOELECTROCHEMICAL WATER SPLITTING

Preliminary work has shown that $Co(OH)_2$ nanosheets can be electrodeposited on n-Si(111) (Phosphorus-doped, 1-3 Ω.cm, Virginia Semiconductor) surface for efficient photoelectrochemical water oxidation. The electrochemical deposition bath contains 10 mM $[Co(en)_3Cl_3]$, 2 M NaOH. The electrodeposition was performed at the constant potential of -1 V vs. Ag/AgCl for 300 s at room temperature. $Co(OH)_2$ is a 2D p-type semiconductor with a rhombohedral structure and a wide bandgap of 2.85 eV. Figure B.1A shows the XRD of as-deposited $Co(OH)_2$ on n-Si(111). What we can observe is the {001} family of peaks of $Co(OH)_2$. Figure B.1B shows the (102) pole figure of $Co(OH)_2$ and no spots can be found which means that $Co(OH)_2$ is not epitaxial on n-Si(111). Figure B.1C exhibits the SEM image of $Co(OH)_2$ on n-Si(111). The uniform nanosheets morphology is favorable for oxygen evolving catalysis due to a large surface area. Photoelectrochemical water oxidation was conducted at a simulated sunlight in 1 M NaOH solution as shown in Figure B.1D. At +0.55 V vs. Ag/AgCl, this photoanode has a limiting current density of 36 $mA/cm^2$ under AM 1.5 irradiation (black line, 100 $mW/cm^2$) while no currents have been observed in the dark (red line). By analyzing the difference between $Co(OH)_2$/n-Si(111) under irradiation and $Co(OH)_2/n^{++}$-Si(111) (Degenerate, resistivity of 0.001 Ω.cm) in the dark, an open-circuit photovoltage of 500 mV and a short-circuit photocurrent of 36 $mA/cm^2$ have been observed. However, this photoanode still suffers from the corrosion of the basic solution which could only last a few hours for efficient photoelectrochemical water oxidation. So long-term stability study could be an important topic in the future.

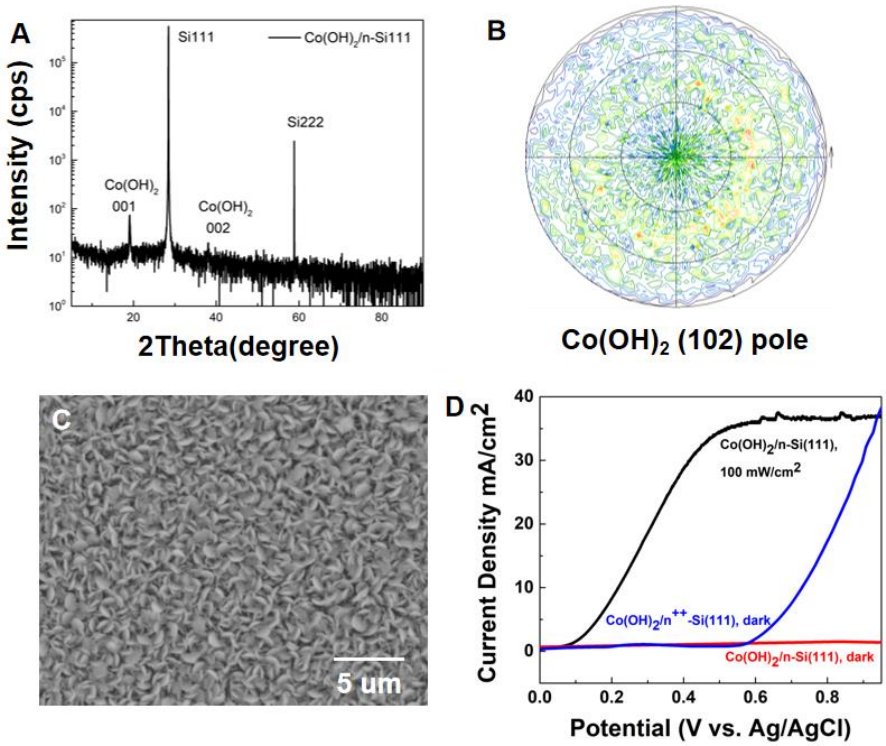


Figure B.1. XRD, pole figure, SEM and photoelectrochemical performance of electrodeposited $Co(OH)_2$ on n-Si(111). (A) XRD of $Co(OH)_2$/n-Si(111); (B) (102) of $Co(OH)_2$; (C) SEM image of $Co(OH)_2$ nanosheets on n-Si(111); (D) Linear sweep voltammetry comparing $Co(OH)_2$/n-Si in the dark (red), $Co(OH)_2/n^{++}$-Si(111) in the dark (blue) and $Co(OH)_2$/n-Si(111) under 100 mW.cm$^{-2}$ AM 1.5 irradiation (black) in 1 M NaOH at a 20 mV s$^{-1}$ scan rate.

# APPENDIX C.

## PRELIMINARY WORK OF EPITAXIAL ELECTRODEPOSITION OF PRUSSIAN BLUE (220) ON AU(100)

Preliminary work has shown that epitaxial PB(220) can be electrodeposited on Au(100) surface from an electrochemical bath containing 1 mM $K_3Fe(CN)_6$ and 1 mM $Fe(NO_3)_3$ in 0.5 M KCl with Ar bubbled during the deposition. The electrodeposition was performed at the constant potential of +0.3 V vs. Ag/AgCl at room temperature. Prussian blue has a cubic crystal structure at room temperature. Figure C.1A shows the XRD of PB(220) on Au(100). Only the {110} family of peaks is observed, indicating an out-of-plane order. Figure C.1B shows the (200) pole figure of PB(220). Four separated and intense main spots are observed at a tilt angle of $\chi = 45°$, consistent with the angle between the [100] and [110] directions in a cubic system. The other 12 spots belong to a small amount of [311] twinning. Figure C.1C and Figure C.1D show SEM images of PB(220) with a 30,000x magnification and 20,000x magnification, respectively. Ordered crystals of PB confirm that PB(220) is indeed epitaxial on Au(100).

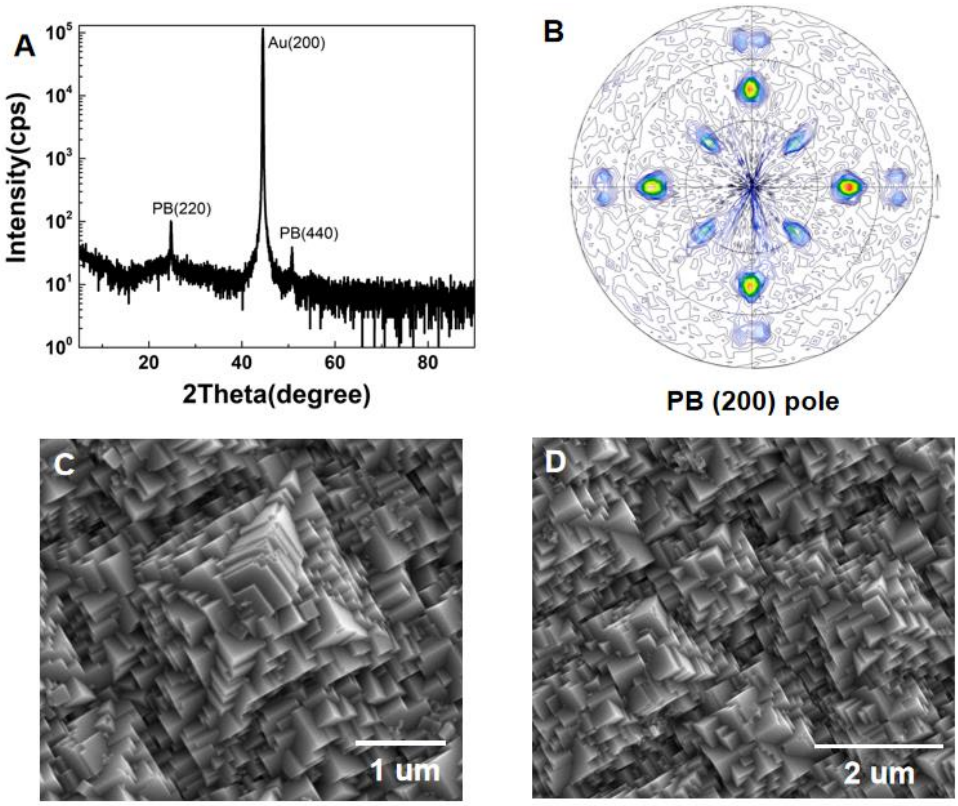


Figure C.1. XRD, pole figure and SEM images of PB(220) on Au(100). (A) XRD of PB(220)/Au(100); (B) (200) pole of PB(220); (C) SEM of PB(220) with a 30,000x magnification; (D) SEM of PB(220) with a 20,000x magnification.

# BIBLIOGRAPHY


[1] L. Fabbrizzi, "Strange case of Signor Volta and Mister Nicholson: how electrochemistry developed as a consequence of an editorial misconduct," *Angewandte Chemie International Edition,* vol. 58, no. 18, pp. 5810-5822, 2019.

[2] F. Xiao, C. Hangarter, B. Yoo, Y. Rheem, K.-H. Lee, and N. V. Myung, "Recent progress in electrodeposition of thermoelectric thin films and nanostructures," *Electrochimica Acta,* vol. 53, no. 28, pp. 8103-8117, 2008.

[3] T. Yoshida *et al.*, "Electrodeposition of inorganic/organic hybrid thin films," *Advanced Functional Materials,* vol. 19, no. 1, pp. 17-43, 2009.

[4] F. Baizeng, L. Xinyu, W. Xindong, and D. Shuzhen, "Surface modification of a MCFC anode by electrodeposition of niobium," *Journal of Electroanalytical Chemistry,* vol. 441, no. 1-2, pp. 1-3, 1998.

[5] Y. Zhang, L. Zhang, and C. Zhou, "Review of chemical vapor deposition of graphene and related applications," *Accounts of chemical research,* vol. 46, no. 10, pp. 2329-2339, 2013.

[6] A. Y. Cho and J. Arthur, "Molecular beam epitaxy," *Progress in solid state chemistry,* vol. 10, pp. 157-191, 1975.

[7] P. Nair *et al.*, "Semiconductor thin films by chemical bath deposition for solar energy related applications," *Solar Energy Materials and solar cells,* vol. 52, no. 3-4, pp. 313-344, 1998.

[8] L. Scriven, "Physics and applications of dip coating and spin coating," *MRS Online Proceedings Library (OPL),* vol. 121, p. 717, 1988.

[9] D. M. Mattox, "Physical vapor deposition (PVD) processes," *Metal Finishing,* vol. 100, pp. 394-408, 2002.

[10] S. M. George, "Atomic layer deposition: an overview," *Chemical reviews,* vol. 110, no. 1, pp. 111-131, 2010.

[11] B. Thirumalraj *et al.*, "Nucleation and growth mechanism of lithium metal electroplating," *Journal of the American Chemical Society,* vol. 141, no. 46, pp. 18612-18623, 2019.

[12] B. Yoo, S. Hernandez, D.-Y. Park, and N. Myung, "Electrodeposition of FeCoNi thin films for magnetic-MEMS devices," *Electrochimica Acta,* vol. 51, no. 28, pp. 6346-6352, 2006.

[13] S. K. Seol, D. Kim, S. Lee, J. H. Kim, W. S. Chang, and J. T. Kim, "Electrodeposition-based 3D printing of metallic microarchitectures with controlled internal structures," *Small,* vol. 11, no. 32, pp. 3896-3902, 2015.

[14] D. Lincot, "Electrodeposition of semiconductors," *Thin solid films,* vol. 487, no. 1-2, pp. 40-48, 2005.

[15] J. Kois *et al.*, "Electrodeposition of Cu–In–Ga thin metal films for Cu (In, Ga) $Se_2$ based solar cells," *Thin Solid Films,* vol. 516, no. 18, pp. 5948-5952, 2008.

[16] I. Zhitomirsky, "Ceramic films using cathodic electrodeposition," *JOM-e,* vol. 52, no. 1, pp. 1019745774-24607, 2000.

[17] N. Fujita, S. Maeda, S. Yoshida, M. Takase, M. Nakano, and H. Fukunaga, "Preparation of Co–Pt alloy film magnets by electrodeposition," *Journal of Magnetism and Magnetic Materials,* vol. 272, pp. E1895-E1897, 2004.

[18] S. Alizadeh and D. Nematollahi, "Convergent and divergent paired electrodeposition of metal-organic framework thin films," *Scientific Reports,* vol. 9, no. 1, p. 14325, 2019.

[19] R. Ahmed, Q. Lin, Y. Xu, and G. Zangari, "Growth, morphology and crystal structure of electrodeposited $Bi_2Se_3$ films: Influence of the substrate," *Electrochimica Acta,* vol. 299, pp. 654-662, 2019.

[20] H. Yamamuro, N. Hatsuta, M. Wachi, Y. Takei, and M. Takashiri, "Combination of electrodeposition and transfer processes for flexible thin-film thermoelectric generators," *Coatings,* vol. 8, no. 1, p. 22, 2018.

[21] J. Mallett *et al.*, "Compositional control in electrodeposition of FePt films," *Electrochemical and solid-state letters,* vol. 7, no. 10, p. C121, 2004.

[22] E. B. Svedberg, J. J. Mallett, S. Sayan, A. J. Shapiro, W. F. Egelhoff Jr, and T. Moffat, "Recrystallization texture, epitaxy, and magnetic properties of electrodeposited FePt on Cu (001)," *Applied physics letters,* vol. 85, no. 8, pp. 1353-1355, 2004.

[23] M. Sheffer, A. Groysman, and D. Mandler, "Electrodeposition of sol–gel films on Al for corrosion protection," *Corrosion Science,* vol. 45, no. 12, pp. 2893-2904, 2003.

[24] N. K. Mahenderkar, Y.-C. Liu, J. A. Koza, and J. A. Switzer, "Electrodeposited germanium nanowires," *ACS nano,* vol. 8, no. 9, pp. 9524-9530, 2014.

[25] R. Liu, F. Oba, E. W. Bohannan, F. Ernst, and J. A. Switzer, "Shape control in epitaxial electrodeposition: $Cu_2O$ nanocubes on InP (001)," *Chemistry of materials,* vol. 15, no. 26, pp. 4882-4885, 2003.

[26] E. A. Kulp and J. A. Switzer, "Electrochemical biomineralization: The deposition of calcite with chiral morphologies," *Journal of the American Chemical Society,* vol. 129, no. 49, pp. 15120-15121, 2007.

[27] M. V. Kelso, J. Z. Tubbesing, Q. Chen, and J. A. Switzer, "Epitaxial electrodeposition of chiral metal surfaces on silicon (643)," *Journal of the American Chemical Society,* vol. 140, no. 46, pp. 15812-15819, 2018.

[28] N. Pangarov, "The crystal orientation of electrodeposited metals," *Electrochimica Acta,* vol. 7, no. 1, pp. 139-146, 1962.

[29] Y. Liu, D. Gokcen, U. Bertocci, and T. P. Moffat, "Self-terminating growth of platinum films by electrochemical deposition," *Science,* vol. 338, no. 6112, pp. 1327-1330, 2012.

[30] J. A. Harrington, "Single-crystal fiber optics: a review," *Solid State Lasers XXIII: Technology and Devices,* vol. 8959, p. 895902, 2014.

[31] H. Jiang and W. Hu, "The emergence of organic single-crystal electronics," *Angewandte Chemie International Edition,* vol. 59, no. 4, pp. 1408-1428, 2020.

[32] D.-Y. Khang, H. Jiang, Y. Huang, and J. A. Rogers, "A stretchable form of single-crystal silicon for high-performance electronics on rubber substrates," *Science,* vol. 311, no. 5758, pp. 208-212, 2006.

[33] N. R. E. Laboratory, "Best research-cell efficiencies," ed: NREL Golden, CO, 2018.

[34] D. Shi *et al.*, "Low trap-state density and long carrier diffusion in organolead trihalide perovskite single crystals," *Science,* vol. 347, no. 6221, pp. 519-522, 2015.

[35] C. Yang, M. Kneiß, F.-L. Schein, M. Lorenz, and M. Grundmann, "Room-temperature domain-epitaxy of copper iodide thin films for transparent CuI/ZnO heterojunctions with high rectification ratios larger than 109," *Scientific reports,* vol. 6, no. 1, p. 21937, 2016.

[36] X. Xiang, Y. Xu, X. Fei, and B. Li, "A multi-wafers LPE technique for $Al_xGa_{1-x}As$/GaAs heterojunction solar cells," *Solar energy materials and solar cells,* vol. 35, pp. 69-74, 1994.

[37] J. Kim *et al.*, "Principle of direct van der Waals epitaxy of single-crystalline films on epitaxial graphene," *Nature communications,* vol. 5, no. 1, pp. 1-7, 2014.

[38] K.-C. Kim *et al.*, "Free-electron creation at the 60 twin boundary in $Bi_2Te_3$," *Nature communications,* vol. 7, no. 1, p. 12449, 2016.

[39] Q. L. He *et al.*, "Two-dimensional superconductivity at the interface of a Bi2Te3/FeTe heterostructure," *Nature communications,* vol. 5, no. 1, p. 4247, 2014.

[40] M. P. Nikiforov, A. A. Vertegel, M. G. Shumsky, and J. A. Switzer, "Epitaxial Electrodeposition of Fe3O4 on Single-Crystal Au (111)," *Advanced Materials,* vol. 12, no. 18, pp. 1351-1353, 2000.

[41] G. Mu, R. V. Gudavarthy, E. A. Kulp, and J. A. Switzer, "Tilted epitaxial ZnO nanospears on Si (001) by chemical bath deposition," *Chemistry of Materials,* vol. 21, no. 17, pp. 3960-3964, 2009.

[42] M. V. Kelso, N. K. Mahenderkar, Q. Chen, J. Z. Tubbesing, and J. A. Switzer, "Spin coating epitaxial films," *Science,* vol. 364, no. 6436, pp. 166-169, 2019.

[43] J. A. Switzer, M. G. Shumsky, and E. W. Bohannan, "Electrodeposited ceramic single crystals," *Science,* vol. 284, no. 5412, pp. 293-296, 1999.

[44] E. W. Bohannan, M. G. Shumsky, and J. A. Switzer, "Epitaxial electrodeposition of copper (I) oxide on single-crystal gold (100)," *Chemistry of materials,* vol. 11, no. 9, pp. 2289-2291, 1999.

[45] S. Nakanishi, G. Lu, H. M. Kothari, E. W. Bohannan, and J. A. Switzer, "Epitaxial electrodeposition of prussian blue thin films on single-crystal Au (110)," *Journal of the American Chemical Society,* vol. 125, no. 49, pp. 14998-14999, 2003.

[46] J. A. Koza, J. C. Hill, A. C. Demster, and J. A. Switzer, "Epitaxial electrodeposition of methylammonium lead iodide perovskites," *Chemistry of Materials,* vol. 28, no. 1, pp. 399-405, 2016.

[47] J. C. Hill, J. A. Koza, and J. A. Switzer, "Electrodeposition of epitaxial lead iodide and conversion to textured methylammonium lead iodide perovskite," *ACS Applied Materials & Interfaces,* vol. 7, no. 47, pp. 26012-26016, 2015.

[48] C. M. Hull and J. A. Switzer, "Electrodeposited epitaxial Cu (100) on Si (100) and lift-off of single crystal-like Cu (100) foils," *ACS applied materials & interfaces,* vol. 10, no. 44, pp. 38596-38602, 2018.

[49] Q. Chen and J. A. Switzer, "Electrodeposition of nanometer-thick epitaxial films of silver onto single-crystal silicon wafers," *Journal of Materials Chemistry C,* vol. 7, no. 6, pp. 1720-1725, 2019.

[50] N. K. Mahenderkar *et al.*, "Epitaxial lift-off of electrodeposited single-crystal gold foils for flexible electronics," *Science,* vol. 355, no. 6330, pp. 1203-1206, 2017.

[51] J. A. Switzer, J. C. Hill, N. K. Mahenderkar, and Y.-C. Liu, "Nanometer-thick gold on silicon as a proxy for single-crystal gold for the electrodeposition of epitaxial cuprous oxide thin films," *ACS applied materials & interfaces,* vol. 8, no. 24, pp. 15828-15837, 2016.

[52] A. Banik, E. W. Bohannan, and J. A. Switzer, "Epitaxial electrodeposition of bii3 and topotactic conversion to highly ordered solar light-absorbing perovskite (CH3NH3) 3Bi2I9," *Chemistry of Materials,* vol. 32, no. 19, pp. 8367-8372, 2020.

[53] M. A. VanHove, W. H. Weinberg, and C.-M. Chan, *Low-energy electron diffraction: experiment, theory and surface structure determination*. Springer Science & Business Media, 2012.

[54] M. Kim, J.-H. Seo, U. Singisetti, and Z. Ma, "Recent advances in free-standing single crystalline wide band-gap semiconductors and their applications: GaN, SiC, ZnO, β-Ga 2 O 3, and diamond," *Journal of Materials Chemistry C,* vol. 5, no. 33, pp. 8338-8354, 2017.

[55] M. Mastellone *et al.*, "LIPSS applied to wide bandgap semiconductors and dielectrics: Assessment and future perspectives," *Materials,* vol. 15, no. 4, p. 1378, 2022.

[56] E. M. Fortunato *et al.*, "Wide-bandgap high-mobility ZnO thin-film transistors produced at room temperature," *Applied Physics Letters,* vol. 85, no. 13, pp. 2541-2543, 2004.

[57] Z. Li *et al.*, "Wide-bandgap perovskite/gallium arsenide tandem solar cells," *Advanced Energy Materials,* vol. 10, no. 6, p. 1903085, 2020.

[58] J. H. Park, D. Y. Kim, E. F. Schubert, J. Cho, and J. K. Kim, "Fundamental limitations of wide-bandgap semiconductors for light-emitting diodes," *ACS Energy Letters,* vol. 3, no. 3, pp. 655-662, 2018.

[59] G. Iannaccone, C. Sbrana, I. Morelli, and S. Strangio, "Power electronics based on wide-bandgap semiconductors: Opportunities and challenges," *IEEE Access,* vol. 9, pp. 139446-139456, 2021.

[60] J. W. Park, B. H. Kang, and H. J. Kim, "A review of low-temperature solution-processed metal oxide thin-film transistors for flexible electronics," *Advanced Functional Materials,* vol. 30, no. 20, p. 1904632, 2020.

[61] S. Pearton *et al.*, "Wide bandgap GaN-based semiconductors for spintronics," *Journal of Physics: Condensed Matter,* vol. 16, no. 7, p. R209, 2004.

[62] E. McGlynn, M. O. Henry, and J.-P. Mosnier, "ZnO wide-bandgap semiconductor nanostructures: Growth, characterization and applications," 2010.

[63] A. Khan, F. Rahman, R. Nongjai, and K. Asokan, "Structural, optical and electrical transport properties of Sn doped In2O3," *Solid State Sciences,* vol. 109, p. 106436, 2020.

[64] H. Hosono, "How we made the IGZO transistor," *Nature Electronics,* vol. 1, no. 7, pp. 428-428, 2018.

[65] W. Cao, J. Li, H. Chen, and J. Xue, "Transparent electrodes for organic optoelectronic devices: a review," *Journal of Photonics for energy,* vol. 4, no. 1, pp. 040990-040990, 2014.

[66] M. Usman, M. Munsif, U. Mushtaq, A.-R. Anwar, and N. Muhammad, "Green gap in GaN-based light-emitting diodes: in perspective," *Critical Reviews in Solid State and Materials Sciences,* vol. 46, no. 5, pp. 450-467, 2021.

[67] K. Liu, M. Sakurai, and M. Aono, "ZnO-based ultraviolet photodetectors," *Sensors,* vol. 10, no. 9, pp. 8604-8634, 2010.

[68] C.-H. Lin, C.-H. Liao, W.-H. Chen, C.-Y. Chou, and C.-Y. Liu, "Fabrication of p-type $TiO_2$ and transparent p-$TiO_2$/n-ITO pn junctions," *AIP Advances,* vol. 9, no. 4, p. 045229, 2019.

[69] J. Bullock *et al.*, "Efficient silicon solar cells with dopant-free asymmetric heterocontacts," *Nature Energy,* vol. 1, no. 3, pp. 1-7, 2016.

[70] L. Calió, S. Kazim, M. Grätzel, and S. Ahmad, "Hole-transport materials for perovskite solar cells," *Angewandte Chemie International Edition,* vol. 55, no. 47, pp. 14522-14545, 2016.

[71] S. Feng *et al.*, "Graphene/p-AlGaN/p-GaN electron tunnelling light emitting diodes with high external quantum efficiency," *Nano Energy,* vol. 60, pp. 836-840, 2019.

[72] Q. Dong *et al.*, "Electron-hole diffusion lengths> 175 μm in solution-grown $CH_3NH_3PbI_3$ single crystals," *Science,* vol. 347, no. 6225, pp. 967-970, 2015.

[73] H. Shen *et al.*, "In situ recombination junction between p-Si and $TiO_2$ enables high-efficiency monolithic perovskite/Si tandem cells," *Science advances,* vol. 4, no. 12, p. eaau9711, 2018.

[74] Y. Nanishi, "The birth of the blue LED," *Nature Photonics,* vol. 8, no. 12, pp. 884-886, 2014.

[75] M. Kneissl, T.-Y. Seong, J. Han, and H. Amano, "The emergence and prospects of deep-ultraviolet light-emitting diode technologies," *nature photonics,* vol. 13, no. 4, pp. 233-244, 2019.

[76] N. E. Courtier, J. M. Cave, J. M. Foster, A. B. Walker, and G. Richardson, "How transport layer properties affect perovskite solar cell performance: insights from a coupled charge transport/ion migration model," *Energy & Environmental Science,* vol. 12, no. 1, pp. 396-409, 2019.

[77] J. Burschka *et al.*, "Sequential deposition as a route to high-performance perovskite-sensitized solar cells," *Nature,* vol. 499, no. 7458, pp. 316-319, 2013.

[78] H. Xu, F. Yuan, D. Zhou, X. Liao, L. Chen, and Y. Chen, "Hole transport layers for organic solar cells: Recent progress and prospects," *Journal of materials chemistry A,* vol. 8, no. 23, pp. 11478-11492, 2020.

[79] T. Matsushima *et al.*, "High performance from extraordinarily thick organic light-emitting diodes," *Nature,* vol. 572, no. 7770, pp. 502-506, 2019.

[80] Y. Rong *et al.*, "Challenges for commercializing perovskite solar cells," *Science,* vol. 361, no. 6408, p. eaat8235, 2018.

[81] J.-P. Correa-Baena *et al.*, "Promises and challenges of perovskite solar cells," *Science,* vol. 358, no. 6364, pp. 739-744, 2017.

[82] L. Cavalcante *et al.*, "Synthesis, structural refinement and optical behavior of $CaTiO_3$ powders: A comparative study of processing in different furnaces," *Chemical Engineering Journal,* vol. 143, no. 1-3, pp. 299-307, 2008.

[83] J. Li *et al.*, "20.8% slot-die coated $MAPbI_3$ perovskite solar cells by optimal DMSO-content and age of 2-ME based precursor inks," *Advanced Energy Materials,* vol. 11, no. 10, p. 2003460, 2021.

[84] H. Zhang *et al.*, "Multifunctional crosslinking-enabled strain-regulating crystallization for stable, efficient α-$FAPbI_3$-based perovskite solar cells," *Advanced Materials,* vol. 33, no. 29, p. 2008487, 2021.

[85] S. Gharibzadeh *et al.*, "2D/3D heterostructure for semitransparent perovskite solar cells with engineered bandgap enables efficiencies exceeding 25% in four-terminal tandems with silicon and CIGS," *Advanced Functional Materials,* vol. 30, no. 19, p. 1909919, 2020.

[86] J. Y. Kim, J.-W. Lee, H. S. Jung, H. Shin, and N.-G. Park, "High-efficiency perovskite solar cells," *Chemical Reviews,* vol. 120, no. 15, pp. 7867-7918, 2020.

[87] A. K. Jena, A. Kulkarni, and T. Miyasaka, "Halide perovskite photovoltaics: background, status, and future prospects," *Chemical reviews,* vol. 119, no. 5, pp. 3036-3103, 2019.

[88] C. Liu *et al.*, "Highly Stable and Efficient Perovskite Solar Cells with 22.0% Efficiency Based on Inorganic–Organic Dopant-Free Double Hole Transporting Layers," *Advanced Functional Materials,* vol. 30, no. 28, p. 1908462, 2020.

[89] D. Zhao, M. Sexton, H. Y. Park, G. Baure, J. C. Nino, and F. So, "High-efficiency solution-processed planar perovskite solar cells with a polymer hole transport layer," *Advanced Energy Materials,* vol. 5, no. 6, p. 1401855, 2015.

[90] Z. Hawash, L. K. Ono, and Y. Qi, "Recent advances in spiro-MeOTAD hole transport material and its applications in organic–inorganic halide perovskite solar cells," *Advanced Materials Interfaces,* vol. 5, no. 1, p. 1700623, 2018.

[91] C. Zuo and L. Ding, "Modified PEDOT layer makes a 1.52 V Voc for perovskite/PCBM solar cells," *Advanced Energy Materials,* vol. 7, no. 2, p. 1601193, 2017.

[92] Z. Yu and L. Sun, "Inorganic hole-transporting materials for perovskite solar cells," *Small Methods,* vol. 2, no. 2, p. 1700280, 2018.

[93] A. S. Subbiah, A. Halder, S. Ghosh, N. Mahuli, G. Hodes, and S. K. Sarkar, "Inorganic hole conducting layers for perovskite-based solar cells," *The journal of physical chemistry letters,* vol. 5, no. 10, pp. 1748-1753, 2014.

[94] Z.-L. Tseng, L.-C. Chen, C.-H. Chiang, S.-H. Chang, C.-C. Chen, and C.-G. Wu, "Efficient inverted-type perovskite solar cells using UV-ozone treated $MoO_x$ and $WO_x$ as hole transporting layers," *Solar Energy,* vol. 139, pp. 484-488, 2016.

[95] A. Huang *et al.*, "Enhanced electrical property of Ni-doped $CoO_x$ hole transport layer for inverted perovskite solar cells," *Nanotechnology,* vol. 28, no. 20, p. 20LT02, 2017.

[96] S. Sajid *et al.*, "Breakthroughs in $NiO_x$-HTMs towards stable, low-cost and efficient perovskite solar cells," *Nano Energy,* vol. 51, pp. 408-424, 2018.

[97] V. E. Madhavan *et al.*, "CuSCN as hole transport material with 3D/2D perovskite solar cells," *ACS Applied Energy Materials,* vol. 3, no. 1, pp. 114-121, 2019.

[98] F. Matebese, R. Taziwa, and D. Mutukwa, "Progress on the synthesis and application of CuSCN inorganic hole transport material in perovskite solar cells," *Materials,* vol. 11, no. 12, p. 2592, 2018.

[99] H. Wang *et al.*, "Efficient and stable inverted planar perovskite solar cells employing CuI as hole-transporting layer prepared by solid–gas transformation," *Energy Technology,* vol. 5, no. 10, pp. 1836-1843, 2017.

[100] F. Igbari, M. Li, Y. Hu, Z.-K. Wang, and L.-S. Liao, "A room-temperature $CuAlO_2$ hole interfacial layer for efficient and stable planar perovskite solar cells," *Journal of Materials Chemistry A,* vol. 4, no. 4, pp. 1326-1335, 2016.

[101] I. S. Jin, J. H. Lee, Y. W. Noh, S. H. Park, and J. W. Jung, "Molecular doping of CuSCN for hole transporting layers in inverted-type planar perovskite solar cells," *Inorganic Chemistry Frontiers,* vol. 6, no. 8, pp. 2158-2166, 2019.

[102] N. Arora *et al.*, "Perovskite solar cells with CuSCN hole extraction layers yield stabilized efficiencies greater than 20%," *Science,* vol. 358, no. 6364, pp. 768-771, 2017.

[103] P. Pattanasattayavong, V. Promarak, and T. D. Anthopoulos, "Electronic properties of copper (I) thiocyanate (CuSCN)," *Advanced Electronic Materials,* vol. 3, no. 3, p. 1600378, 2017.

[104] L. Pan *et al.*, "$Cu_2O$ photocathodes with band-tail states assisted hole transport for standalone solar water splitting," *Nature communications,* vol. 11, no. 1, p. 318, 2020.

[105] P. Pattanasattayavong *et al.*, "Hole-transporting transistors and circuits based on the transparent inorganic semiconductor copper (I) thiocyanate (CuSCN) processed from solution at room temperature," *Advanced Materials,* vol. 25, no. 10, pp. 1504-1509, 2013.

[106] S. D. Chavhan, T. H. Ou, M.-R. Jiang, C.-W. Wang, and J.-H. Jou, "Enabling high-efficiency organic light-emitting diode with trifunctional solution-processable copper (I) thiocyanate," *The Journal of Physical Chemistry C,* vol. 122, no. 33, pp. 18836-18840, 2018.

[107] J. A. Christians, R. C. Fung, and P. V. Kamat, "An inorganic hole conductor for organo-lead halide perovskite solar cells. Improved hole conductivity with copper iodide," *Journal of the American Chemical Society,* vol. 136, no. 2, pp. 758-764, 2014.

[108] F.-L. Schein, H. von Wenckstern, and M. Grundmann, "Transparent p-CuI/n-ZnO heterojunction diodes," *Applied Physics Letters,* vol. 102, no. 9, p. 092109, 2013.

[109] M. Huangfu *et al.*, "Copper iodide as inorganic hole conductor for perovskite solar cells with different thickness of mesoporous layer and hole transport layer," *Applied Surface Science,* vol. 357, pp. 2234-2240, 2015.

[110] F. Meng *et al.*, "Efficient perovskite solar cells with a CuI-modified polymer hole-transport layer," *ACS Applied Energy Materials,* vol. 5, no. 9, pp. 11034-11041, 2022.

[111] A. Liu *et al.*, "High-performance p-channel transistors with transparent Zn doped-CuI," *Nature communications,* vol. 11, no. 1, p. 4309, 2020.

[112] H. Wang *et al.*, "One plus one greater than two: high-performance inverted planar perovskite solar cells based on a composite CuI/CuSCN hole-transporting layer," *Journal of Materials Chemistry A,* vol. 6, no. 43, pp. 21435-21444, 2018.

[113] W. Sun *et al.*, "Room-temperature and solution-processed copper iodide as the hole transport layer for inverted planar perovskite solar cells," *Nanoscale,* vol. 8, no. 35, pp. 15954-15960, 2016.

[114] R. Bhargav *et al.*, "Copper bromide as an efficient solution-processable hole transport layer for organic solar cells: effect of solvents," *ACS omega,* vol. 4, no. 3, pp. 6028-6034, 2019.

[115] T.-M. Kim, H.-S. Shim, M.-S. Choi, H. J. Kim, and J.-J. Kim, "Multilayer epitaxial growth of lead phthalocyanine and C70 using CuBr as a templating layer for enhancing the efficiency of organic photovoltaic cells," *ACS applied materials & interfaces,* vol. 6, no. 6, pp. 4286-4291, 2014.

[116] S. Zhang *et al.*, "Printable and Homogeneous NiOx Hole Transport Layers Prepared by a Polymer-Network Gel Method for Large-Area and Flexible Perovskite Solar Cells," *Advanced Functional Materials,* vol. 31, no. 47, p. 2106495, 2021.

[117] X. Zhao *et al.*, "Photoconductive NiOx hole transport layer for efficient perovskite solar cells," *Chemical Engineering Journal,* vol. 435, p. 135140, 2022.

[118] S. D. Chavhan *et al.*, "Low temperature processed $NiO_x$ hole transport layers for efficient polymer solar cells," *Organic Electronics,* vol. 44, pp. 59-66, 2017.

[119] W.-S. Chen, S.-H. Yang, W.-C. Tseng, W. W.-S. Chen, and Y.-C. Lu, "Utilization of nanoporous nickel oxide as the hole injection layer for quantum dot light-emitting diodes," *ACS omega,* vol. 6, no. 20, pp. 13447-13455, 2021.

[120] J. Zheng *et al.*, "Solution-processed, silver-doped $NiO_x$ as hole transporting layer for high-efficiency inverted perovskite solar cells," *ACS Applied Energy Materials,* vol. 1, no. 2, pp. 561-570, 2018.

[121] H. Choi *et al.*, "Solution processed $WO_3$ layer for the replacement of PEDOT: PSS layer in organic photovoltaic cells," *Organic Electronics,* vol. 13, no. 6, pp. 959-968, 2012.

[122] G. W. Kim, G. Kang, K. Choi, H. Choi, and T. Park, "Solution processable inorganic–organic double-layered hole transport layer for highly stable planar perovskite solar cells," *Advanced Energy Materials,* vol. 8, no. 26, p. 1801386, 2018.

[123] D. S. Hecht, L. Hu, and G. Irvin, "Emerging transparent electrodes based on thin films of carbon nanotubes, graphene, and metallic nanostructures," *Advanced materials,* vol. 23, no. 13, pp. 1482-1513, 2011.

[124] H.-C. Chu *et al.*, "Spray-deposited large-area copper nanowire transparent conductive electrodes and their uses for touch screen applications," *ACS applied materials & interfaces,* vol. 8, no. 20, pp. 13009-13017, 2016.

[125] K. Sun, P. Li, Y. Xia, J. Chang, and J. Ouyang, "Transparent conductive oxide-free perovskite solar cells with PEDOT: PSS as transparent electrode," *ACS applied materials & interfaces,* vol. 7, no. 28, pp. 15314-15320, 2015.

[126] M. Esro *et al.*, "Solution processed $SnO_2$: Sb transparent conductive oxide as an alternative to indium tin oxide for applications in organic light emitting diodes," *Journal of Materials Chemistry C,* vol. 4, no. 16, pp. 3563-3570, 2016.

[127] N. Gaillard *et al.*, "Wide-bandgap Cu (In, Ga)$S_2$ photocathodes integrated on transparent conductive F:$SnO_2$ substrates for chalcopyrite-based water splitting tandem devices," *ACS Applied Energy Materials,* vol. 2, no. 8, pp. 5515-5524, 2019.

[128] J. Shi, J. Zhang, L. Yang, M. Qu, D. C. Qi, and K. H. Zhang, "Wide bandgap oxide semiconductors: from materials physics to optoelectronic devices," *Advanced Materials,* vol. 33, no. 50, p. 2006230, 2021.

[129] R. Woods-Robinson *et al.*, "Wide band gap chalcogenide semiconductors," *Chemical reviews,* vol. 120, no. 9, pp. 4007-4055, 2020.

[130] A. Elschner, S. Kirchmeyer, W. Lovenich, U. Merker, and K. Reuter, *PEDOT: principles and applications of an intrinsically conductive polymer*. CRC press, 2010.

[131] I.-A. Pavel, S. Lakard, and B. Lakard, "Flexible sensors based on conductive polymers," *Chemosensors,* vol. 10, no. 3, p. 97, 2022.

[132] C. F. Guo and Z. Ren, "Flexible transparent conductors based on metal nanowire networks," *Materials Today,* vol. 18, no. 3, pp. 143-154, 2015.

[133] M. R. Azani, A. Hassanpour, and T. Torres, "Benefits, problems, and solutions of silver nanowire transparent conductive electrodes in indium tin oxide (ITO)-free flexible solar cells," *Advanced Energy Materials,* vol. 10, no. 48, p. 2002536, 2020.

[134] J. K. Wassei and R. B. Kaner, "Graphene, a promising transparent conductor," *Materials today,* vol. 13, no. 3, pp. 52-59, 2010.

[135] L. Yu, C. Shearer, and J. Shapter, "Recent development of carbon nanotube transparent conductive films," *Chemical reviews,* vol. 116, no. 22, pp. 13413-13453, 2016.

[136] Y. G. Bi *et al.*, "Ultrathin metal films as the transparent electrode in ITO-free organic optoelectronic devices," *Advanced Optical Materials,* vol. 7, no. 6, p. 1800778, 2019.

[137] T. Minami, "Transparent conducting oxide semiconductors for transparent electrodes," *Semiconductor science and technology,* vol. 20, no. 4, p. S35, 2005.

[138] A. Rakhshani, Y. Makdisi, and H. Ramazaniyan, "Electronic and optical properties of fluorine-doped tin oxide films," *Journal of applied physics,* vol. 83, no. 2, pp. 1049-1057, 1998.

[139] X. Jiang, F. Wong, M. Fung, and S. Lee, "Aluminum-doped zinc oxide films as transparent conductive electrode for organic light-emitting devices," *Applied Physics Letters,* vol. 83, no. 9, pp. 1875-1877, 2003.

[140] A. Suresh, P. Wellenius, A. Dhawan, and J. Muth, "Room temperature pulsed laser deposited indium gallium zinc oxide channel based transparent thin film transistors," *Applied physics letters,* vol. 90, no. 12, p. 123512, 2007.

[141] K. Nomura, H. Ohta, A. Takagi, T. Kamiya, M. Hirano, and H. Hosono, "Room-temperature fabrication of transparent flexible thin-film transistors using amorphous oxide semiconductors," *nature,* vol. 432, no. 7016, pp. 488-492, 2004.

[142] Z. Wang, P. K. Nayak, J. A. Caraveo-Frescas, and H. N. Alshareef, "Recent developments in p-Type oxide semiconductor materials and devices," *Advanced Materials,* vol. 28, no. 20, pp. 3831-3892, 2016.

[143] V. O. Williams *et al.*, "Fabrication of transparent-conducting-oxide-coated inverse opals as mesostructured architectures for electrocatalysis applications: A case study with NiO," *ACS Applied Materials & Interfaces,* vol. 6, no. 15, pp. 12290-12294, 2014.

[144] M. Moharam, E. Elsayed, J. Nino, R. Abou-Shahba, and M. Rashad, "Potentiostatic deposition of $Cu_2O$ films as p-type transparent conductors at room temperature," *Thin Solid Films,* vol. 616, pp. 760-766, 2016.

[145] H. Kawazoe, M. Yasukawa, H. Hyodo, M. Kurita, H. Yanagi, and H. Hosono, "P-type electrical conduction in transparent thin films of $CuAlO_2$," *Nature,* vol. 389, no. 6654, pp. 939-942, 1997.

[146] S. Nandy, A. Banerjee, E. Fortunato, and R. Martins, "A review on $Cu_2O$ and CuI-based p-type semiconducting transparent oxide materials: promising candidates for new generation oxide based electronics," *Reviews in Advanced Sciences and Engineering,* vol. 2, no. 4, pp. 273-304, 2013.

[147] R. K. Vijayaraghavan *et al.*, "Influence of Oxygen Plasma on the Growth, Structure, Morphology, and Electro-Optical Properties of p-Type Transparent Conducting CuBr Thin Films," *The Journal of Physical Chemistry C,* vol. 118, no. 40, pp. 23226-23232, 2014.

[148] S. Chen, T. Kuo, Y. Lin, and C. Chang, "Preparation and properties of p-type transparent conductive NiO films," in *Advanced Materials Research*, 2010, vol. 123: Trans Tech Publ, pp. 181-184.

[149] A. Kotta and H. K. Seo, "Facile synthesis of highly conductive vanadium-doped NiO film for transparent conductive oxide," *Applied Sciences,* vol. 10, no. 16, p. 5415, 2020.

[150] U. Joshi, Y. Matsumoto, K. Itaka, M. Sumiya, and H. Koinuma, "Combinatorial synthesis of Li-doped NiO thin films and their transparent conducting properties," *Applied surface science,* vol. 252, no. 7, pp. 2524-2528, 2006.

[151] S. Chen, T. Kuo, Y. Lin, and H. Lin, "Preparation and properties of p-type transparent conductive Cu-doped NiO films," *Thin Solid Films,* vol. 519, no. 15, pp. 4944-4947, 2011.

[152] N. Yamada, R. Ino, and Y. Ninomiya, "Truly transparent p-type γ-CuI thin films with high hole mobility," *Chemistry of Materials,* vol. 28, no. 14, pp. 4971-4981, 2016.

[153] P. Storm *et al.*, "High mobility, highly transparent, smooth, p-type CuI thin films grown by pulsed laser deposition," *APL Materials,* vol. 8, no. 9, p. 091115, 2020.

[154] C. Yang, M. Kneiβ, M. Lorenz, and M. Grundmann, "Room-temperature synthesized copper iodide thin film as degenerate p-type transparent conductor with a boosted figure of merit," *Proceedings of the National Academy of Sciences,* vol. 113, no. 46, pp. 12929-12933, 2016.

[155] K. Ahn *et al.*, "Highly Conductive p-Type Transparent Conducting Electrode with Sulfur-Doped Copper Iodide," *Chemistry of Materials,* vol. 34, no. 23, pp. 10517-10527, 2022.

[156] S. Inudo, M. Miyake, and T. Hirato, "Electrical properties of CuI films prepared by spin coating," *physica status solidi (a),* vol. 210, no. 11, pp. 2395-2398, 2013.

[157] I. Kosta, E. Azaceta, L. Yate, G. Cabañero, H. Grande, and R. Tena-Zaera, "Cathodic electrochemical deposition of CuI from room temperature ionic liquid-based electrolytes," *Electrochemistry Communications,* vol. 59, pp. 20-23, 2015.

[158] P. Ahirrao, S. Gosavi, S. S. Sonawane, and R. Patil, "Wide Band gap nanocrystalline CuSCN thin films deposited by modified chemical method," *Arch. Phys. Res,* vol. 2, no. 3, pp. 29-33, 2011.

[159] A. Banik, J. Z. Tubbesing, B. Luo, X. Zhang, and J. A. Switzer, "Epitaxial Electrodeposition of Optically Transparent Hole-Conducting CuI on n-Si (111)," *Chemistry of Materials,* vol. 33, no. 9, pp. 3220-3227, 2021.

[160] V. S. Vavilov, "Physics and applications of wide bandgap semiconductors," *Physics-Uspekhi,* vol. 37, no. 3, p. 269, 1994.

[161] Y. Zou, Y. Zhang, Y. Hu, and H. Gu, "Ultraviolet detectors based on wide bandgap semiconductor nanowire: A review," *Sensors,* vol. 18, no. 7, p. 2072, 2018.

[162] M. Meneghini, L.-R. Trevisanello, G. Meneghesso, and E. Zanoni, "A review on the reliability of GaN-based LEDs," *IEEE Transactions on Device and Materials Reliability,* vol. 8, no. 2, pp. 323-331, 2008.

[163] B.-C. Lin *et al.*, "Advantages of blue LEDs with graded-composition AlGaN/GaN superlattice EBL," *IEEE Photonics Technology Letters,* vol. 25, no. 21, pp. 2062-2065, 2013.

[164] S. Jha *et al.*, "Violet-blue LEDs based on p-GaN/n-ZnO nanorods and their stability," *Nanotechnology,* vol. 22, no. 24, p. 245202, 2011.

[165] A. R. Powell and L. B. Rowland, "SiC materials-progress, status, and potential roadblocks," *Proceedings of the IEEE,* vol. 90, no. 6, pp. 942-955, 2002.

[166] A. Cowley, "Novel ultra-violet/blue optoelectronic materials and devices based on copper halides (CuHa)," Dublin City University, 2012.

[167] A. Cowley *et al.*, "Electroluminescence of γ-CuBr thin films via vacuum evaporation depositon," *Journal of Physics D: Applied Physics,* vol. 43, no. 16, p. 165101, 2010.

[168] O. Madelung, *Semiconductors: data handbook*. Springer Science & Business Media, 2004.

[169] S. Nakamura and G. Fasol, *The blue laser diode: GaN based light emitters and lasers*. Springer Science & Business Media, 2013.

[170] P. Von Dollen, S. Pimputkar, and J. S. Speck, "Let there be light—with gallium nitride: The 2014 Nobel Prize in Physics," *Angewandte Chemie International Edition,* vol. 53, no. 51, pp. 13978-13980, 2014.

[171] S.-D. Baek, D.-K. Kwon, Y. C. Kim, and J.-M. Myoung, "Violet light-emitting diodes based on p-CuI thin film/n-MgZnO quantum dot heterojunction," *ACS applied materials & interfaces,* vol. 12, no. 5, pp. 6037-6047, 2020.

[172] Y. I. Alivov, J. Van Nostrand, D. C. Look, M. Chukichev, and B. Ataev, "Observation of 430 nm electroluminescence from ZnO/GaN heterojunction light-emitting diodes," *Applied Physics Letters,* vol. 83, no. 14, pp. 2943-2945, 2003.

[173] Q. Zhang, H. Guo, Z. Feng, L. Lin, J. Zhou, and Z. Lin, "n-ZnO nanorods/p-CuSCN heterojunction light-emitting diodes fabricated by electrochemical method," *Electrochimica Acta,* vol. 55, no. 17, pp. 4889-4894, 2010.

[174] Y. Li *et al.*, "Study of polarization field in GaN-based blue LEDs on Si and sapphire substrate by electroluminescence," *Journal of luminescence,* vol. 122, pp. 567-570, 2007.

[175] D. Ahn and S.-H. Park, "Cuprous halides semiconductors as a new means for highly efficient light-emitting diodes," *Scientific Reports,* vol. 6, no. 1, pp. 1-9, 2016.

[176] A. Cowley *et al.*, "UV emission on a Si substrate: Optical and structural properties of γ-CuCl on Si grown using liquid phase epitaxy techniques," *physica status solidi (a),* vol. 206, no. 5, pp. 923-926, 2009.

[177] B. Bao *et al.*, "Sodium deca-tungstate/polyacrylic acid self-assembled flexible wearable photochromic composite fabric for solar UV detector," *Composites Part B: Engineering,* vol. 202, p. 108464, 2020.

[178] C. Avila-Avendano, M. I. Pintor-Monroy, A. Ortiz-Conde, J. A. Caraveo-Frescas, and M. A. Quevedo-Lopez, "Deep UV sensors enabling solar-blind flame detectors for large-area applications," *IEEE Sensors Journal,* vol. 21, no. 13, pp. 14815-14821, 2021.

[179] H. Guan *et al.*, "A self-powered UV photodetector based on the hydrovoltaic and photoelectric coupling properties of ZnO nanowire arrays," *Journal of Alloys and Compounds,* vol. 867, p. 159073, 2021.

[180] D. Wang *et al.*, "Self-powered ZnO/$SrCoO_x$ flexible ultraviolet detectors processed at room temperature," *Materials & Design,* vol. 203, p. 109616, 2021.

[181] L. Sun, C. Wang, T. Ji, J. Wang, G.-C. Yi, and X. Chen, "Self-powered UV-visible photodetector with fast response and high photosensitivity employing an Fe: $TiO_2$/n-Si heterojunction," *RSC advances,* vol. 7, no. 81, pp. 51744-51749, 2017.

[182] Y. Gao *et al.*, "$TiO_2$ nanorod arrays based self-powered UV photodetector: heterojunction with NiO nanoflakes and enhanced UV photoresponse," *ACS applied materials & interfaces,* vol. 10, no. 13, pp. 11269-11279, 2018.

[183] B. Sun *et al.*, "High-sensitive, self-powered deep UV photodetector based on p-CuSCN/n-$Ga_2O_3$ thin film heterojunction," *Optics Communications,* vol. 504, p. 127483, 2022.

[184] Z. Zhou *et al.*, "Self-powered p-CuI/n-GaN heterojunction UV photodetector based on thermal evaporated high quality CuI thin film," *Optics Express,* vol. 30, no. 16, pp. 29749-29759, 2022.

[185] S. M. Hatch, J. Briscoe, and S. Dunn, "A self-powered ZnO-nanorod/CuSCN UV photodetector exhibiting rapid response," *Advanced Materials,* vol. 25, no. 6, pp. 867-871, 2013.

[186] F. Cao, L. Jin, Y. Wu, and X. Ji, "High-performance, self-powered UV photodetector based on Au nanoparticles decorated ZnO/CuI heterostructure," *Journal of Alloys and Compounds,* vol. 859, p. 158383, 2021.

[187] H.-P. Lin, X.-J. Lin, and D.-C. Perng, "Electrodeposited CuSCN metal-semiconductor-metal high performance deep-ultraviolet photodetector," *Applied Physics Letters,* vol. 112, no. 2, p. 021107, 2018.

[188] C. Gong *et al.*, "Self-confined growth of ultrathin 2D nonlayered wide-bandgap semiconductor CuBr flakes," *Advanced Materials,* vol. 31, no. 36, p. 1903580, 2019.

[189] N. Yamada, Y. Kondo, X. Cao, and Y. Nakano, "Visible-blind wide-dynamic-range fast-response self-powered ultraviolet photodetector based on CuI/In-Ga-Zn-O heterojunction," *Applied Materials Today,* vol. 15, pp. 153-162, 2019.

[190] G. Stringfellow, "Epitaxy," *Reports on Progress in Physics,* vol. 45, no. 5, p. 469, 1982.

[191] Z. H. Bakr, Q. Wali, A. Fakharuddin, L. Schmidt-Mende, T. M. Brown, and R. Jose, "Advances in hole transport materials engineering for stable and efficient perovskite solar cells," *Nano energy,* vol. 34, pp. 271-305, 2017.

[192] G. W. Kim, H. Choi, M. Kim, J. Lee, S. Y. Son, and T. Park, "Hole transport materials in conventional structural (n–i–p) perovskite solar cells: from past to the future," *Advanced Energy Materials,* vol. 10, no. 8, p. 1903403, 2020.

[193] J. Ren, Y. Tao, X. Li, T. Ma, B. Liu, and D. Lu, "Effect of external electric field on the ordered structure of molecular chains and hole mobility in regioregular poly (3-hexylthiophene) with different molecular weights," *Langmuir,* vol. 34, no. 46, pp. 13871-13881, 2018.

[194] I. Yavuz and K. Houk, "Mesoscale ordering and charge-transport of crystalline spiro-OMeTAD organic semiconductors," *The Journal of Physical Chemistry C,* vol. 121, no. 2, pp. 993-999, 2017.

[195] X. Tang *et al.*, "Stripping GaN/InGaN epitaxial films and fabricating vertical GaN-based light-emitting diodes," *Vacuum,* vol. 187, p. 110160, 2021.

[196] T. Dutta, P. Gupta, A. Gupta, and J. Narayan, "Effect of Li doping in NiO thin films on its transparent and conducting properties and its application in heteroepitaxial pn junctions," *Journal of Applied Physics,* vol. 108, no. 8, p. 083715, 2010.

[197] B. Feng *et al.*, "$CuInO_2$ epitaxial thin films on epi-GaN wafer: Fabrication and solar-blind photodetector," *Applied Surface Science,* vol. 604, p. 154505, 2022.

[198] T. Ikenoue, J. Inoue, M. Miyake, and T. Hirato, "Epitaxial growth of undoped and Li-doped NiO thin films on α-$Al_2O_3$ substrates by mist chemical vapor deposition," *Journal of Crystal Growth,* vol. 507, pp. 379-383, 2019.

[199] Y. Zhao *et al.*, "Enhanced P-type GaN conductivity by Mg delta doped AlGaN/GaN superlattice structure," *Materials,* vol. 14, no. 1, p. 144, 2020.

[200] K. Mustonen *et al.*, "Toward exotic layered materials: 2D cuprous iodide," *Advanced Materials,* vol. 34, no. 9, p. 2106922, 2022.

[201] M. Grundmann, F. L. Schein, M. Lorenz, T. Böntgen, J. Lenzner, and H. von Wenckstern, "Cuprous iodide–ap-type transparent semiconductor: History and novel applications," *physica status solidi (a),* vol. 210, no. 9, pp. 1671-1703, 2013.

[202] L. Mohan *et al.*, "Low Temperature Scalable Deposition of Copper (I) Thiocyanate Films via Aerosol-Assisted Chemical Vapor Deposition," *Crystal Growth & Design,* vol. 20, no. 8, pp. 5380-5386, 2020.

[203] K. Zhao, R. Munir, B. Yan, Y. Yang, T. Kim, and A. Amassian, "Solution-processed inorganic copper (I) thiocyanate (CuSCN) hole transporting layers for efficient p–i–n perovskite solar cells," *Journal of Materials Chemistry A,* vol. 3, no. 41, pp. 20554-20559, 2015.

[204] B. Sankapal, E. Goncalves, A. Ennaoui, and M. C. Lux-Steiner, "Wide band gap p-type windows by CBD and SILAR methods," *Thin Solid Films,* vol. 451, pp. 128-132, 2004.

[205] C. Chappaz-Gillot, R. Salazar, S. Berson, and V. Ivanova, "Room temperature template-free electrodeposition of CuSCN nanowires," *Electrochemistry communications,* vol. 24, pp. 1-4, 2012.

[206] S. Li *et al.*, "UV photoresponse properties of ZnO nanorods arrays deposited with CuSCN by SILAR method," *Chemical Physics Letters,* vol. 620, pp. 50-55, 2015.

[207] L. Sun, K. Ichinose, T. Sekiya, T. Sugiura, and T. Yoshida, "Cathodic electrodeposition of p-CuSCN nanorod and its dye-sensitized photocathodic property," *Physics Procedia,* vol. 14, pp. 12-24, 2011.

[208] T. Iwamoto *et al.*, "Electrochemical self-assembly of nanostructured CuSCN/rhodamine B hybrid thin film and its dye-sensitized photocathodic properties," *The Journal of Physical Chemistry C,* vol. 118, no. 30, pp. 16581-16590, 2014.

[209] W. Luo *et al.*, "Copper thiocyanate/copper iodide based hole transport composites with balanced properties for efficient polymer light-emitting diodes," *Journal of Materials Chemistry C,* vol. 6, no. 18, pp. 4895-4902, 2018.

[210] S. Inagaki *et al.*, "Molecular beam epitaxy of high-quality CuI thin films on a low temperature grown buffer layer," *Applied Physics Letters,* vol. 116, no. 19, p. 192105, 2020.

[211] M. Nakayama, A. Soumura, K. Hamasaki, H. Takeuchi, and H. Nishimura, "Hot excitons in CuCl and CuBr crystalline thin films grown by vacuum deposition," *Physical Review B,* vol. 55, no. 15, p. 10099, 1997.

[212] P. Storm, S. Selle, H. von Wenckstern, M. Grundmann, and M. Lorenz, "Epitaxial lift-off of single crystalline CuI thin films," *Journal of Materials Chemistry C,* vol. 10, no. 11, pp. 4124-4127, 2022.

[213] R. Bulakhe, N. Shinde, R. Thorat, S. Nikam, and C. Lokhande, "Deposition of copper iodide thin films by chemical bath deposition (CBD) and successive ionic layer adsorption and reaction (SILAR) methods," *Current Applied Physics,* vol. 13, no. 8, pp. 1661-1667, 2013.

[214] C. M. Chang, L. M. Davis, E. K. Spear, and R. G. Gordon, "Chemical vapor deposition of transparent, p-type cuprous bromide thin films," *Chemistry of Materials,* vol. 33, no. 4, pp. 1426-1434, 2021.

[215] S. Emin *et al.*, "A novel approach for the preparation of textured CuO thin films from electrodeposited CuCl and CuBr," *Journal of Electroanalytical Chemistry,* vol. 717, pp. 243-249, 2014.

[216] H. Kang, R. Liu, K. Chen, Y. Zheng, and Z. Xu, "Electrodeposition and optical properties of highly oriented γ-CuI thin films," *Electrochimica acta,* vol. 55, no. 27, pp. 8121-8125, 2010.

[217] D. Ramírez, K. Álvarez, G. Riveros, B. González, and E. A. Dalchiele, "Electrodeposition of CuSCN seed layers and nanowires: A microelectrogravimetric approach," *Electrochimica Acta,* vol. 228, pp. 308-318, 2017.

[218] R. Krumpolec *et al.*, "Structural and optical properties of luminescent copper (I) chloride thin films deposited by sequentially pulsed chemical vapour deposition," *Coatings,* vol. 8, no. 10, p. 369, 2018.

[219] L. O'Reilly *et al.*, "Growth and characterisation of wide-bandgap, I-VII optoelectronic materials on silicon," *Journal of Materials Science: Materials in Electronics,* vol. 16, pp. 415-419, 2005.

[220] D. Shi *et al.*, "Spiro-OMeTAD single crystals: Remarkably enhanced charge-carrier transport via mesoscale ordering," *Science advances,* vol. 2, no. 4, p. e1501491, 2016.

[221] J. C. Love, L. A. Estroff, J. K. Kriebel, R. G. Nuzzo, and G. M. Whitesides, "Self-assembled monolayers of thiolates on metals as a form of nanotechnology," *Chemical reviews,* vol. 105, no. 4, pp. 1103-1170, 2005.

[222] R. Haneda and K. Aramaki, "Protection of Copper Corrosion by an Ultrathin Two-Dimensional Polymer Film of Alkanethiol Monolayer," *Journal of the Electrochemical Society,* vol. 145, no. 6, p. 1856, 1998.

[223] A.-C. Liu, D.-c. Chen, C.-C. Lin, H.-H. Chou, and C.-h. Chen, "Application of cysteine monolayers for electrochemical determination of sub-ppb copper (II)," *Analytical Chemistry,* vol. 71, no. 8, pp. 1549-1552, 1999.

[224] J. Aizenberg, A. J. Black, and G. M. Whitesides, "Control of crystal nucleation by patterned self-assembled monolayers," *Nature,* vol. 398, no. 6727, pp. 495-498, 1999.

[225] T. Weimann, W. Geyer, P. Hinze, V. Stadler, W. Eck, and A. Gölzhäuser, "Nanoscale patterning of self-assembled monolayers by e-beam lithography," *Microelectronic engineering,* vol. 57, pp. 903-907, 2001.

[226] J. L. Wilbur, A. Kumar, E. Kim, and G. M. Whitesides, "Microfabrication by microcontact printing of self-assembled monolayers," *Advanced materials,* vol. 6, no. 7-8, pp. 600-604, 1994.

[227] R. J. Barsotti, M. S. O'Connel, and F. Stellacci, "Morphology control in self-assembled monolayers written by dip pen nanolithography," *Langmuir,* vol. 20, no. 12, pp. 4795-4798, 2004.

[228] C. Vericat, M. Vela, and R. Salvarezza, "Self-assembled monolayers of alkanethiols on Au (111): surface structures, defects and dynamics," *Physical Chemistry Chemical Physics,* vol. 7, no. 18, pp. 3258-3268, 2005.

[229] E. Biemmi, C. Scherb, and T. Bein, "Oriented growth of the metal organic framework tunable with functionalized self-assembled monolayers," *Journal of the American Chemical Society,* vol. 129, no. 26, pp. 8054-8055, 2007.

[230] J. Aizenberg, A. J. Black, and G. M. Whitesides, "Oriented growth of calcite controlled by self-assembled monolayers of functionalized alkanethiols supported on gold and silver," *Journal of the American Chemical Society,* vol. 121, no. 18, pp. 4500-4509, 1999.

[231] A. L. Briseno *et al.*, "Patterned growth of large oriented organic semiconductor single crystals on self-assembled monolayer templates," *Journal of the American Chemical Society,* vol. 127, no. 35, pp. 12164-12165, 2005.

[232] A. M. Travaille *et al.*, "Highly oriented self-assembled monolayers as templates for epitaxial calcite growth," *Journal of the American Chemical Society,* vol. 125, no. 38, pp. 11571-11577, 2003.

[233] A. M. Travaille, E. G. Steijven, H. Meekes, and H. van Kempen, "Thermodynamics of epitaxial calcite nucleation on self-assembled monolayers," *The Journal of Physical Chemistry B,* vol. 109, no. 12, pp. 5618-5626, 2005.

[234] Z. She, A. DiFalco, G. Hähner, and M. Buck, "Electron-beam patterned self-assembled monolayers as templates for Cu electrodeposition and lift-off," *Beilstein Journal of Nanotechnology,* vol. 3, no. 1, pp. 101-113, 2012.

[235] M. Nishizawa, T. Sunagawa, and H. Yoneyama, "Underpotential deposition of copper on gold electrodes through self-assembled monolayers of propanethiol," *Langmuir,* vol. 13, no. 20, pp. 5215-5217, 1997.

[236] J.-F. Liu *et al.*, "Fabrication of colloidal gold micro-patterns using photolithographed self-assembled monolayers as templates," *Thin Solid Films,* vol. 327, pp. 176-179, 1998.

[237] O. Azzaroni, P. Schilardi, and R. Salvarezza, "Metal electrodeposition on self-assembled monolayers: a versatile tool for pattern transfer on metal thin films," *Electrochimica acta,* vol. 48, no. 20-22, pp. 3107-3114, 2003.

[238] P. Schilardi, O. Azzaroni, and R. Salvarezza, "A novel application of alkanethiol self-assembled monolayers in nanofabrication: Direct molding and replication of patterned conducting masters," *Langmuir,* vol. 17, no. 9, pp. 2748-2752, 2001.

[239] T. Baunach *et al.*, "A New Approach to the Electrochemical Metallization of Organic Monolayers: Palladium Deposition onto a 4, 4′-Dithiodipyridine Self-Assembled Monolayer," *Advanced Materials,* vol. 16, no. 22, pp. 2024-2028, 2004.

[240] S. A. Hashemi, S. Ramakrishna, and A. G. Aberle, "Recent progress in flexible–wearable solar cells for self-powered electronic devices," *Energy & Environmental Science,* vol. 13, no. 3, pp. 685-743, 2020.

[241] D. Zhang, T. Huang, and L. Duan, "Emerging self-emissive technologies for flexible displays," *Advanced Materials,* vol. 32, no. 15, p. 1902391, 2020.

[242] N. Wen *et al.*, "Emerging flexible sensors based on nanomaterials: recent status and applications," *Journal of Materials Chemistry A,* vol. 8, no. 48, pp. 25499-25527, 2020.

[243] Z. Wu *et al.*, "Carbon-nanomaterial-based flexible batteries for wearable electronics," *Advanced Materials,* vol. 31, no. 9, p. 1800716, 2019.

[244] X. Meng *et al.*, "Bio-inspired vertebral design for scalable and flexible perovskite solar cells," *Nature Communications,* vol. 11, no. 1, p. 3016, 2020.

[245] C.-W. Cheng, K.-T. Shiu, N. Li, S.-J. Han, L. Shi, and D. K. Sadana, "Epitaxial lift-off process for gallium arsenide substrate reuse and flexible electronics," *Nature communications,* vol. 4, no. 1, p. 1577, 2013.

[246] C. M. Campbell, C.-Y. Tsai, J. Ding, and Y.-H. Zhang, "Epitaxial lift off of II-VI thin films using water-soluble MgTe," *IEEE Journal of Photovoltaics,* vol. 9, no. 6, pp. 1834-1838, 2019.

[247] F. Chancerel *et al.*, "Epitaxial lift-off of InGaAs solar cells from InP substrate using a strained AlAs/InAlAs superlattice as a novel sacrificial layer," *Solar Energy Materials and Solar Cells,* vol. 195, pp. 204-212, 2019.

[248] H. S. Kum *et al.*, "Heterogeneous integration of single-crystalline complex-oxide membranes," *Nature,* vol. 578, no. 7793, pp. 75-81, 2020.

[249] Y. Kim *et al.*, "Remote epitaxy through graphene enables two-dimensional material-based layer transfer," *Nature,* vol. 544, no. 7650, pp. 340-343, 2017.

# VITA

Bin Luo was born in Shaoxing city, Zhejiang province, China. Bin Luo obtained his bachelor's degree in Polymer Materials and Engineering (Excellent Class) at Donghua University of China in Shanghai in 2015. During his undergraduate period, his research focused on acid-base responsive functional polymeric ionic liquids, and he published his first-author paper in Polymer Chemistry journal. In 2018, he obtained his master's degree in Material Science at Donghua University of China in Shanghai. During his master, his work focused on functional conductive polymers for toxic gas sensing. Since 2018, he worked for 1.5 years as a R & D Engineer in Yinshi Technology Co., Ltd. (Shanghai, China) to lead the development of low-power VOCs gas sensors and electronic noses. In 2019, he was accepted in the Chemistry Department at Missouri University of Science Technology in Rolla, Missouri. In August of 2019, he joined Prof. Jay A. Switzer's lab as a PhD student. His research has focused on epitaxial electrodeposition of wide bandgap p-type semiconductors and copper metal via self-assembled monolayer towards energy conversion and flexible electronics applications. During his PhD, his work on epitaxial CuSCN was published in Chemistry of Materials journal. He received his PhD in Chemistry from Missouri University of Science and Technology in May 2023.